THESIS

THE RELATIVE INFLUENCE OF AEROSOLS AND THE ENVIRONMENT ON ORGANIZED TROPICAL AND MIDLATITUDE DEEP CONVECTION

Submitted by

Leah Danielle Grant

Department of Atmospheric Science

In partial fulfillment of the requirements

For the Degree of Master of Science

Colorado State University

Fort Collins, Colorado

Spring 2014

Master's Committee:

Advisor: Susan C. van den Heever

Richard H. Johnson
Jay M. Ham

ABSTRACT

THE RELATIVE INFLUENCE OF AEROSOLS AND THE ENVIRONMENT ON ORGANIZED TROPICAL AND MIDLATITUDE DEEP CONVECTION

In this two-part study, the relative impacts of aerosols and the environment on organized deep convection, including tropical sea-breeze convection and midlatitude supercellular and multicellular deep convection, are investigated within idealized cloud-resolving modeling simulations using the Regional Atmospheric Modeling System (RAMS). Part one explores aerosol-cloud-land surface interactions within tropical deep convection organized along a sea breeze front. The idealized RAMS domain setup is representative of the coastal Cameroon rainforest in equatorial Africa. In order to assess the potential sensitivity of sea-breeze convection to increasing anthropogenic activity and deforestation occurring in such regions, 27 total simulations are performed in which combinations of enhanced aerosol concentrations, reduced surface roughness length, and reduced soil moisture are included. Both enhanced aerosols and reduced soil moisture are found to individually reduce the precipitation due to reductions in downwelling shortwave radiation and surface latent heat fluxes, respectively, while perturbations to the roughness length do not have a large impact on the precipitation. The largest soil moisture perturbations dominate the precipitation changes due to reduced low-level moisture available to the convection, but if the soil moisture perturbation is moderate, synergistic interactions between soil moisture and aerosols enhance the sea breeze precipitation. This is found to result from evening convection that forms ahead of the sea breeze only when both

effects are present. Interactions between the resulting gust fronts and the sea breeze front locally enhance convergence and therefore the rainfall.

Part two of this study investigates the relative roles of midlevel dryness and aerosols on supercellular and multicellular convective morphology. A common storm-splitting situation is simulated wherein the right-moving storm becomes a dominant supercell and the left-moving storm evolves into a multicellular cluster. The right-mover, which is a classic (CL) supercell in the control simulation, becomes a low-precipitation (LP) supercell with increasing dryness aloft. Different midlevel hail growth mechanisms are found to dominate in the CL and LPs that assist in explaining their varying surface precipitation distributions. Although the CL and LP supercells are dynamically similar, their microphysical structure differs due to the strong control that midlevel dryness exerts on supercell morphology; aerosols have little impact on the supercellular structure. On the other hand, while midlevel dryness also dominates the changes to the multicellular convection, aerosols influence the precipitation through feedbacks to the cold pool strength and subsequent dynamical forcing.

Overall, aerosol impacts are largest for the most weakly organized convection (tropical sea breeze convection) and smallest for strongly dynamic convection (supercells). Additionally, aerosol impacts are modulated by environmental influences, most notably soil moisture availability and midlevel moisture content in this study.

ACKNOWLEDGEMENTS

First and foremost, I would like to thank my adviser, Dr. Susan van den Heever. I am very fortunate to have been given the opportunity to study storm dynamics and microphysics in her group at CSU. Under her mentorship, I have grown a thousand fold as a young scientist. She has led me to become a better writer and a more confident presenter, taught me to better manage my time (despite my best procrastination efforts at times), and cultivated an ever-increasing passion and respect for the science. I could not imagine a more wonderful adviser and hope to one day follow her outstanding example in this regard.

I would also like to extend a special thank-you to my committee members, Drs. Richard Johnson and Jay Ham, for their time, effort, and insights in serving on my committee and for their helpful comments and suggestions for this thesis. I thank Dr. Lixin Lu of the Cooperative Institute for Research in the Atmosphere (CIRA) for her insight into land surface processes in the initial stages of the study presented in Chapter 2. Many thanks as well to the members of the van den Heever research group, both past and present. I have had many enlightening, entertaining, and inspiring conversations that have led to my enhanced understanding of all things clouds, convection, and numerical modeling with Robert Seigel, Adele Igel, Steve Saleeby, Amanda Sheffield, Peter Marinescu, Clay McGee, Josh King, Steve Herbener, Matt Igel, Rachel Storer, Michal Clavner, and Aryeh Drager. Finally, I thank my family, especially my parents, and my friends for their unfailing support and encouragement.

This work has been supported by a graduate fellowship from CIRA and by a fellowship from the American Meteorological Society.

TABLE OF CONTENTS

CHAPTER 1: INTRODUCTION

1.1 Aerosol Impacts on Deep Convection

Aerosol-cloud interactions have received much attention over the past few decades by virtue of their potential to influence important aspects of the earth system, notably the radiation budget and the hydrological cycle. Many of the original studies of aerosol-cloud interactions were of shallow warm-rain cloud systems, and multiple aerosol indirect effects have been identified from these studies. With increasing aerosol number concentrations and a constant liquid water content, smaller cloud droplets form which more effectively scatter solar radiation, thereby brightening the clouds (the first indirect effect; Twomey 1977). Collision-coalescence is also less efficient as cloud droplet sizes decrease, and so warm clouds forming in more polluted environments may precipitate less, which may in turn extend the cloud lifetime (the second indirect effect; Albrecht 1989). Aerosols may also directly interact with radiation. Absorbing aerosols may change the thermodynamic environment and reduce the cloud lifetime (the semidirect effect; Ackerman et al. 2000). Such aerosol impacts on warm rain clouds are well-studied and relatively well understood.

Aerosol-cloud interactions within deep convective clouds are more complicated because the influence of aerosols on the warm phase region of the cloud extends into the mixed phase region, thereby impacting the multiple pathways through which ice-phase hydrometeors may form. One example is the concept of convective invigoration (Andreae et al. 2004; Khain et al. 2005; van den Heever et al. 2006; van den Heever and Cotton 2007; Rosenfeld et al. 2008), which has received increasing attention in the past decade. The traditional explanation of convective invigoration is that under more polluted conditions the efficiency of the warm rain

process is reduced as cloud droplet sizes decrease; more cloud water is therefore available to be lofted above the freezing level, where it may be collected by ice hydrometeors. The additional freezing and latent heating invigorates the cloud updraft, which would subsequently enhance the amount of precipitation produced at the surface. Moreover, recent modeling and observational studies have shown that enhanced aerosol concentrations lead to fewer, larger raindrops within warm-phase (Altaratz et al. 2007; Berg et al. 2008; Saleeby et al. 2010) and convective clouds (Storer et al. 2010; May et al. 2011; Storer and van den Heever 2013). Populations of larger raindrops fall faster and also have less net surface area, which reduces evaporative cooling within the downdraft. This weakens the cold pool and subsequent dynamical forcing. Overall, under more polluted conditions, the convective cloud lifetime and total amount of precipitation could either increase or decrease, depending on the balance between the storm motion and cold pool propagation (van den Heever and Cotton 2007; Storer et al. 2010; Morrison 2012). These examples highlight the complexity of aerosol impacts on deep convective clouds because of the existence of microphysical-dynamical feedbacks.

Recent studies have demonstrated the importance of considering aerosol indirect effects within a larger system-wide context. For instance, aerosol indirect effects have been investigated within simulations of tropical deep convection under the framework of radiative-convective equilibrium (RCE), a good approximation to the tropical atmosphere (van den Heever et al. 2011; Storer and van den Heever 2013). van den Heever et al. (2011) demonstrated that aerosols invigorated the deep convective clouds and the large-scale circulation. The invigorated circulation led to suppression of precipitation within shallow clouds that compensated for the changes in the precipitation within deep convective clouds, leading to only a small response in the domain-wide precipitation. It has also been noted in these RCE simulations that the impact of

aerosols on deep convection depends on the storm lifetime. Storer and van den Heever (2013) showed that in earlier stages of convective development, aerosols invigorate convection through enhanced latent heating from condensation, vapor deposition, and freezing, but later in the convective life cycle, increased condensate loading was an important factor in determining the updraft strength. van den Heever et al. (2006), van den Heever and Cotton (2007), and Tao et al. (2007) also found that aerosol impacts on deep convection vary within the deep convective cloud life cycle.

Including other aspects of the earth system in studies of aerosol-cloud interactions may also modulate the response of clouds and precipitation to aerosol loading by virtue of feedbacks within the system, although few studies have investigated this. Jiang and Feingold (2006) considered a coupled aerosol-cloud-radiation-land surface system in their modeling study of aerosol impacts on warm-phase cumulus clouds. They found that the inclusion of aerosol direct effects were very important. When the direct effects were considered, the cloud-atmosphere-land surface system response to increasing aerosol concentrations was substantially modified by the reduction in the surface fluxes and subsequent changes to the evolution of the boundary layer. The net effect was a reduction in the magnitude of the second aerosol indirect effect within the coupled system compared to simulations when feedbacks between the aerosol radiative effects and the land surface were not included.

To further complicate matters, recent studies have shown that the impact of aerosols on deep convective clouds may vary according to environmental parameters such as instability, vertical wind shear, and relative humidity, and therefore cloud type (Seifert and Beheng 2006; Khain et al. 2008; Fan et al. 2009; Storer et al. 2010). Khain et al. (2008) found that precipitation associated with deep convection increased with increasing aerosol concentrations if the relative

humidity was high, but decreased if the relative humidity was low due to enhanced hydrometeor evaporation. Fan et al. (2009) showed that aerosols invigorate isolated deep convection under scenarios of weak vertical wind shear but suppress it under strong wind shear. Storer et al. (2010) investigated aerosol effects on supercellular and multicellular deep convection for a range of values of Convective Available Potential Energy (CAPE). They found that the amount of CAPE modulates the precipitation response to aerosols, since the variation in total precipitation with changing aerosol concentrations was smaller with higher CAPE. The results of Storer et al. (2010) indicated that the ability of aerosols to influence deep convective precipitation depends on the level of dynamical forcing and, by extension, the level of storm organization, which was also suggested by Seifert and Beheng (2006).

1.2 Experiment Objectives and Key Findings

The wide range of deep convective precipitation responses to aerosol forcing in these recent studies demonstrate the need to better characterize aerosol impacts on different types of deep convection under broader contexts, taking into account the possible modulation by other environmental parameters and feedbacks within the aerosol-cloud-land-atmosphere system. The primary goal of the research presented in this thesis is therefore to explore the relative influence of aerosols and the environment on the precipitation and characteristics of different types of deep convection, including weakly organized tropical convection and more strongly organized midlatitude convection. To accomplish this goal, idealized cloud-resolving modeling simulations that can systematically and carefully control for variations in aerosols and environmental parameters are performed using the Regional Atmospheric Modeling System (RAMS). The use of such an idealized approach is highly appropriate in exploring the stated objectives because

separating aerosol impacts from environmental influences on deep convection within observations remains a challenging problem, as changes in background aerosol concentrations are often accompanied by concomitant changes in thermodynamic regimes (e.g. May et al. 2009; Wall et al. 2014).

The first part of this study investigates the potential sensitivity of tropical sea breeze convection under weak vertical wind shear to variations in aerosols, the surface roughness length, and soil moisture, and their potential synergistic interactions by virtue of feedbacks within the aerosol-cloud-land surface system. Tropical convection is crucial to the global circulation and hydrological cycle. Therefore, understanding its potential sensitivity to aerosols, roughness length, and soil moisture is important because all of these parameters are frequently altered by anthropogenic activity and deforestation practices in rainforest regions. Idealized simulations of tropical sea breeze convection were conducted using RAMS, and mechanisms responsible for the changes in the rainfall patterns were assessed. The methodology and results from this study, titled "Aerosol-Cloud-Land Surface Interactions within Tropical Sea Breeze Convection," are presented in Chapter 2 of this thesis and have been prepared for submission to the *Journal of Geophysical Research*.

The major findings from the sea breeze study are as follows: (1) when soil moisture is substantially reduced or the aerosol concentrations are significantly enhanced, the sea breeze precipitation is limited by the large reductions in surface latent heat fluxes for drier soil and surface heating for polluted conditions. Their influences dominate the response of the sea breeze precipitation. (2) If perturbations to the soil moisture or aerosol concentrations are not too large, synergistic interactions between aerosols and soil moisture, and between aerosols and the surface roughness length, feed back to the sea breeze convergence and thereby enhance the sea breeze

precipitation. Therefore, the pathway by which synergistic feedbacks within the aerosol-cloud-land surface system occur is primarily through the low-level convergence in these simulations.

The second study presented in this thesis switches focus from the tropics to the midlatitudes and investigates the relative impacts of aerosols and midlevel dryness on more organized multicellular convection and highly organized supercellular convection occurring within the same domain under strong ambient vertical wind shear. Another set of idealized simulations was conducted with RAMS, and the resultant sensitivity of the convective morphology was analyzed. The background, methodology, and findings from this study, titled "Relative Impact of Midlevel Dryness and Aerosols on Midlatitude Deep Convective Morphology," are presented in Chapter 3 of this document. The main results from this study are the following: (1) the presence of midlevel dryness exerts a much stronger control on convective morphology than do aerosols. In agreement with previous studies (e.g. Storer et al. 2010) and the results presented in Chapter 2 of this thesis, the environment modulates the influence of aerosols on convection. (2) Aerosols impact the multicellular convection through feedbacks to the strength of the cold pool. The dry layer altitude influences whether enhanced aerosols increase or decrease the multicellular precipitation. (3) With increasing midlevel dryness, supercells transition from the classic supercell structure to the low-precipitation archetype, but aerosols have very little influence on the supercellular storm structure because the supercell dynamics overwhelm the aerosol influences. The results regarding the influence of midlevel dryness on supercell morphology have been accepted for publication in the *Journal of the Atmospheric Sciences* in a paper titled "Microphysical and Dynamical Characteristics of Low-Precipitation and Classic Supercells" (Grant and van den Heever 2014;).

The broad conclusions from these two studies are as follows:

- Aerosol impacts on deep convection are largest for the most weakly organized deep convection (tropical sea breeze convection) and smallest for the most strongly organized convection (midlatitude supercells).
- The environment, particularly soil moisture and midlevel humidity, modulates the influence of aerosols on deep convection.

The next chapter of this document, Chapter 2, describes the study investigating the influence of aerosols, land surface characteristics, and their feedbacks to tropical sea breeze convection. The relative impacts of aerosols and midlevel dryness on supercellular and multicellular convection are detailed in Chapter 3. Finally, an overall summary and conclusions from the research presented in this thesis is provided in Chapter 4.

CHAPTER 2: AEROSOL-CLOUD-LAND SURFACE INTERACTIONS WITHIN TROPICAL SEA BREEZE CONVECTION

2.1 Introduction

Some of the highest global annual rainfall totals on the order of 2-3 m yr^{-1} (Liebmann et al. 2012) are found in the equatorial rainforest regions of Africa, Amazonia, and Indonesia where tropical convection occurs year round. It is well known that convection in these regions plays a crucial role in the global circulation through its impacts on the ascending branch of the Hadley Cell (Riehl and Malkus 1958), and on the global hydrological cycle (Avissar and Werth 2005). However, these regions are under ever-increasing anthropogenic activity, including biomass burning and deforestation practices. Such anthropogenic activity may have significant impacts on the convective storm characteristics and rainfall patterns in these critical tropical rainforest regions through aspects such as changing land surface properties and atmospheric aerosol loading (e.g. Andreae et al. 2004; Ramos da Silva and Avissar 2006; Koren et al. 2008). It is therefore highly important to understand the response of convective storms to these anthropogenic factors if we are to understand the impacts of increasing human populations on tropical convection, tropical rainfall, and the large-scale circulation.

Convection in Africa is anomalous relative to the other equatorial land regions such as Amazonia and Indonesia (e.g. Mohr and Zipser 1996a,b; Mohr et al. 1999; Petersen and Rutledge 1998, 2001; McCollum et al. 2000). While annual rainfall in equatorial Africa is comparatively lower, convection is more intense by measures such as high (40-dBZ) reflectivity echo top height, minimum brightness temperature, and lightning flash rate (Zipser et al. 2006). Mesoscale convective systems (MCSs) are also disproportionally larger in equatorial Africa

(Nesbitt et al. 2006). The reasons for these differences are not well understood. Rainfall patterns over equatorial Africa are also highly spatially variable (Balas et al. 2007). Part of this variability is likely a result of mesoscale-organized convection due to features such as sea- and lake-breezes, topography, and larger-scale features modulating convective activity including convectively-coupled Kelvin waves, the Madden-Julian oscillation, and midlevel easterly jets (Laing et al. 2011; Jackson et al. 2009).

The sea breeze represents a persistent forcing mechanism for deep convection and rainfall. Its importance, particularly in the diurnal cycle of rainfall, has been noted in several studies of deep convection in the tropics (Yang and Slingo 2001; Nesbitt and Zipser 2003; Kikuchi and Wang 2008), as well as in equatorial Africa (Laing et al. 2008, 2011). Many studies have demonstrated the sensitivity of the sea breeze structure, local convergence, and resulting precipitation to various processes and mechanisms including sensible heat fluxes, soil moisture, surface roughness length, coastline curvature, and interaction with existing boundaries such as land breezes, other sea breezes, and gust fronts (Wakimoto and Atkins 1994; Atkins et al. 1995; Kingsmill 1995; Fankhauser et al. 1995; Wilson and Megenhardt 1997; Carbone et al. 2000; Baker et al. 2001; Fovell and Dailey 2001; Marshall et al. 2004; Fovell 2005; Crosman and Horel 2010 and references therein). Sea breeze generated precipitation may also be sensitive to changes in aerosol concentrations through aerosol direct effects and indirect effects on the storm dynamics and microphysics (e.g. Andreae et al. 2004; Khain et al. 2005; van den Heever et al. 2006; Koren et al. 2004, 2008; Lin et al. 2006).

While many studies have investigated aerosol-cloud interactions and land-atmosphere interactions separately, very few have considered the synergistic interactions among them within a common analytical framework. The goal of this research is therefore to investigate the potential

sensitivity of sea breeze convection over coastal equatorial Africa to changes in aerosol concentrations and land surface characteristics, both independently and synergistically. Such changes to the surface and aerosol characteristics are possible with increasing anthropogenic activity, pollution, and deforestation practices, which are often focused in coastal regions (Hinrichsen 1999). Specifically, this study seeks to answer the following questions: (1) what are the mechanisms by which changing aerosol number concentrations, surface roughness length, and soil moisture each individually impact tropical sea breeze precipitation; and (2) how do aerosols interact synergistically with land surface processes to influence the precipitation? These goals are addressed through the use of idealized cloud-resolving modeling simulations.

In this study, it will be demonstrated that the individual impacts of increasing aerosol concentrations and decreasing soil moisture both reduce the sea breeze precipitation, while changes to the surface roughness length only have a slight impact on the precipitation. It will also be shown that the pathway through which aerosols and land surface processes interact synergistically to affect rainfall is through feedbacks to the localized sea breeze convergence by storm-generated gust fronts. The sensitivity of rainfall to these various factors and their interactions is assessed through the analysis of changes to the basic ingredients for deep, moist convection: *moisture instability*, *and lift* (e.g. Doswell 1987; Johns and Doswell 1992). Section 2.2 describes the model configuration, the sensitivity experiments, and the factor separation methodology used for the analysis. The results are presented in section 2.3, including the mechanisms by which the various processes and their interactions change the sea breeze structure and resulting precipitation. A discussion and conclusions are provided in section 2.4.

2.2 Experiment Design

a. RAMS model configuration

In this study, idealized simulations were conducted using the Regional Atmospheric Modeling system (RAMS) version 6 (Cotton et al. 2003; Saleeby and van den Heever 2013). RAMS is a regional, non-hydrostatic model that contains a sophisticated microphysics and aerosol parameterization scheme and is coupled to the Land-Ecosystem-Atmosphere-Feedback (LEAF) version 3 land surface parameterization (Walko et al. 2000). RAMS is thus an ideal modeling framework with which the goals of this study can be addressed. A summary of the RAMS model configuration is provided in Table 2.1.

The RAMS simulations presented herein contain a single grid of 550 x 200 km extent, a horizontal grid spacing of one km, and 57 vertical levels spanning ~26 km with a minimum vertical grid spacing of 100 m near the surface. The grid resolution is fine enough to explicitly represent deep convection, such as suggested by Ramos da Silva and Avissar (2006) for simulations over the Amazon, and to model the detailed sea breeze structure (Crosman and Horel 2010), but coarse enough that a large number of sensitivity simulations may be performed in a realistic time frame. Simulations were run for 16 hours, beginning at 700 local time (LT). The Harrington (1997) two-stream radiation scheme was utilized for these experiments.

The RAMS microphysics scheme is a sophisticated double-moment bulk scheme with bin-emulating procedures for cloud droplet nucleation, riming, and sedimentation. The scheme utilizes a gamma size distribution to represent eight hydrometeor classes, including cloud water, drizzle, rain, pristine ice, snow, aggregates, graupel and hail. RAMS contains nine possible different aerosol modes for four aerosol particle types, but given the idealized setup of these simulations, only a sub-micron ammonium sulfate mode was used here. Sulfates are a prevalent

aerosol type in the atmosphere, serve as effective cloud condensation nuclei (CCN) due to their high solubility, and are often associated with anthropogenic activity (e.g. Andreae and Rosenfeld 2008, and references therein). Aerosols do not have sources and sinks and are radiatively active in these simulations. Aerosol-radiative interactions are parameterized from Mie Theory in RAMS. The reader is referred to Walko et al. (1995), Meyers et al. (1997), Saleeby and Cotton (2004, 2008), and Saleeby and van den Heever (2013) for further details on the RAMS microphysics scheme and aerosol treatment.

The horizontally homogeneous but vertically varying initial thermodynamic conditions were generated from the European Centre for Medium-Range Weather Forecasts (ECMWF) analyses for the Year of Tropical Convection (YOTC). Temperature, specific humidity, and winds at 600 UTC (700 LT) were averaged spatially from 0 °N to 4 °N and from 10 °E to 20 °E, broadly encompassing the Cameroon rainforest region, and temporally from 1 June through 31 August for 2008 and 2009 to create the initial sounding profile for the idealized simulations (Fig. 2.1a). The thermodynamic conditions are therefore representative of one of equatorial Africa's dry seasons, when anthropogenic activity and deforestation practices are more active. Above 300 hPa, the specific humidity was reduced by a factor of two-thirds from the YOTC moisture profile based on the results of Ciesielski et al. (2014), where it was shown that ECMWF moisture analyses are too humid in the upper levels in comparison to high accuracy, humidity-corrected rawinsonde measurements taken during the Dynamics of the Madden-Julian Oscillation field campaign. Random temperature perturbations were introduced at each grid point within the lowest two km AGL, with a maximum of 1 K at the surface. The random perturbations disrupt the homogeneity of the initial environment and allow the idealized sea breeze to evolve realistically, as will be seen in the analysis of Figs. 2.3 and 2.4 below.

RAMS is coupled to the LEAF-3 model, an interactive land surface model containing 22 different surface types and 12 soil classes (Walko et al. 2000). LEAF prognoses temperature and moisture content for multiple soil levels, the vegetation surface, and the vegetation canopy. The land surface and atmosphere interact through turbulent energy and moisture exchange, radiative transfer, transpiration, and precipitation. Eleven soil levels from 0.01 m to 0.5 m below ground were used in these simulations. The LEAF surface classes chosen for the domain setup are representative of the coastal Cameroon rainforest region: the eastern two-thirds of the domain were specified as evergreen broadleaf tree with a sandy clay loam soil type (Rodell et al. 2004) and the western third as ocean with a fixed sea surface temperature (SST) of 300 K, based on the average coastal SST in June, July, and August from the YOTC dataset. The approximate domain size and the forest-ocean partition within the domain are indicated in Fig. 2.1b in order to provide a sense of the grid scale. Boundary conditions were open radiative on the east and west sides of the domain, but periodic on the north and south sides so that the simulated domain is representative of an idealized coastline stretching to both the north and south. It should be noted that we are not assessing the impact of coastline curvature on sea breeze convergence and resulting convective precipitation in this study, and hence we prescribe the imposed ocean-forest border to be perfectly straight. To avoid any potential influence of the model lateral boundary conditions, the region within 50 km of the east and west borders is excluded from the analysis throughout this study.

b. Sensitivity experiments and analysis methodology

To address the goals of this study, 27 simulations with varying aerosol concentrations, values of surface roughness length, and soil moisture contents were conducted. For each of the

three parameters, two different perturbation values were used from the values chosen in the control (hereafter CTL) simulation: a moderate perturbation, and an extreme perturbation. The initial surface aerosol concentration in CTL was 200 cm^{-3}. The two perturbation surface values used were 500 cm^{-3} and 2000 cm^{-3}; these simulations will be referred to as cMid and cPoll, respectively, where the "c" refers to aerosol particles that can serve as CCN. The CTL surface concentration is representative of clean continental conditions. Similar concentrations have been measured in pristine conditions in Amazonia (Roberts et al. 2001; Gunthe et al. 2009). The extreme value of 2000 cm^{-3} was chosen based measurements in the Amazon, where aerosol number concentrations of up to 10,000 cm^{-3} have been measured near the surface during periods of biomass burning (Martin et al. 2010, and references therein). In each case, the aerosol number concentration profile was linearly decreased to one tenth of the surface concentration by 4 km AGL and was held constant thereafter. The aerosol number concentration profiles for CTL, cMid, and cPoll are displayed in Fig. 2.2.

The two surface parameters that were varied in these experiments were the roughness length and soil moisture. The initial roughness length in CTL is 3.50 m, which is calculated within the LEAF model from the default evergreen broadleaf class vegetation height of 32 m. The perturbation roughness length values of 1.64 m and 0.22 m were calculated by specifying two perturbation tree heights of 15 m and 2 m, respectively; these simulations will be referred to as tMid and tSml, respectively. Soil moisture was initialized horizontally homogeneously by setting the soil moisture saturation in CTL to 75% saturated for all soil levels, which corresponds to a soil moisture content of 0.315 m^3 m^{-3} for the sandy clay loam soil type chosen for these simulations. Idealized perturbation soil moisture values were simply specified at 50% saturated and 25% saturated (s50 and s25), corresponding to volumetric soil moisture contents of 0.21 and

0.105 m^3 m^{-3}, respectively. Similar idealized approaches to soil moisture initialization have also been used in previous studies (Jiang and Feingold 2006; Gero and Pitman 2006; Ramos da Silva and Avissar 2006; Saad et al. 2010). The initial roughness length and soil moisture for CTL and the sensitivity experiments are also depicted in Fig. 2.2. The CTL simulation is therefore the least polluted simulation with the wettest soil and the highest surface roughness length.

It should be noted that we have not simply altered the land surface type for the sensitivity experiments, as is sometimes done in studies of deforestation impacts. The reasons for this are threefold. Firstly, in reality the land surface type is usually not completely altered under deforestation scenarios; often, secondary forest regrowth occurs, and the land surface properties are similar to those of the original forest (O'Brien 2000; Pielke et al. 2007). In this scenario, one might expect the most significantly altered surface parameter to be the roughness length due to the smaller tree heights. Secondly, soil moisture is often substantially altered through land use changes (Pielke et al. 2007 and references therein), and has been shown in numerous studies to have a strong impact on land-atmosphere coupling by virtue of its control over the latent and sensible surface energy flux partition, and thus its influence on surface-driven buoyancy and moisture availability for cloud and precipitation formation (e.g. Yu et al. 2002; Ramos da Silva and Avissar 2006; Betts 2007, 2009; Taylor et al. 2012). Thirdly, it is beneficial to directly and independently test specific parameters and their influence on rainfall. Changing the vegetation type altogether results in changing multiple surface parameters at once (e.g. roughness length, albedo, root zone depth, leaf area index, etc.), and the resulting changes to clouds and rainfall patterns may then be attributable to the effects of multiple parameters as well as their interactions. This makes it difficult to assess the actual processes at work and the individual roles of the different land surface properties.

In order to understand how aerosols, clouds, and surface processes may interact synergistically, the factor separation methodology of Stein and Alpert (1993) was utilized for this analysis. Factor separation is a simple and elegant way to show how multiple factors, as well as their nonlinear interactions, influence a predicted field. Factor separation has been successfully used in many modeling studies of atmospheric processes, such as lee cyclogenesis (Alpert et al. 1996), aerosol impacts on convective precipitation (van den Heever et al. 2006; Seigel et al. 2013), the influence of land-cover change on convective storm development (Gero and Pitman 2006), and sea breeze structure (Darby et al. 2002).

Each of the three parameters tested (aerosol concentrations, roughness length, and soil moisture) represents one factor that can impact the spatial and temporal convective rainfall patterns. Generally, 2^n simulations are required to assess how n different factors and their nonlinear interactions influence a solution. Since we used three possible initial values for each of three factors, 3^3=27 simulations were necessary. The simulation numbers and names, the corresponding factor separation name, and the factor separation formula used to calculate the influence of each factor and the synergistic interactions amongst factors are summarized in Table 2.2. The naming convention to be used throughout the rest of this study will be as follows: simulation 1 will always be called “CTL,” and the sensitivity experiments are referenced by the labels “c” (aerosols or potential **CCN**), “t” (roughness length or **tree** height), and “s” (**soil** moisture), followed by the perturbation description. If a particular label is not included, this means that the value for that factor is the same as in CTL. For example, “cMid-tSml-s25” refers to the simulation with the moderate aerosol perturbation and the most extreme roughness length and soil moisture perturbations, while “cPoll-s50” refers to the simulation with the most polluted

aerosol concentrations and the 50% saturated soil moisture perturbation, but with the original, largest value of roughness length as in CTL.

2.3 Results

a. CTL sea breeze and precipitation characteristics

Many of the following figures are presented as subsets relative to the location of the sea breeze front. In order to identify the sea breeze front location at each model output time (every 5 minutes), the zonal wind was first averaged meridionally and over the lowest 1 km AGL, and then smoothed to obtain an average zonal wind profile in the east-west direction. The sea breeze location was then identified by finding the location of the minimum in the gradient of the smoothed averaged wind profile. This point corresponds to the x-location of the maximum averaged zonal wind convergence, which was simply extrapolated to all points in y for simplicity, representing the sea breeze front as a straight line.

Figure 2.3 displays the vertically averaged 0-1 km zonal wind, the identified sea breeze location, and precipitation rate from 1400-1900 LT for CTL. At 1400 LT (Fig. 2.3a), the sea breeze front is well defined by virtue of the differential heating of the land surface that has occurred throughout the morning hours. The sea breeze then propagates eastward and serves as a focal point for convection through convergence at its leading edge. The precipitation rates associated with the sea breeze are increasing at 1400 LT and maximize between ~1700 and 1800 LT (Fig. 2.3d-e). Most of the sea breeze precipitation dissipates by 2200 LT, one hour before the end of the simulation. It can be seen in Fig. 2.3 that both the sea breeze front identification based on the average low-level zonal wind convergence and the linear sea breeze approximation are

reasonable. The sea breeze front does vary spatially, especially as it interacts with gust fronts produced by storms ahead of the sea breeze, but this variation is usually not more than 5-10 km.

In order to further demonstrate the structure of the sea breeze and how it changes in some of the sensitivity experiments, the sea breeze strength expressed in terms of its density potential temperature perturbation, the cold pools associated with smaller convective cells ahead of the sea breeze, and vertically integrated condensate are depicted in Fig. 2.4 at 1630 LT for simulations CTL, cPoll, s25, and cPoll-s25. The more intense convection associated with the sea breeze front occurs as the sea breeze collides with cold pools. An example can be seen in CTL at ~x=280, y=20, where the interaction between a cold pool and the sea breeze front has caused the integrated condensate to exceed 25 mm. The precipitation associated with this convective development exceeds 50 mm hr^{-1} at 1700 LT (Fig. 2.3d, at the same grid coordinates). It is apparent from the example shown in Fig. 2.4 that changing both aerosol concentrations and soil moisture, independently and simultaneously, impact the sea breeze strength, structure, and propagation, as well as the cloud field and cold pools in the eastern portion of the domain. These changes will be discussed in further detail in the following sections.

Given the idealized nature of the simulations, the intent is not to reproduce the rainfall patterns for a specific event over the Cameroon rainforest. However, it is helpful to know whether the model produces reasonable rainfall totals for this region at this time of year. The precipitation rate in CTL averaged spatially over the forest region and temporally between 1300 and 2200 LT is ~0.34 mm hr^{-1}. The average precipitation rate over 24 hours would then be ~0.13 mm hr^{-1}. This represents a lower-limit approximation for the simulated average precipitation rates, since it assumes that all the precipitation occurs in the afternoon in association with the sea breeze forcing. For comparison, the 24-hour accumulated precipitation between the 6 hour and

30 hour YOTC forecasts initialized at 12 UTC was calculated for each day in June, July, and August in 2008 and 2009 and then temporally averaged (Fig. 2.1b). The ECMWF YOTC average precipitation rate varies between ~0.2 and 0.4 mm hr^{-1} along the Cameroon rainforest coast between 1 °N and 4 °N. Additionally, these precipitation rates appear to agree favorably with estimates of annual mean precipitation from observations (e.g. Liebmann et al. 2012, their Figs. 1 and 2). Therefore, the accumulated precipitation associated with the sea breeze convection in the idealized RAMS simulations appears reasonable. The changes to the sea breeze precipitation in each sensitivity experiment are discussed in the next section. The processes by which aerosol concentrations, roughness length, soil moisture, and their sets of nonlinear interactions influence the precipitation amounts and patterns are then investigated by analyzing their impacts on the three ingredients for convection: moisture, instability, and lift.

b. Sensitivity experiments: Changes in precipitation

Figure 2.5 displays the domain total accumulated precipitation at the end of the simulation (2300 LT) for all 27 simulations (top panel), and the results of the factor separation calculation (bottom panel). The naming convention of each simulation is as described in Table 2.2. Note that the simulations are color coded according to whether they include only one factor, different pairs of factors, or all three factors. The same colors are used throughout the rest of the figures in this chapter for clarity.

The highest accumulated precipitation occurs in simulation 5 (tSml), followed closely by CTL. It is immediately obvious that enhanced aerosol concentrations and reduced soil moisture both individually reduce precipitation totals, by over 40% and 50% for the most extreme perturbations (Fig. 2.5). The trends in total precipitation due to reduced roughness length are

nonmonotonic, but the changes in precipitation are quite small. The lowest total accumulated precipitation occurs in simulation 25 (cPoll-tMid-s25) where total precipitation is reduced from CTL by almost 70%.

By including the simulations containing the combinations of factors (simulations 8-27), the synergistic interactions occurring between the factors can be assessed. It is important to note that these synergy terms, as calculated with the factor separation formulas and displayed in Fig. 2.5, represent the nonlinear interactions, or feedbacks, acting between the different factors. For example, the synergy between aerosols and soil moisture can either enhance or reduce the rainfall *relative* to the change in rainfall that would occur if the *separate, individual* impacts of aerosols and soil moisture were added together. The results of the factor separation calculation displayed in the bottom panel of Fig. 2.5 indicate that all the double synergistic interactions between pairs of factors (simulations 8-19) work to enhance total precipitation, while almost all the triple synergistic interactions (simulations 20-27) reduce total precipitation. The interpretation of these signs is not trivial and is discussed in further detail in section 3.3f. Note that the double synergy terms are largest for aerosol-soil moisture interactions (simulations 12-15), and that the magnitudes of the double synergy terms for aerosol-roughness length interactions (simulations 8-11) are all larger than the impacts of roughness length itself (simulations 4-5).

The separate impacts of (1) increased aerosol concentrations, (2) reduced surface roughness length, (3) reduced soil moisture, and then the synergistic interactions amongst these three factors on the precipitation fields, as well as a discussion of the processes responsible for the precipitation trends noted above, are presented in the following four sections.

c. Enhanced aerosol concentrations

This section focuses on the reduction in accumulated precipitation seen in simulations cMid and cPoll relative to CTL (Fig. 2.5). Ammonium sulfate aerosols are effective scatterers of solar radiation; thus when aerosol concentrations are enhanced, the amount of incoming solar radiation is reduced. Fig. 2.6 displays profiles of downwelling clear sky solar radiation averaged ahead of the sea breeze from 1300 to 1600 LT when incoming solar radiation is near its peak. It is clear that the incoming solar radiation is decreased throughout the atmosphere in cMid and cPoll relative to CTL, especially below ~3 km where the aerosol perturbation is concentrated. The downwelling shortwave at the surface is reduced by 16 W m^{-2} (2.1 %) and 102 W m^{-2} (13 %) in cMid and cPoll, respectively.

Reduced incoming shortwave radiation results in lower surface temperatures in the polluted scenarios. Since the temperature difference between land and ocean is the fundamental driver of the sea breeze, the sea breeze itself weakens, as demonstrated in Hovmöller diagrams of the meridionally and 0-1 km AGL vertically averaged zonal wind speed in CTL and the differences between cMid or cPoll and CTL (Fig. 2.7). Wind speeds both behind the sea breeze front and ahead of the sea breeze are weaker in cMid and cPoll. The sea breeze front is also displaced farther west, by ~40 km in cPoll at 2200 LT (Fig. 2.7). The weaker wind speeds and more slowly-progressing sea breeze decrease the mean sea breeze convergence by ~4% and 14% in cMid and cPoll, respectively. As the convection is driven by the sea breeze, and most of the intense convection is focused just behind the sea breeze front (Fig. 2.3), the accumulated precipitation is lower in cMid and cPoll than in CTL.

In addition to lower surface temperatures under enhanced aerosol concentrations, evapotranspiration from the vegetation canopy and the soil is also reduced since the amount of

incoming solar radiation at the surface is smaller. Surface latent heat fluxes (LHF) and sensible heat fluxes (SHF) are reduced by ~4% and ~6% in cMid and by 21% and ~26% in cPoll, respectively (Table 2.3). The Bowen ratio (SHF/LHF), which represents the surface energy flux partition, is slightly smaller under more polluted conditions, since the reduction in SHF is greater than the reduction in LHF. Such aerosol-radiative interactions and subsequent reductions in the surface fluxes, with resultant implications for cloud formation, have also been noted in previous observational and modeling studies (Yu et al. 2002; Koren et al. 2004, 2008; Feingold et al. 2005; Jiang and Feingold 2006; Zhang et al. 2008). Therefore, all three ingredients for convection – moisture from evapotranspiration, instability achieved through surface heating, and sea breeze convergence forcing for ascent – are weakened under scenarios of enhanced aerosol concentrations, explaining the reductions in accumulated precipitation (Fig. 2.5).

d. Reduced surface roughness length

In this section, changes to the ingredients for convection with decreasing roughness length in simulations 1, 4, and 5 (CTL, tMid, and tSml) are investigated in order to understand why the roughness length does not have a large impact on the sea breeze precipitation (Fig. 2.5). Cross sections of zonal wind speed relative to the sea breeze front in CTL, and differences between the roughness length sensitivity experiments and CTL (Fig. 2.8), demonstrate changes to the structure of the sea breeze in simulations tMid and tSml. A smaller value of surface roughness length results in reduced friction velocity and weaker momentum transfer between the surface and lower atmosphere. The net result of these effects is that near-surface zonal wind speeds are stronger, particularly behind the sea breeze but also out ahead of the sea breeze front (Fig. 2.8).

The changes in near-surface wind speeds in and around the sea breeze front impact the profile of convergence (Fig. 2.9). The peak convergence associated with the sea breeze front is closer to the surface by up to several hundred meters in the smaller surface roughness cases. Convergence at the surface is also enhanced by ~17% and ~47% in tMid and tSml. Gero and Pitman (2006) have also demonstrated sensitivity of the sea breeze convergence and resulting convection over the Sydney Basin to changes in the roughness length. Enhanced convergence closer to the surface is more favorable for convection, since the lift associated with the convergence will supply higher moisture and energy from closer to the surface to the developing convection. However, perturbations to the surface roughness length also change the partitioning between surface SHF and LHF. The SHF increases by up to ~15% while LHF decreases by up to ~11% as roughness length decreases, which increases the Bowen ratio (Table 2.3), in agreement with previous studies (Garratt 1993). The change in the Bowen ratio with decreasing roughness length occurs because the efficiency of turbulent energy transfer from the canopy to the lower atmosphere decreases, which allows larger surface temperatures to build up and consequently the SHF to increase. While the stronger SHF strengthens surface-driven buoyancy and warms the near-surface air, thereby steepening the low level lapse rate, the smaller LHF reduces the amount of moisture available to the convection. The net result of these two effects is a reduction in the Convective Available Potential Energy (CAPE) ahead of the sea breeze.

In reality, it is likely that other land surface parameters, such as leaf area index (LAI) and rooting depth, are also altered when the roughness length is decreased, although often all three of these surface parameters increase toward their original values under scenarios of reforestation (Mahmood et al. 2014). The duration of these idealized simulations is not long enough for precipitation and evaporation to change the soil moisture below a depth of 0.3 m. Therefore, the

results presented herein are not expected to be sensitive to the root zone depth, since the smallest root depth for any vegetation type in LEAF is 0.7 m. In order to test the sensitivity to LAI, additional simulations were performed in which LAI was varied between ~0.5 and 6 for the smallest roughness length case, where 6 is the maximum value of LAI for the LEAF evergreen broadleaf vegetation class. It was found that LAI also has a nonmonotonic impact on the precipitation. The largest change in the magnitude of accumulated precipitation with changing LAI was ~7% relative to simulation tSml. The impacts of LAI are similar to those of roughness length in that a smaller LAI increases the Bowen ratio, which increases the strength of the sea breeze convergence but decreases the CAPE. These have competing effects on the convection, and thus the sea breeze precipitation is not very sensitive to changes in LAI associated with different roughness lengths, especially in comparison to the precipitation sensitivity to aerosols and soil moisture (Fig. 2.5).

In summary, the three ingredients for convection change in compensating ways when surface roughness length is decreased. While the strength of the convergence increases and its peak is closer to the surface, the low-level moisture and therefore CAPE both decrease. These competing effects on convection produce only small changes to the total rainfall.

e. Reduced soil moisture

The differences in rainfall between simulations 1, 6, and 7 (CTL, s50, and s25) are discussed in this section. It was seen in section 3.3b that the accumulated rainfall is substantially reduced as soil moisture content is decreased to 25% saturation. It is also clear from Fig. 2.5 that the precipitation responds nonlinearly to a linear decrease in soil moisture content. The sea breeze structure response to the soil moisture perturbation is also highly nonlinear, as evidenced

in the Hovmöller plots of zonal wind speed (Fig. 2.10). The wind speeds behind the sea breeze are stronger and the sea breeze front is 15 km farther eastward at 2200 LT in simulation s25 compared to CTL, in agreement with previous studies demonstrating changes to the sea breeze propagation speed with varying soil moisture (Physick 1980; Miao et al. 2003). Due to these changes in the zonal wind speed, the sea breeze convergence is significantly enhanced, by up to 100% at ~1km AGL in s25 (not shown), although it is only very slightly enhanced in s50 relative to CTL.

The sea breeze is stronger in s25 because the LHF is reduced while the SHF is enhanced, and hence the Bowen ratio is increased, under drier soil conditions (Table 2.3), in agreement with previous studies (Physick 1980; Kala et al. 2010). Again it is apparent that the increase (decrease) in SHF (LHF) responds highly nonlinearly to the soil moisture perturbation. This nonlinear response is a result of the parameterized vegetation becoming stressed when the soil moisture is reduced to 25% saturation. Since more of the shortwave radiation absorbed at the surface is utilized to increase the surface temperature rather than to flux water to the atmosphere under lower soil moisture scenarios, the forest-ocean temperature gradient increases. The sea breeze strength therefore also increases, and it accelerates inland more quickly. Robinson et al. (2013) have also recently demonstrated this result within idealized simulations of sea breeze propagation under varying magnitudes of surface heating.

In summary, reduced soil moisture alters the three ingredients for convection in opposing ways. Although the convergence associated with the sea breeze front strengthens, the reduction in the LHF limits the amount of moisture and therefore CAPE available to the convection. Near-surface vapor mixing ratios are reduced by 0.6 g kg^{-1} (4 %) in s50 and by 3 g kg^{-1} (20 %) in s25. Therefore, the moisture reduction has the greatest control over the precipitation response in s25.

This result is similar to that described by Baker et al. (2001); they showed that precipitation associated with Florida sea breeze convection was higher over wetter soils because low-level moisture and instability were increased. Ramos da Silva and Avissar (2006) also found that wetter soil conditions led to more precipitation in simulations of convection over Amazonia. The impact of reduced soil moisture on the sea breeze precipitation is analogous to the impact of reduced roughness length, wherein convergence is strengthened but an increase in the Bowen ratio results in less available moisture and CAPE. The net result is a reduction in accumulated precipitation, although the effect is much stronger for the soil moisture perturbations than for the roughness length perturbations (e.g. Table 2.3 and Fig. 2.5).

f. Synergistic interactions

In this section, possible feedbacks to rainfall patterns resulting from the nonlinear interactions of aerosols and land surface processes are discussed. Recall that the bottom panel of Fig. 2.5 displays the results of the factor separation calculations. It should be emphasized that the double and triple synergy terms are not simply the differences in rainfall between each simulation and CTL, but rather represent the contributions of the synergistic interactions that occur only when both effects are present (Table 2.2). For simulations 8-19, the factor separation calculation therefore represents the impact on the rainfall that is solely due to the interaction, or synergy, between the pairs of factors being considered by subtracting out the individual separate contributions of each factor. In simulations 20-27, the triple interactions between aerosols, roughness length, and soil moisture are demonstrated.

The factor separation results for total precipitation (Fig. 2.5) demonstrate that the double synergies all act to enhance total rainfall, while the triple interaction reduces rainfall. However,

care must be taken in interpreting the synergy calculation when one of the factors dominates the solution (Alpert and Sholokhman 2011). For instance, the accumulated precipitation is reduced by almost 60% when soil moisture is reduced to 25% saturation (Fig. 2.5). Additionally, for the most polluted aerosol scenario, total precipitation is reduced by ~40%. Since the individual impact of each of these factors is large, a negative feedback by synergy between these two effects naturally arises from the calculation (Table 2.2) because accumulated rainfall is a finite quantity that cannot be reduced indefinitely. In these scenarios, the synergy terms are not as meaningful because the individual impacts of soil moisture and aerosols dominate the rainfall changes.

On the other hand, feedbacks and more meaningful synergy contributions emerge when perturbations are moderate or the rainfall response to the individual factor is small. For instance, the synergy between roughness length and aerosols always increases rainfall, and almost always by more than the individual impact of roughness length itself (Fig. 2.5). Also, interestingly, while precipitation is reduced in both cMid and s50 relative to CTL as described above, the accumulated precipitation in simulation cMid-s50 is larger than in either cMid or s50 itself, indicating the importance of the synergistic interactions that act to enhance rainfall in this case. The magnitude of the contribution by synergy to the rainfall enhancement is ~20%, which is larger than the individual magnitudes of the rainfall reduction by cMid and s50. This synergy represents a negative feedback to the rainfall, since it acts in opposition to the individual negative impacts of aerosols and soil moisture. The processes responsible for the rainfall enhancement by synergistic interactions between aerosols and soil moisture for moderate perturbations are next explored to demonstrate how such nonlinear interactions arise.

A time series of the rate of change of the accumulated precipitation over the forest region (Fig. 2.11) demonstrates that the enhanced precipitation by cMid-s50 synergy occurs primarily in the latter half of the analysis period. The most significant enhancement in terms of the precipitation rate magnitude and percentage increase occurs between 1900-2100 LT as the sea breeze convection diminishes. In simulation cMid-s50, individual convective towers develop ahead of the sea breeze between 1800-1830 LT. Their respective outflows at 1905 LT, which are characterized by strong divergence at the centers and convergence along their edges, are evident in Fig. 2.12 at ~x=350, y=80 km. These outflows interact with the sea breeze front, locally enhancing convergence and further increasing convection behind the sea breeze front from 1900-2000 LT. Additionally, convergence is enhanced directly to the north and south of where the outflows intersect the sea breeze front. Vertically integrated condensate begins to increase there, similarly to the mechanism described in Droegemeier and Wilhelmson (1985). Although convection along the sea breeze still occurs toward the end of the simulations in CTL, cMid, and s50, such as the convection seen at x=350, y=120 in CTL (Fig. 2.12) after the sea breeze interacts with an older remnant cold pool, strong individual convective towers ahead of the sea breeze are only able to develop in cMid-s50, when both enhanced aerosol concentrations and reduced soil moisture are included. The presence of this convection and the subsequent enhancement of the sea breeze precipitation resulting from its outflow therefore demonstrates how the nonlinear interactions between aerosols and soil moisture operate. This result is broadly consistent with the findings in Baker et al. (2001). They indicated that nonlinear interactions between coastline curvature and land-breeze circulations increase precipitation due to local enhancements in sea breeze convergence resulting from gust fronts.

The formation of the convection ahead of the sea breeze in cMid-s50 can be understood as follows: in more polluted scenarios, there are fewer clouds ahead of the sea breeze, as demonstrated by the average total condensate profile shown in Fig. 2.13. This occurs due to the reduced surface fluxes as well as smaller cloud droplets and hence enhanced evaporation rates with increased aerosol concentrations (not shown). Similar results have been found in previous studies (e.g. Koren et al. 2004; Feingold et al. 2005; Jiang and Feingold 2006; Xue and Feingold 2006). Thus, although the surface fluxes are reduced with enhanced aerosol concentrations (Table 2.3), the evening CAPE ahead of the sea breeze is larger in cMid because less convection has utilized and hence erased the instability in this region. When soil moisture is reduced and the Bowen ratio increases, the surface buoyancy forcing increases and moisture decreases. This results in enhanced cloudiness above ~3 km (Fig. 2.13) and fewer clouds that develop into deep convection under drier soil conditions. Additionally, cold pools ahead of the sea breeze are stronger on average by 0.11 K (~13%) in s50 and by 0.14 K (~17%) in s25 relative to CTL in terms of their density potential temperature perturbations, which is evident qualitatively in Fig. 2.4. It is only when both of these effects are present (larger evening instability with enhanced aerosols and stronger surface buoyancy fluxes and forcing by cold pool outflows with reduced soil moisture) that evening convection ahead of the sea breeze is able to develop and subsequently interact with the sea breeze to locally enhance the precipitation.

The simulation results for cMid-s50 also suggest that, similarly, stronger isolated convection develops ahead of the sea breeze between 1630-1700 LT which leads to the enhanced precipitation by cMid-s50 synergy between 1700-1800 LT that can be seen in Fig. 2.11. Moreover, even though the boundary layer moisture reduction in s25 dominates the impact on rainfall, a similar sequence of events occurs in the other simulations containing both enhanced

aerosols and reduced soil moisture. Finally, the nonlinear interactions between enhanced aerosols and roughness length are analogous to those between aerosols and soil moisture because reductions in roughness length also result in a larger Bowen ratio and stronger convective outflows, as in the simulations with reduced soil moisture. Factor separation calculations indicate that synergistic interactions between aerosols and roughness length enhance the sea breeze convergence (not shown), which enhances the rainfall.

To summarize, soil moisture and aerosol loading individually dominate the impacts on rainfall when the perturbations are extreme, but the nonlinear interactions between aerosols and soil moisture and between aerosols and roughness length are significant when aerosol and soil moisture perturbations are more moderate. These interactions arise through their synergistic impacts on the third ingredient for convection, the lifting mechanism. This result demonstrates the chaotic nature of convection, as has also been noted by Carbone et al. (2000) for observations of organized convection initially forced by sea breeze and gust front interactions over the Tiwi Islands, and by Baker et al. (2001) within Florida sea breeze simulations. The sensitivity of convective rainfall to small changes in the ingredients for convection and hence initial convective forcing in these simulations highlights this chaotic nature, since the enhanced rainfall by synergy depends solely on the presence or absence of relatively stronger convection that initiates ahead of sea breeze. In turn, the gust fronts locally enhance the sea breeze convergence and therefore the sea breeze precipitation.

2.4 Summary and Discussion

In this study, the relative influences of aerosols, surface roughness length, and soil moisture, as well as their synergistic interactions, on the rainfall resulting from tropical

convection focused along a sea breeze front have been investigated through the use of idealized cloud-resolving modeling simulations. The impacts of these factors and their interactions on the rainfall were investigated by analyzing the three ingredients for convection: moisture, instability, and lift. It was shown that enhanced aerosol number concentrations reduce the amount of shortwave radiation absorbed at the surface, resulting in less surface heating and smaller surface fluxes, a weaker sea breeze, and therefore reduced rainfall. Reduced soil moisture also reduces rainfall by changing the SHF and LHF partition and therefore the Bowen ratio; the smaller LHF results in less low-level moisture available to convection and consequently lower precipitation totals. A smaller surface roughness length leads to enhanced convergence along the sea breeze front but reduced moisture and instability. Changes to the roughness length therefore have competing effects on the ingredients for convection, and the net result is that changes to rainfall are small.

This study has also demonstrated that when the perturbations to aerosol concentrations or soil moisture are more extreme, their influences on the surface fluxes and available low-level moisture dominate the resulting changes to the sea breeze rainfall. However, nonlinear interactions between aerosols and land surface processes, particularly between aerosols and soil moisture, are more significant when their relative perturbations are more moderate. These interactions act to enhance rainfall, which represents a negative feedback to the precipitation, through their mutual impact on the sea breeze convergence and the gust fronts interacting with the sea breeze front. Therefore, these results indicate that the pathway through which such interactions between aerosols and land surface processes can occur is primarily through the low-level convergence.

Given the idealized nature of the simulations, these results are also likely to be more generally applicable to tropical rainforest convection initiated along other boundaries such as sea breezes in Amazonia and Indonesia, or lake breezes along Lake Victoria, which have been shown to be important forcing mechanisms for deep convection that contribute to the spatial pattern of rainfall over tropical rainforests (Kousky 1980; Laing et al. 2008, 2011; Vondou et al. 2010). However, the sensitivity to the initial thermodynamic and wind profile, which was representative of the coastal Cameroon rainforest region in this study, remains to be tested. It will also be important to account for other local factors that may modulate the sensitivities of the sea breeze convection to changing aerosol concentrations and land surface properties such as topography and coastline curvature (e.g. Baker et al. 2001; Darby et al. 2002; Miao et al. 2003), which have not been investigated in this study. Finally, it would be interesting to investigate possible precipitation feedbacks and the role of the land breeze and subsequent sea breezes in initiating and contributing to coastal rainfall totals over several days. Such investigations would require longer duration simulations and therefore lateral boundary nudging with reanalysis data.

The results of this study highlight the importance of considering mutual impacts of aerosols and land surface properties on clouds and precipitation, as their interactions can be significant. To our knowledge, only one other study has investigated aerosol-cloud-land surface interactions within a coupled system. In their simulations of cumulus convection over land, Jiang and Feingold (2006) found that the inclusion of radiative feedbacks to the surface fluxes by aerosols and clouds resulted in a reduction in the magnitude of the second aerosol indirect effect. Their findings therefore also demonstrate the importance of including such feedbacks. The results of the present study also point to the importance of accurately representing gust fronts and low-level convergence in model simulations, since this is an important mechanism through

which these feedbacks occur. Finally, this study underscores the need to account for the surface-cloud-atmosphere system responses to changes in aerosol loading and land surface properties in regional and large-scale models, especially as anthropogenic activity continues to impact tropical rainforest regions. Additional avenues for feedbacks between aerosols and surface processes likely also exist. For example, aerosols and clouds impact the diffuse and direct light partition, which influences evapotranspiration and vegetative carbon uptake (Gu et al. 2003; Lu et al. 2005; Matsui et al. 2008). The roughness length may also influence surface emissions of aerosols through changes in the near-surface winds (Cowie et al. 2013). Such feedbacks need to be considered in future studies of aerosol-cloud-land surface interactions.

2.5 Tables and Figures

Table 2.1. Summary of RAMS model options used in all the sea breeze simulations.

Model Aspect	**Setting**
Grid	Arakawa C grid $\Delta x = \Delta y = 1$ km; 550 km x 200 km domain size Δz variable minimum $\Delta z = 100$ m, maximum $\Delta z = 1$ km vertical stretch ratio = 1.05 57 vertical levels; model top ~26 km
Time integration	3 s time step; 16 hour simulation duration
Initialization	Horizontally homogeneous thermodynamic and wind profile, averaged from ECMWF YOTC analysis data Initial start time 600 UTC 1 July Random thermal perturbations through lowest 2 km AGL, with a maximum magnitude of 1 K at the lowest model level above ground
Surface scheme	LEAF-3 (Walko et al. 2000) 11 soil levels from 0.01 m to 0.5 m below ground Western third of domain: ocean (SST 300 K) Eastern two-thirds of domain: evergreen broadleaf tree surface type, sandy clay loam soil type
Boundary conditions	Radiative lateral boundary (Klemp and Wilhelmson 1978) in zonal direction; periodic in meridional direction Rayleigh friction damping over top 6 vertical levels (~21-26 km AGL)
Microphysics scheme	Two-moment bulk microphysics (Meyers et al. 1997) 8 hydrometeor classes (Saleeby and Cotton 2004)
Radiation scheme	Harrington (1997) two-stream, updated every 5 simulation minutes
Aerosol treatment	Aerosol species: sulfates (Saleeby and van den Heever 2013) No aerosol sources or sinks Aerosols radiatively active DeMott et al. (2010) Ice Nucleation parameterization
Turbulence scheme	Smagorinsky (1963) deformation-K with stability modifications by Hill (1974); stability modifications by Lilly (1962) used gradually above the boundary layer
Coriolis	No

Table 2.2. Summary of sensitivity experiment numbering, experiment names, factor separation formulas, and a physical description of the significance of the factor separation computation. Note that the simulations including a combination of moderate and extreme perturbations (e.g. simulation 9, cMid-tSml) are not displayed for brevity.

Simulation no. (factor name)	**Exp. name**	**Factor separation formula**	**Description**
1 (f0)	CTL	--	Base simulation (most pristine)
2 (f1a)	cMid	f1a-f0	Impact of moderate aerosol perturbation
3 (f1b)	cPoll	f1b-f0	Impact of extreme aerosol perturbation
4 (f2a)	tMid	f2a-f0	Impact of moderate roughness length perturbation
5 (f2b)	tSml	f2b-f0	Impact of extreme roughness length perturbation
6 (f3a)	s50	f3a-f0	Impact of moderate soil moisture perturbation
7 (f3b)	s25	f3b-f0	Impact of extreme soil moisture perturbation
8 (f1a2a)	cMid-tMid	f1a2a – (f1a+f2a) + f0	Double synergy between aerosols and roughness length for moderate perturbations
11 (f1b2b)	cPoll-tSml	f1b2b – (f1b+f2b) + f0	Double synergy between aerosols and roughness length for extreme perturbations
12 (f1a3a)	cMid-s50	f1a3a – (f1a+f3a) + f0	Double synergy between aerosols and soil moisture for moderate perturbations
15 (f1b3b)	cPoll-s25	f1b3b – (f1b+f3b) + f0	Double synergy between aerosols and soil moisture for extreme perturbations
16 (f2a3a)	tMid-s50	f2a3a – (f2a+f3a) + f0	Double synergy between roughness length and soil moisture for moderate perturbations
19 (f2b3b)	tSml-s25	f2b3b – (f2b+f3b) + f0	Double synergy between roughness length and soil moisture for extreme perturbations
20 (f1a2a3a)	cMid-tMid-s50	f1a2a3a – (f1a2a+f1a3a+f2a3a) + (f1a+f2a+f3a) – f0	Triple synergy between all three factors for moderate perturbations
27 (f1b2b3b)	cPoll-tSml-s25	f1b2b3b – (f1b2b+f1b3b+f2b3b) + (f1b+f2b+f3b) – f0	Triple synergy between all three factors for extreme perturbations

Table 2.3. Latent (LHF) and sensible (SHF) heat fluxes and the Bowen ratio, averaged spatially from 10 km ahead of the sea breeze to 50 km from the domain edge, and temporally from 1300-2200 LT, for simulations CTL, cMid, cPoll, tMid, tSml, s50, and s25. Percent differences from CTL are listed in parentheses.

Simulation name	**LHF (W m^{-2})**	**SHF (W m^{-2})**	**Bowen ratio (SHF/LHF)**
CTL	257.4	91.6	0.36
cMid	246.6 (-4.2 %)	86.5 (-5.6 %)	0.35 (-1.5 %)
cPoll	203.3 (-21.0 %)	67.7 (-26.1 %)	0.33 (-6.5 %)
tMid	248.4 (-3.5 %)	98.5 (+7.5 %)	0.40 (+11.3 %)
tSml	229.2 (-10.9 %)	105.8 (+15.4 %)	0.46 (+29.6 %)
s50	203.5 (-20.9 %)	106.6 (+16.7 %)	0.53 (+47.7 %)
s25	46.1 (-82.1 %)	218.9 (+139.0 %)	4.75 (+1235 %)

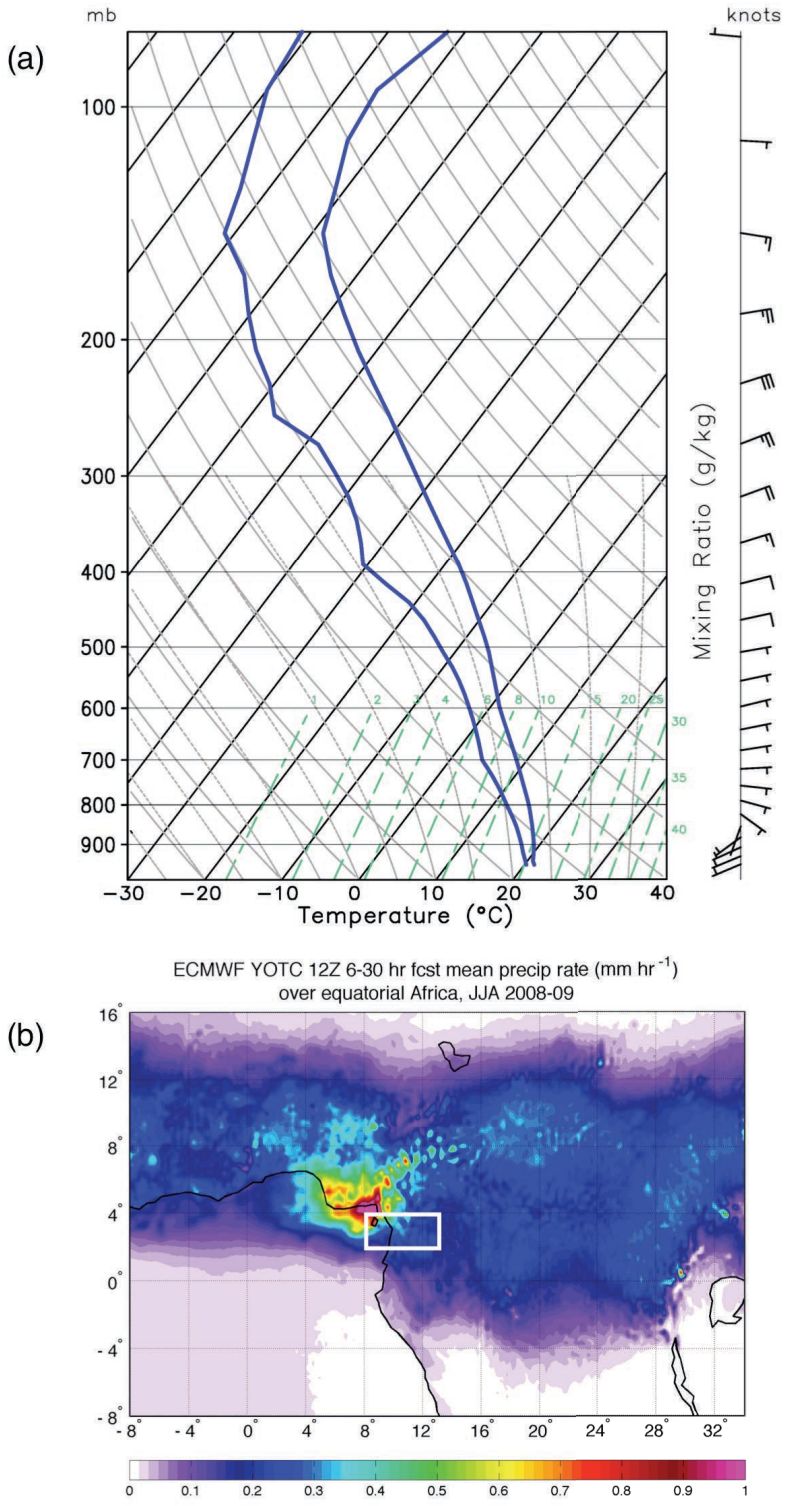

Fig. 2.1. (a) Initial thermodynamic temperature and dewpoint sounding, as well as the initial wind profile (barbs, knots), used in all of the idealized simulations. (b) Mean precipitation rate (mm hr^{-1}) over equatorial Africa, calculated from the ECMWF YOTC forecast data as described in the text. The white box indicates the approximate size of the domain used for the idealized simulations.

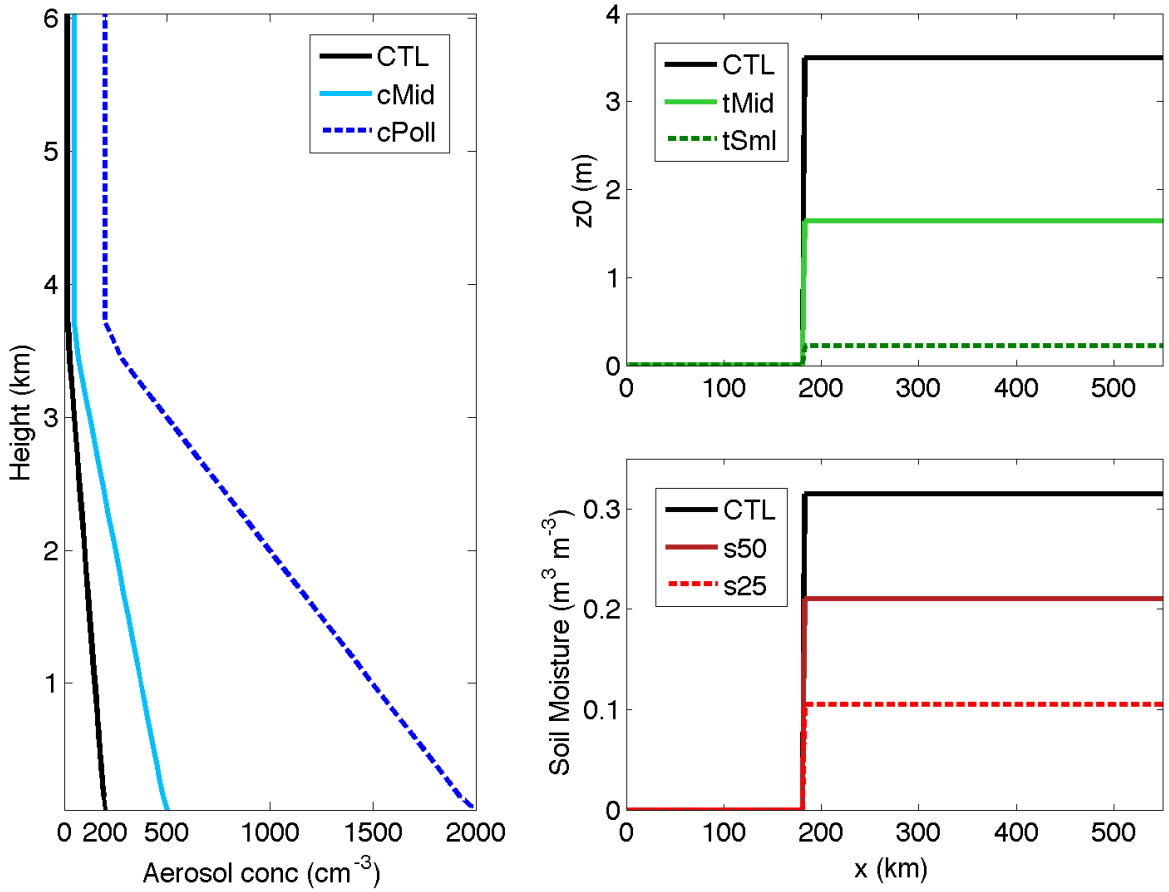

Fig. 2.2. Initial conditions for the control simulation (CTL) and the various sensitivity experiments. Left: aerosol number concentration profile (cm^{-3}) for CTL and the polluted conditions (cMid and cPoll) used for the sensitivity tests. Top right: surface roughness length (m) as a function of east-west position for CTL and sensitivity experiments tMid and tSml. Bottom right: volumetric soil moisture content (m^3 m^{-3}) as a function of east-west position for CTL (75% soil moisture saturation) and for the 50% and 25% saturation sensitivity experiments (s50 and s25). Note that the western third of the domain is ocean.

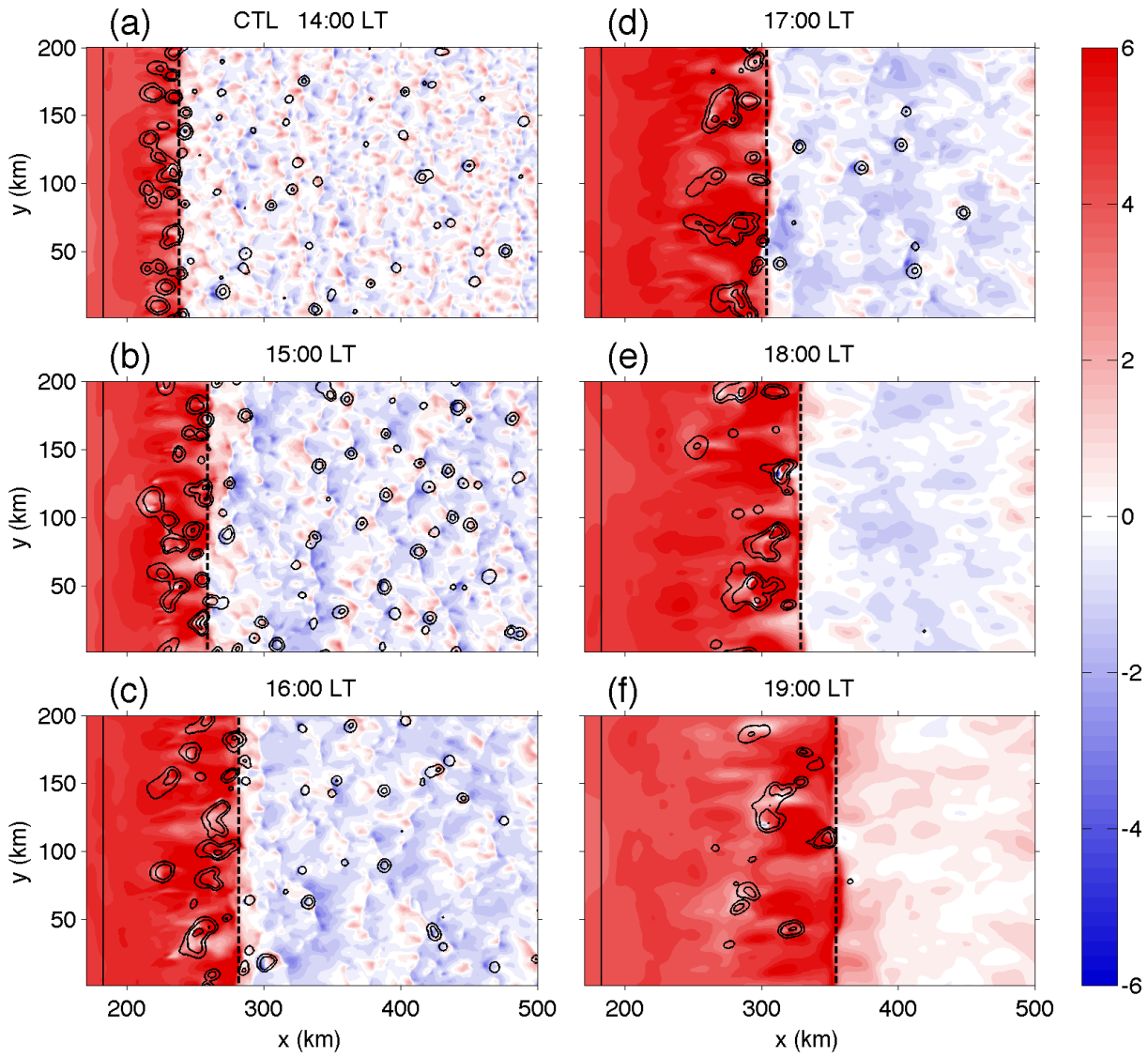

Fig. 2.3. Zonal wind vertically averaged over the lowest 1 km (m s^{-1}, shaded) and precipitation rate (0.5, 5, and 50 mm hr^{-1}, solid contours) for simulation CTL, from (a)-(f) 1400-1900 LT as indicated in each panel. The thin solid line at ~x=180 km denotes the ocean-forest border. The thick dashed black line is the identified sea breeze from the averaged convergence as described in the text.

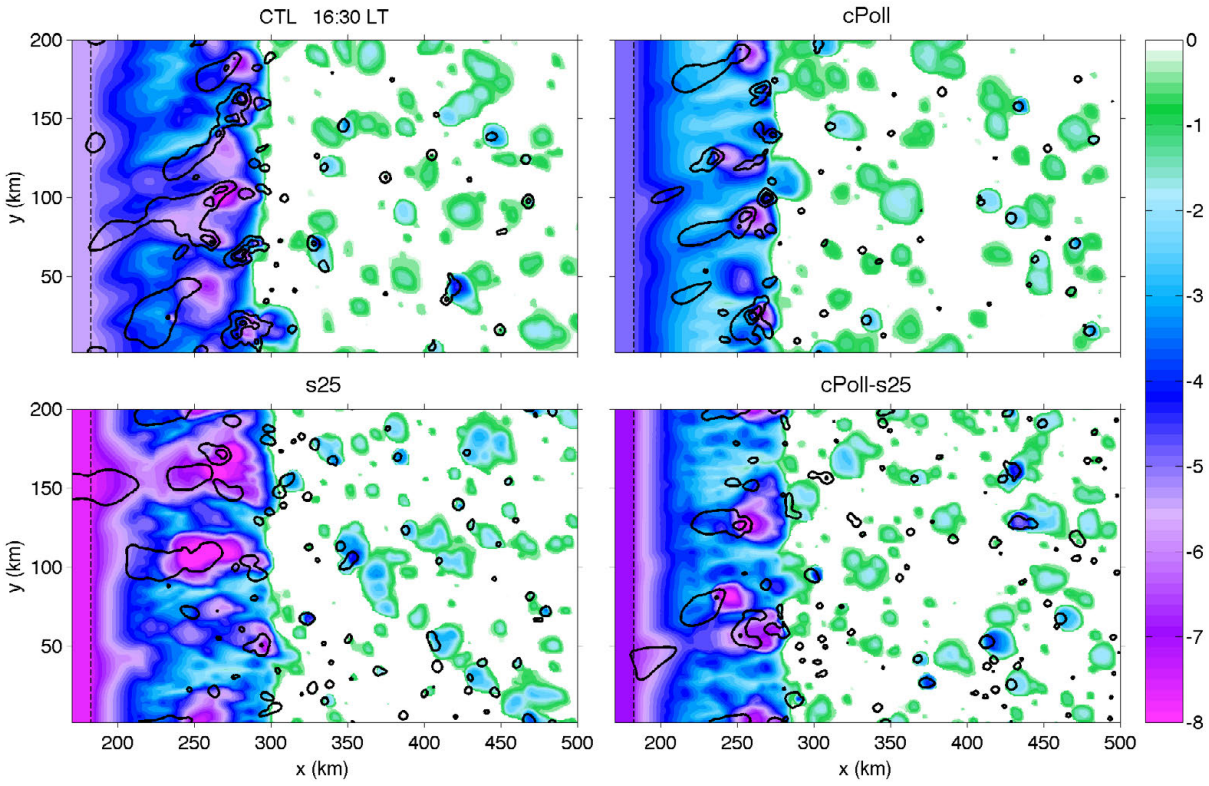

Fig. 2.4. Perturbation density potential temperature (K, shaded) at the lowest model level within identified cold pools where buoyancy < -0.005 m s^{-2}, following the methodology of Tompkins (2001); and vertically integrated condensate (0.5, 10, and 25 mm solid contours) for simulations CTL, cPoll, s25, and cPoll-s25 at 1630 LT. The mean density potential temperature is determined by spatially averaging the density potential temperature from 10 km ahead of the sea breeze front to 50 km from the east border of the domain. The thin dashed line denotes the forest-ocean border.

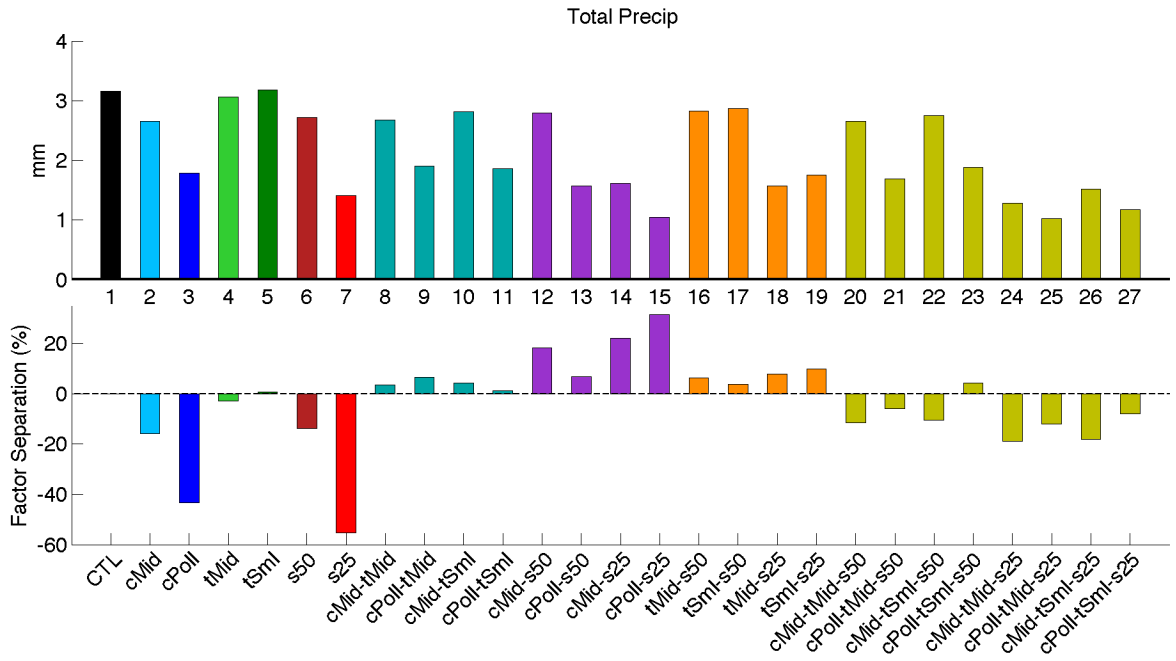

Fig. 2.5. Top panel: Averaged accumulated surface precipitation (mm) over the forest region at the end of the simulation for all 27 experiments as numbered in the top panel and labeled in the bottom panel. Bottom panel: results of the factor separation calculation (Table 2.2), expressed as a percent difference from CTL. The values displayed for simulations 8-27 are not simply percent differences from CTL, as described in the text. Factor separation for simulations 8-19 represents double synergistic interactions between pairs of factors, and the triple synergistic interactions are represented in simulations 20-27.

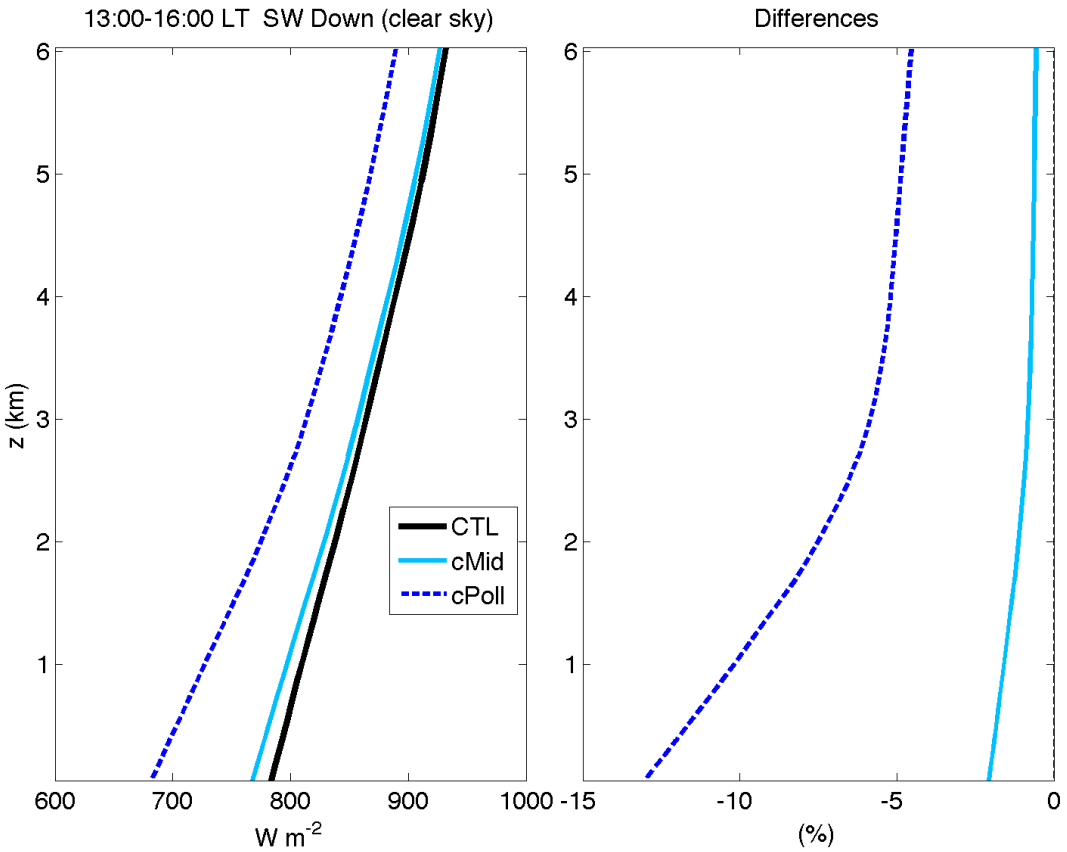

Fig. 2.6. (Left) Downwelling shortwave radiation (W m^{-2}) and (right) percent change from CTL for simulations CTL, cMid, and cPoll, averaged from 1300-1600 LT and from 10 km ahead of the sea breeze front (in order to avoid any spatial variation in the sea breeze front location) to 50 km from the eastern domain edge for clear-sky columns only. Clear-sky columns required that total condensate < 0.01 g kg^{-1} everywhere throughout the column.

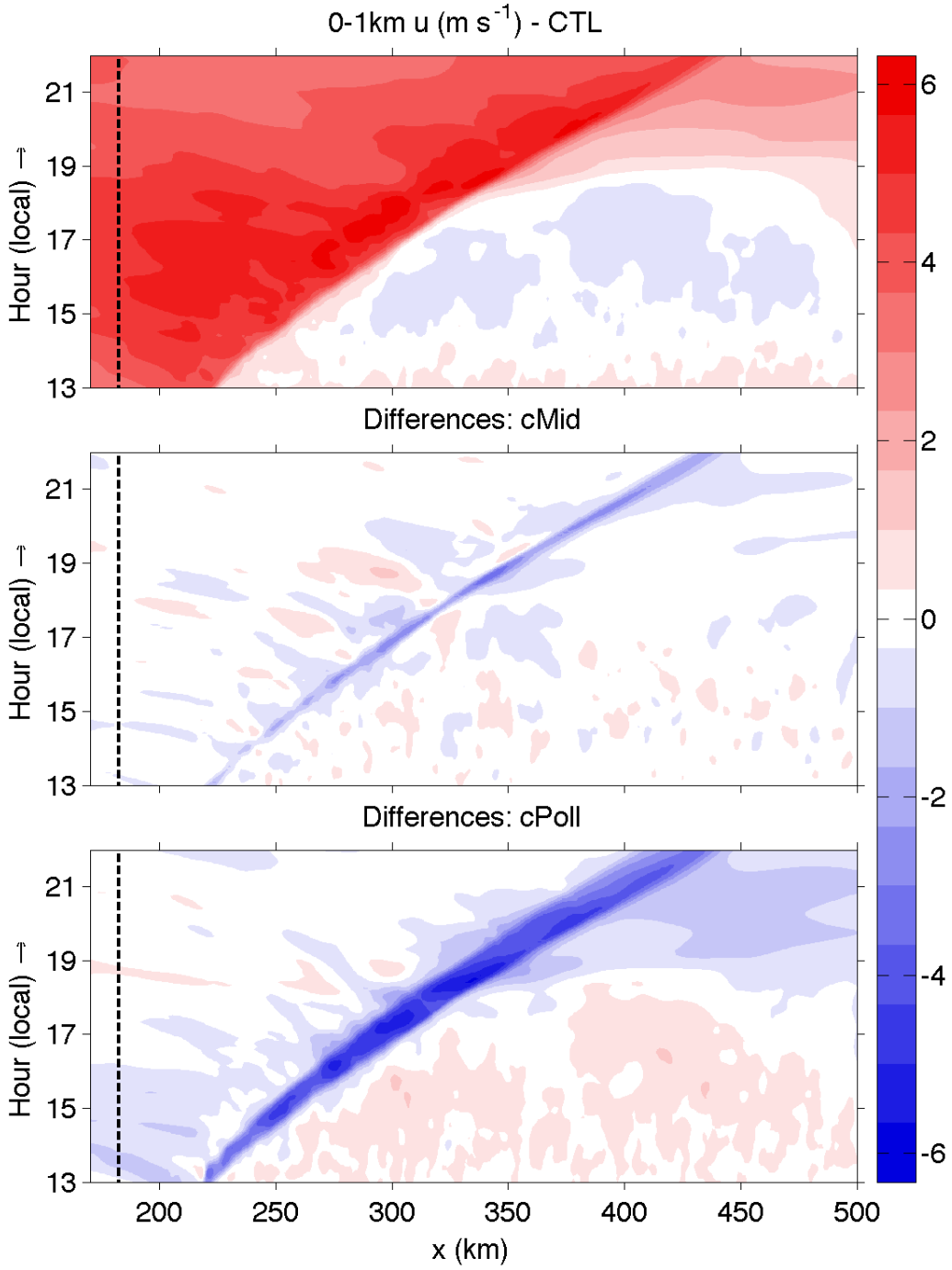

Fig. 2.7. Top panel: Hovmöller diagram of zonal wind (m s^{-1}, shaded) averaged meridionally and over the lowest 1 km for simulation CTL. Middle and bottom panels: difference field for the zonal wind Hovmöller diagrams between simulations cMid and CTL (middle) and cPoll and CTL (bottom). The dashed black line denotes the forest-ocean border.

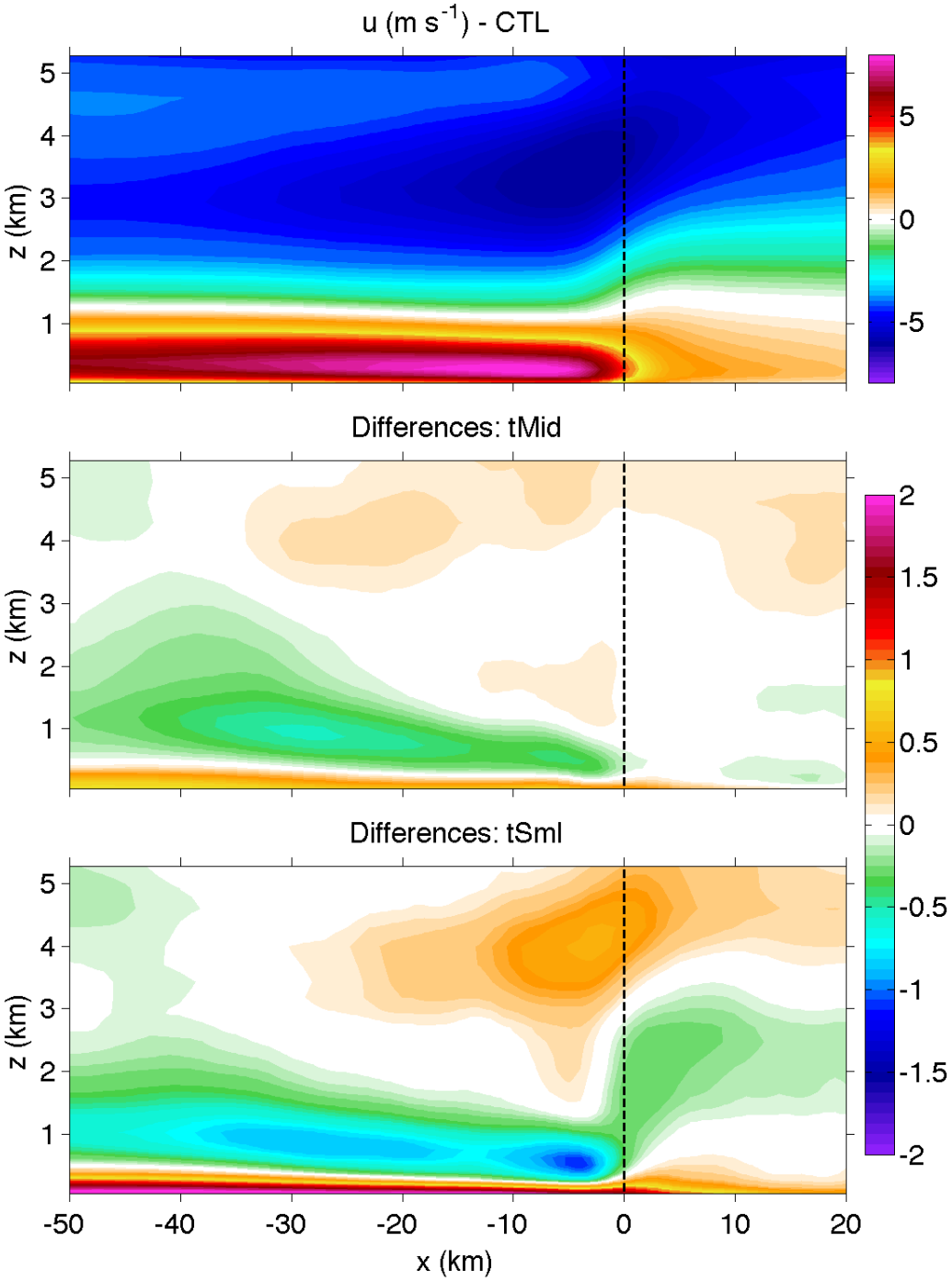

Fig. 2.8. Top panel: composite cross section of zonal wind speed (m s^{-1}, shaded) relative to the sea breeze front (at x=0), averaged meridionally and from 1300-2200 LT for simulation CTL. Middle and bottom panels: difference fields for the composite zonal wind cross sections between simulations tMid and CTL (middle) and tSml and CTL (bottom).

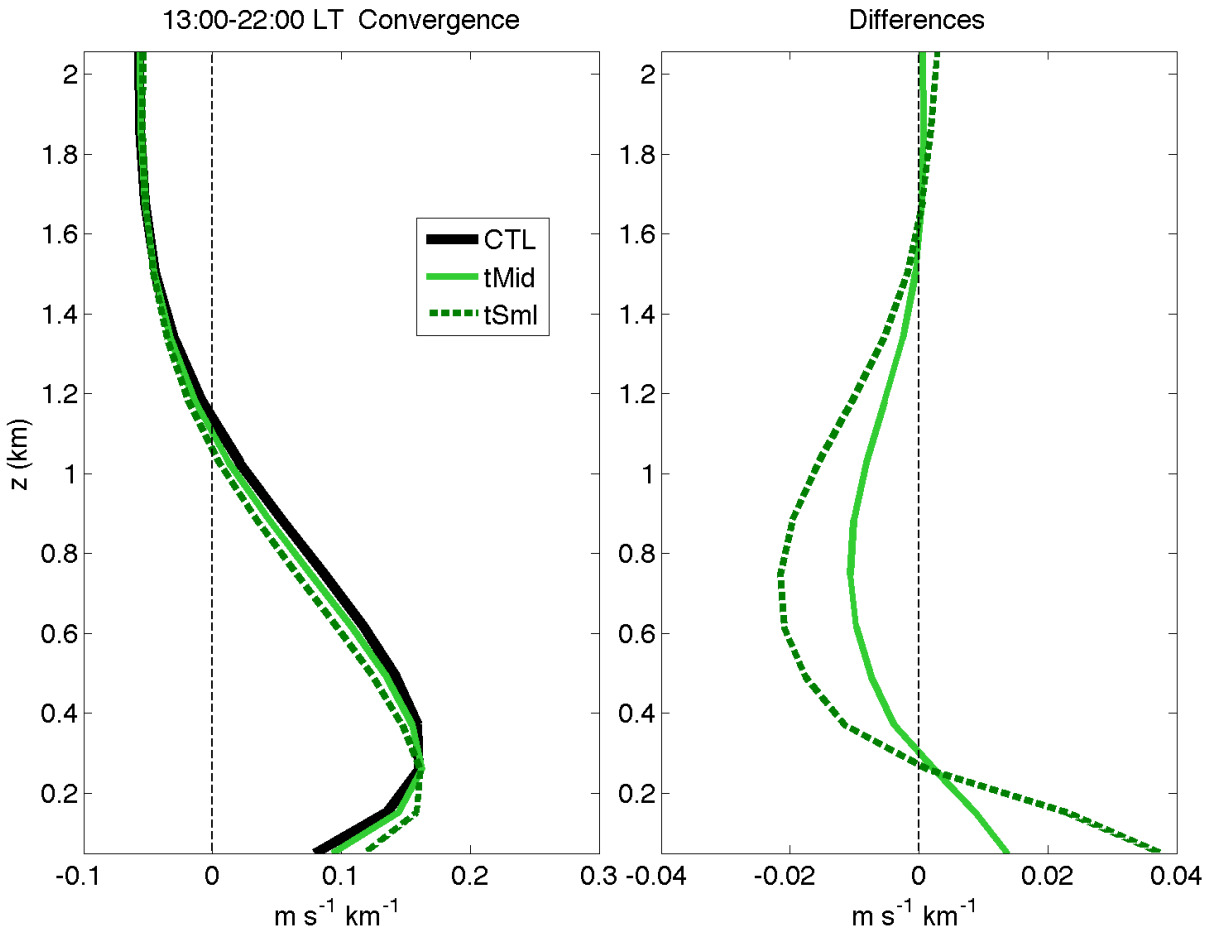

Fig. 2.9. (Left) Profiles of convergence (m s^{-1} km^{-1}) and (right) differences from CTL for simulations CTL, tMid, and tSml, averaged from 20 km behind to 20 km ahead of the sea breeze front and from 1300-2200 LT.

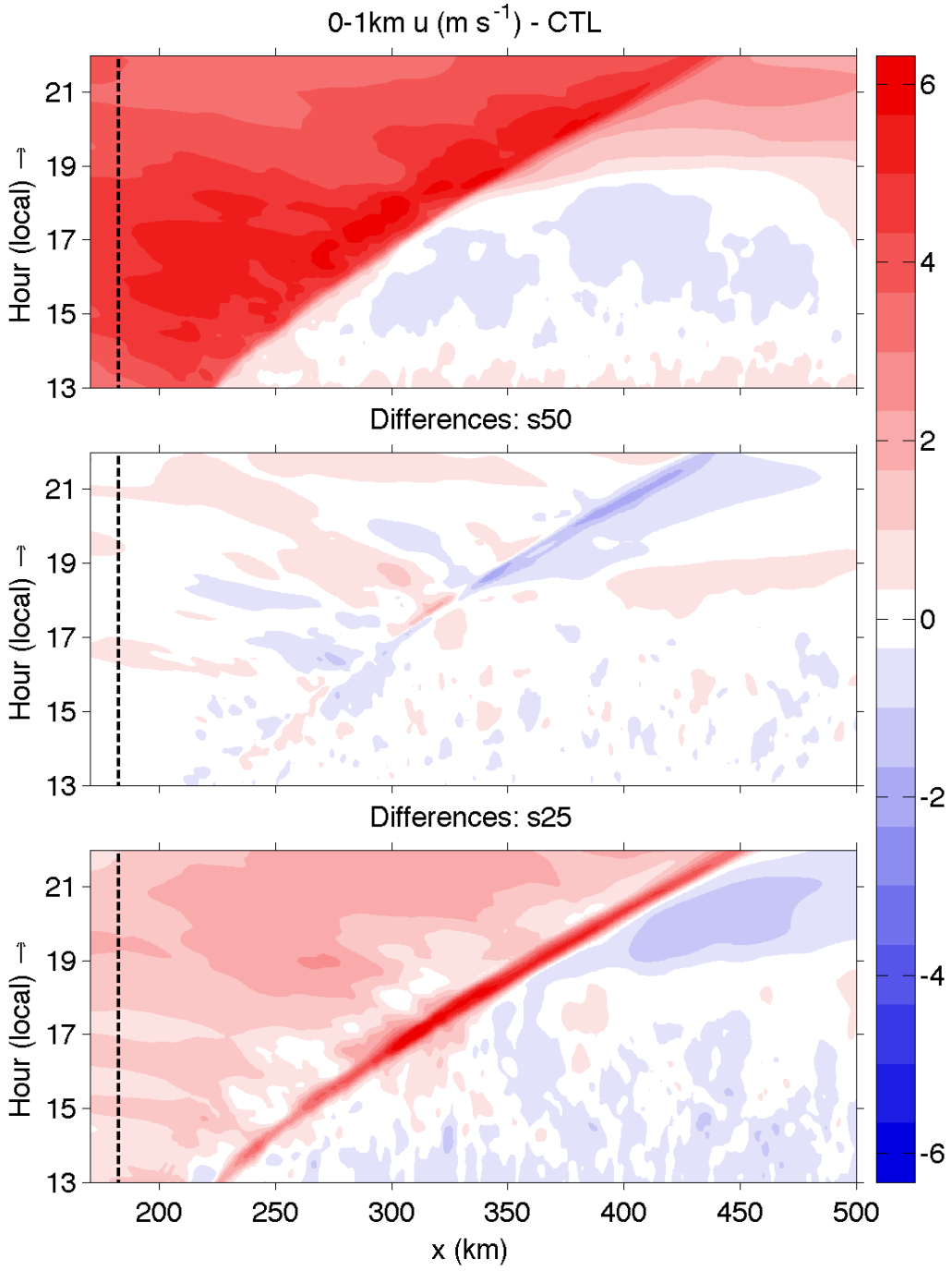

Fig. 2.10. As in Fig. 2.7, but for simulations CTL, s50, and s25.

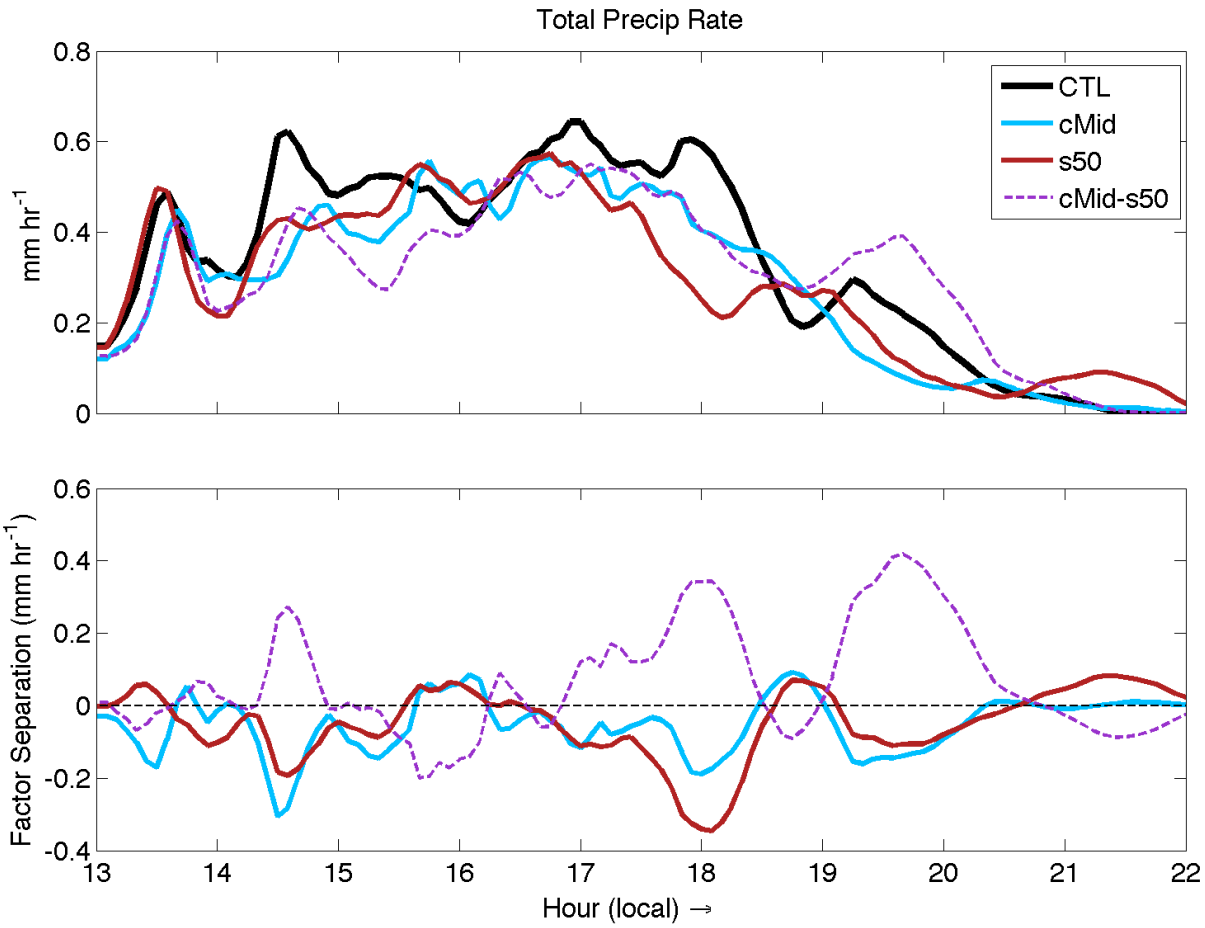

Fig. 2.11. Time series of the rate of change of accumulated precipitation (mm hr^{-1}) averaged over the forest region (top) and the factor separation calculation (bottom) for simulations CTL, cMid, s50, and cMid-s50. Note that the cMid-s50 line in the bottom panel represents the double synergy term.

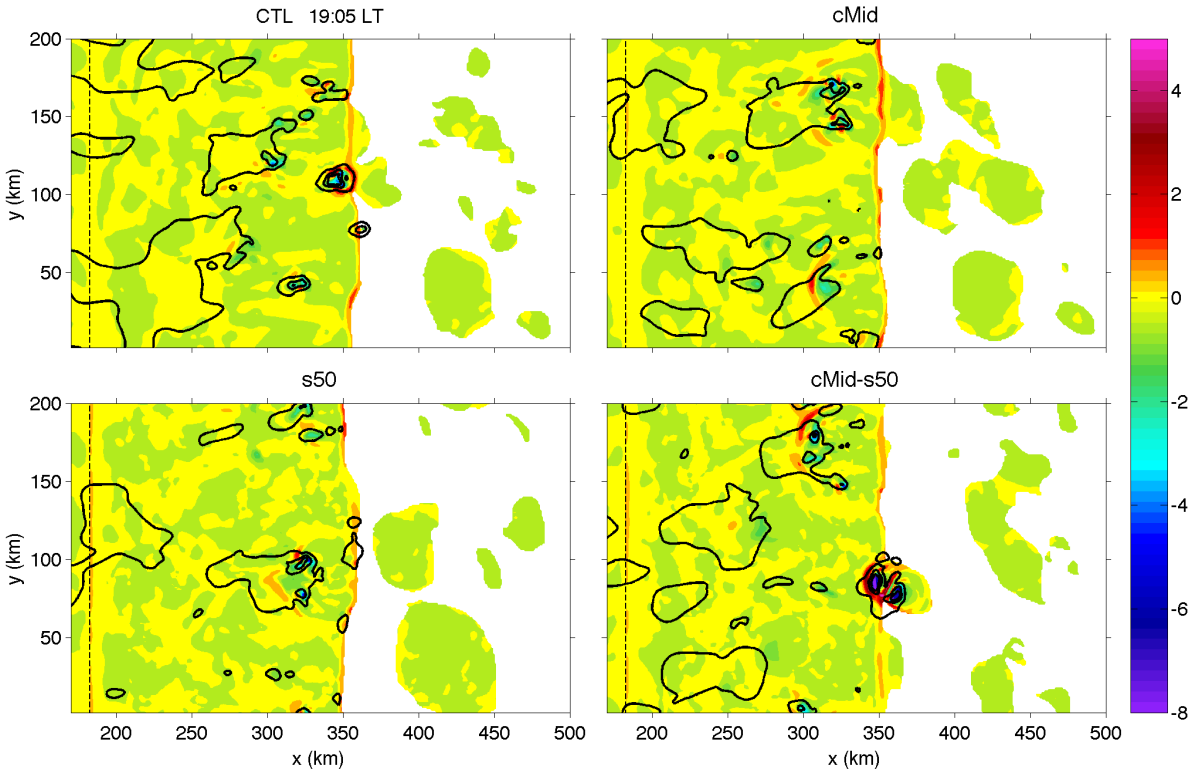

Fig. 2.12. Convergence at the lowest model level (m s^{-1} km^{-1}, shaded only within identified cold pools, as in Fig. 2.4) and vertically integrated condensate (0.5, 10, and 25 mm, solid contours) for simulations CTL, cMid, s50, and cMid-s50 at 1905 LT. The thin dashed line denotes the forest-ocean border.

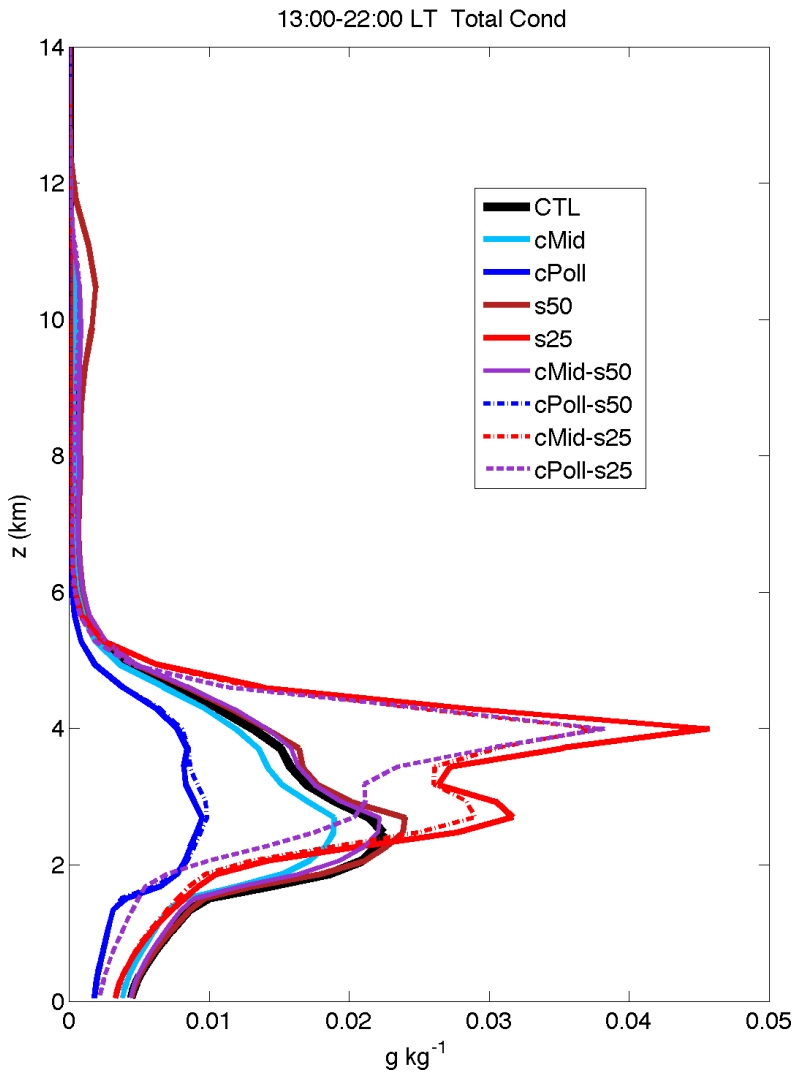

Fig. 2.13. Profiles of total condensate (g kg^{-1}) averaged spatially from 10 km ahead of the sea breeze front to 50 km from the eastern domain edge, and temporally from 1300-2200 LT.

CHAPTER 3: THE RELATIVE IMPACT OF MIDLEVEL DRYNESS AND AEROSOLS ON MIDLATITUDE DEEP CONVECTIVE MORPHOLOGY

3.1 Introduction

The supercell storm spectrum represents a continuum of supercell types, but which are commonly divided into three main classes: low-precipitation (LP), classic (CL), and high-precipitation (HP) supercells. LPs have strong and long-lived rotating updrafts, as do all supercells, but their precipitation rates are comparatively weaker. They are low precipitation efficiency storms even amongst supercells, which themselves are a low-precipitation efficiency storm class (Browning 1977).

More intense precipitation is typically located within the forward-flank downdraft (FFD) region in LPs, while the rear-flank downdraft (RFD) and updraft core usually contain only a few large hydrometeors (Bluestein and Parks 1983, hereafter BP83; Bluestein 1984). Additionally, observations of LPs report narrow updrafts often located to the rear of the main radar echo that may be tilted or upright, hail and large raindrops falling from the anvil, and a lack of strong cold pools (Davies-Jones et al. 1976; Burgess and Davies-Jones 1979, hereafter BD79; BP83; Bluestein 1984; Bluestein and Woodall 1990; Moller et al. 1994). Observations of significant overshooting tops (e.g., up to 4 km above the equilibrium level reported in BD79) indicate that LP supercells are not simply weaker versions of their classic counterparts. Though LPs are often isolated, they sometimes occur in relatively close proximity to CL supercells or other convection; in these cases, the LP is typically the furthest upwind of the storms (BP83; Rasmussen and Straka 1998, hereafter RS98). LPs form most frequently in the high plains of the U.S. and along the dryline (BD79; Moller et al. 1994).

The mechanisms that distinguish LP from CL supercells are not well understood, though a number of hypotheses have been put forward. Brooks et al. (1994) suggest that the strength of the low- and mid-level wind shear can affect which supercell archetype forms through its impacts on the strength of the mesocyclone, storm-relative winds, and advection of hydrometeors within the storm. RS98 hypothesize, based on environmental sounding data, that upper-level storm-relative winds and upper-level humidity are potential discriminators. BD79 first noted the connection between LPs and the dryline, highlighting the potential importance of low-level moisture; BP83 also found that LPs form in environments that are drier (all the LP storms in their study occurred near the dryline). Background aerosol concentrations, through their impact on collision-coalescence processes (Weisman and Bluestein 1985; Bluestein and Woodall 1990), and the size of the initial convective element (BP83; Brooks and Wilhelmson 1992) have also been suggested as storm morphology discriminators.

Environmental factors leading to LP supercells are not well understood because (1) observations of LP supercells are limited due to the subjectivity of their classification and difficulty to detect with radar; and (2) high-resolution simulations with sophisticated microphysics have not yet been performed (Beatty et al. 2008). In one modeling study, an LP-like storm was simulated by artificially shutting off rain formation in the model and forcing all condensed water to remain as cloud water (Weisman and Bluestein 1985). In another study, Brooks and Wilhelmson (1992) used a smaller warm bubble for storm initialization and likened the resulting storm precipitation characteristics to an LP supercell. However, the simulated LP storm contained weak updrafts of less than 10 m s^{-1}.

Though it is not known which factor(s) lead to LP supercells, the environments in which they typically form are often characterized by elevated dry layers and by enhanced background

aerosol concentrations from dust sources in Texas and New Mexico (Prospero et al. 2002), front range pollution, or wildfires. Furthermore, LPs sometimes occur near other deep convection, including both supercells and multicells. The goal of the research presented here is therefore threefold: (1) to investigate the relative sensitivity of supercell storm morphology both to changes in the vertical moisture profile and to the background aerosol concentrations, and the physical processes by which these varying environmental characteristics impact supercellular storm structure; (2) to assess whether differences in the dynamical and microphysical characteristics of these supercell types do exist and hence produce their differing precipitation distributions; and (3) to understand how the sensitivity of nearby multicellular convection to both midlevel dryness and aerosols differs from that of the supercells.

To address these goals, idealized simulations of supercell storms were performed with a cloud-resolving model. A storm-splitting regime was first simulated in which the right-moving cell evolves into a CL supercell. Next, because dry layers are common in environments where LPs occur, the environmental moisture profile was systematically altered by adding dry layers of varying magnitudes and altitudes. Finally, background aerosol concentrations were then enhanced for three of the moisture profiles. It will be shown in this study that LP supercells form in both clean and polluted conditions when elevated dry layers are present. The microphysical structure and dominant hail growth mechanisms are found to differ in LPs compared to CL supercells. The broad dynamical structure, however, is similar amongst the different storm types. It will also be demonstrated that supercell morphology is relatively insensitive to aerosol concentrations. Finally, while the neighboring multicellular convection is also most strongly impacted by the presence of midlevel dryness, aerosols do influence the precipitation resulting from the left-mover through feedbacks to the strength of the cold pool.

The organization of this chapter is as follows: section 3.2 describes the model used and the design of the sensitivity experiments. Section 3.3 presents the results of the dry layer simulations, focusing on the right-moving storm. Section 3.3 includes (a) an overview of the simulation evolutions and supercell precipitation characteristics; (b) a comparison of the simulated supercell structure and dynamical features; (c) an analysis of microphysical fields and budgets; and (d) different hail growth mechanisms in the CL and LPs. The results of the aerosol sensitivity tests, including a discussion of both the dominant supercell and the multicellular convection, are presented in section 3.4. In section 3.5, previous hypotheses regarding supercell morphology, future work, and potential applications for forecasting are discussed. A summary is provided in section 3.6.

3.2 Model Setup and Experiment Design

The Regional Atmospheric Modeling System (RAMS) version 6 was used to achieve the goals of this study (Cotton et al. 2003; Saleeby and van den Heever 2013). RAMS is a non-hydrostatic, regional model appropriate for simulating a wide range of scales of atmospheric phenomena. For these experiments, RAMS was set up as a cloud-resolving model with 300 m horizontal grid spacing and a single grid with a domain size of 285 by 225 km. The vertical grid spacing was 25 m at the surface and was vertically stretched to a maximum of 300 m. The domain top was located approximately 22 km above ground level (AGL; all heights are AGL from here on). There were 92 vertical levels, 17 of which were below 1 km. The time step was one second, and experiments were run for three simulation hours. The model configuration is detailed in Table 3.1.

RAMS uses a sophisticated two-moment bulk microphysics scheme which prognoses mass and number concentration for eight hydrometeor classes: cloud, drizzle, rain, pristine ice, snow, aggregates, graupel, and hail. RAMS also utilizes bin-emulating procedures for cloud droplet nucleation, riming, and sedimentation. The microphysics code tracks detailed microphysical budgets, which is crucial for microphysical process studies. Further details on various aspects of the RAMS microphysics scheme may be found in Walko et al. (1995), Meyers et al. (1997), Saleeby and Cotton (2004, 2008), and Saleeby and van den Heever (2013).

The model domain was initialized with vertically varying but horizontally homogeneous conditions. The control (CTL) experiment thermodynamic profile follows the analytical profile of Weisman and Klemp (1982) with a vapor mixing ratio of 13 g kg^{-1} in the well-mixed boundary layer. The initial CTL temperature and dewpoint profiles are shown in blue in Fig. 3.1. Surface-based convective available potential energy (CAPE) in this environment approaches 1800 J kg^{-1}.

An idealized half-circle shear profile was used in which wind speeds increased from 0 m s^{-1} at the surface to 32 m s^{-1} at 5 km AGL. Wind speeds increased slowly to 34 m s^{-1} by 7 km AGL, with no further vertical wind shear above 7 km. The wind profile in knots is also depicted in Fig. 3.1. The idealized half-circle hodograph shape has been used extensively in modeling studies of supercells (e.g. Weisman and Klemp 1984; Droegemeier et al. 1993; McCaul and Cohen 2002), and the hodograph strength utilized in the present study corresponds to the strongest shear case tested in Weisman and Klemp (1984). This shear and instability combination is conducive for supercell development, and the clockwise-turning hodograph favors the right-moving storms (Weisman and Klemp 1984). The magnitude of the shear is representative of

previously observed LP supercell environments (e.g. BD79, their Fig. 2; Bluestein and Woodall 1990, their Fig. 7; MacGorman and Burgess 1994, their Table 1 for the 26 March 1991 case).

To address the goals of this study, nine additional sensitivity simulations were next designed with varying environmental moisture profiles. Moisture mass was systematically reduced from the CTL vapor mixing ratio profile within a 1 km deep layer; these layers will simply be referred to as dry layers. The various imposed dry layers were located at three different heights: 1.5-2.5 km, 2-3 km, and 3-4 km. Such dry layers often occur above the well-mixed boundary layer near the dry line or in the high plains due to the elevated mixed layer, such as shown in Ziegler and Rasmussen (1998, their Fig. 3), Cai et al. (2006, their Fig. 18), and Parker (2012, his Fig. 1). The vapor mixing ratio was linearly interpolated to the original profile at 1 km below and 2 km above the dry layer, and the final profile was then smoothed. The addition of various dry layers, one for each experiment, are also depicted in Fig. 3.1. Throughout the rest of the chapter, these experiments will be referenced using a letter and number, where the first letter is either L, M, or H, referring to the height of the dry layer (L-low, M-middle, H-high); and the number is either 25, 50, or 75, referring to the vapor mixing ratio reduction percentage. For example, H75 refers to the experiment with the strongest (75%) reduction in mixing ratio within the highest vertical layer. The experiment names and dry layer setups are summarized in Table 3.2. The precipitable water (PW) for each simulation, which varies from ~30 to 45 mm, and the percent change from CTL are listed in Table 3.3.

In the interest of performing a controlled experiment, the moisture profile was kept identical in each simulation except within the imposed dry layer. In this way, the surface-based and most unstable CAPE, rather than the mixed-layer CAPE, are kept constant for each case, save for small variations (<5%) due to the virtual temperature effect. Note that the lowest and

middle dry layers deplete moisture from the well-mixed layer. This reduces the mixed-layer CAPE by ~10 and 20% in L25 and L50, respectively, but it does not change the mixed-layer CAPE by more than a few percent in M25-75. Consequently, M was the lowest dry layer that supported sustained convection. Simulation L75 was therefore not performed, and simulations L25 and L50 will only be briefly discussed in section 3.3a below.

While the observed example dryline and high plains soundings referenced earlier contain dry air confined within a layer, it is perhaps more common for dry air aloft to extend upward throughout the troposphere. Furthermore, as stated in Weisman and Klemp (1982), the analytical sounding is too moist within upper levels compared to soundings representative of midlatitude severe weather situations. Two sensitivity experiments were therefore performed in which the vapor mixing ratio was reduced by 50% above 6 km for experiments CTL and H50 (not shown). Very little change in the simulation evolutions, accumulated precipitation, and storm structure were found. Therefore, the results presented in this study do not appear to depend on the presence of the overlying moist layer above the imposed dry layer.

Finally, based on the results from the dry layer sensitivity experiments presented in the next section (3.3), aerosol concentrations were enhanced for simulations CTL, M25, and H50. The cleanest aerosol profile utilized in all nine dry layer experiments described above contained a surface number concentration of 100 cm^{-3} that decreased linearly to 10 cm^{-3} at 4 km and was held constant thereafter. Note that this aerosol profile applies to a small mode of both ammonium sulfate and dust, and therefore the total aerosol number concentration is actually double. For the aerosol sensitivity tests, aerosol concentrations were multiplied everywhere by a factor of 4 and 16 so that the surface concentration was 400 cm^{-3} in the moderately polluted tests and 1600 cm^{-3} in the most polluted tests. The three aerosol concentration profiles are shown in Fig. 3.2. The

simulations with enhanced aerosol concentrations are named by appending the surface number concentration to the dry layer name (e.g. M25-400 or H50-1600). The results from the aerosol sensitivity tests are presented in section 3.4.

3.3 Results: Dry Layers

a. Simulation evolution and precipitation characteristics

This section (3.3) discusses the results of the dry layer sensitivity experiments. General characteristics of each simulation evolution are evident in the accumulated surface precipitation field (Fig. 3.3). Firstly, given the imposed veering wind profile, the initial thermal in CTL evolves into a convective storm that splits into a right-mover (RM) – which becomes the dominant, relatively steady supercell – and a left-mover (LM), which later undergoes additional storm-splitting. In CTL, splitting is first evident in the midlevel updraft after 45 minutes.

The initial storm split and the same general precipitation pattern are evident in experiments CTL, M25, H25, H50, and H75, although it can be seen by comparing these five experiments that the RM in CTL takes a sharper right-turn than in the other experiments. This is broadly consistent with BD79's observations of tornado-producing LP supercells which did not have significant right-turning motion, unlike previously observed CL supercells at that time. BP83 also found that LPs move less to the right of the mean wind shear than CL supercells, although it was noted that this result was significant at slightly below the 95% confidence level.

It is clear that the highest accumulated surface precipitation both overall and for the RM occurs in CTL compared to all of the dry layer experiments. Accumulated precipitation for the CTL RM reaches a maximum of 26.8 mm at the end of the simulation, whereas it only once exceeds 20 mm in H50 and not at all in the other simulations. Domain-wide accumulated

precipitation is reduced as the dry layer strength is increased, especially in the precipitation resulting from the initial LM. The environments in M75 and all the experiments with the lowest dry layer are not supportive of sustained convection; the initial convection quickly dissipates in these scenarios. The simulation evolution in M50 is also substantially different. In M50, the initial RM takes much longer to become organized, and its path is therefore displaced farther north. Since moisture was depleted from the top of the mixed layer in the M and L experiments, these results are consistent with those in BP83. They found that the moist layer depth did not differ between CL and LP environments. Additionally, McCaul and Cohen (2002) showed that simulated supercells were more intense under more CAPE-starved environments when the mixed-layer and moist-layer depths were increased.

The weakest dry layer has much more of an impact on accumulated surface precipitation when placed at mid levels (M25) compared with higher levels (H25), though the spatial pattern is similar between the two. In fact, total precipitation in H25 is the most similar to CTL. Furthermore, accumulated precipitation is higher in simulation H50 than in M25, although the reduction in PW is slightly greater for H50 (Table 3.3). Thus simulated storm precipitation characteristics and, as will be shown, RM updraft steadiness and strength (Fig. 3.4b) are significantly more sensitive to the imposed dry layer when it depletes moisture from the well-mixed boundary layer (M and L experiments) than when it does not (H experiments), again in agreement with McCaul and Cohen (2002) and BP83.

Since one objective of this study is to compare the microphysical and dynamical processes within CL and LP supercells, the analysis will focus on the RM storm for the rest of section 3.3. Further discussion of the left-moving cluster is provided in section 3.4. Only six experiments produced a RM supercell. The total precipitation rate over the RM track, shown in

Fig. 3.4a, is calculated as the rate of change of accumulated surface precipitation in kg s^{-1} by the formula $\Delta\left[\left(\sum_{dA} accumulated\_precip > 1mm\right) \bullet dx \bullet dy\right] / \Delta t$. This takes into account the intensity of the RM precipitation, as well as its spatial extent. Experiment CTL produces the most precipitation .The total RM surface precipitation is systematically reduced as the dry layer strength increases and as the dry layer altitude decreases, in agreement with the results shown in Fig. 3.3. There is some indication that a limit exists on the extent to which the dry layer can impact the precipitation for the high-level dry layers; for example, the reduction in the RM precipitation rate between CTL and H25 is larger than the reduction between H25 and H50, and the change in precipitation rate between H50 and H75 is relatively small.

The reduced RM surface precipitation rate in the various dry layer experiments does not occur because the dry layer reduces the storm's updraft strength, except perhaps in M50 and at times in M25 (Fig. 3.4b). The CTL and all the highest dry layer experiments exhibit similar maximum updraft speeds of ~50 m s^{-1} once they reach a relatively steady state, particularly after ~90 simulation minutes. The RM supercells in M25 and M50 are more unsteady in comparison. Maximum updraft strength varies by 10-15 m s^{-1} in M25, although it does occasionally exceed 50 m s^{-1}. The M50 RM is a weaker storm overall; its maximum updraft strength exceeds 40 m s^{-1} for only ~30 minutes.

Though updraft strength is comparable amongst the supercells, especially between CTL and H25-75, the dry layer RM supercells have narrower updrafts (Fig. 3.4c). The area of updraft exceeding 15 m s^{-1} at 6 km in CTL is about twice as large as the updraft area in M25, H50, and H75. This is consistent with observations of LP supercells resembling "skeletons" of CL supercells with narrower updrafts (BP83).

The analysis in this and the following section will focus on the CTL, M25, H50, and H75 RM supercells. These four are chosen because M25, H50, and H75 have similar updraft and precipitation characteristics and resemble LP supercells, as is seen in Fig. 3.4 and will be discussed in further detail in the following sections. M50 is excluded because it is a weaker storm. H25 cannot easily be defined as an LP supercell, as it has an updraft area and precipitation characteristics between that of the CTL RM and the other dry layer RMs (Fig. 3.4a and c).

Temporal evolution of surface precipitation rate, and maximum up- and down-drafts within the lowest 1 km, for the last 20 simulation minutes are depicted in Fig. 3.5 for the above-mentioned four RM supercells. The CTL RM exhibits characteristics of CL supercell storms. The FFD region contains heavy precipitation. In the RFD region to the west of the main low-level updraft, precipitation rates typically reach 60-75 mm hr^{-1} throughout the last 30 simulation minutes and even exceed 100 mm hr^{-1} at 150 min (not shown). The precipitation field clearly resembles the typical hook echo structure of CL supercells.

Though the RMs in dry layer experiments M25, H50, and H75 also exhibit these general RFD and FFD precipitation features, the RFD precipitation is less intense, particularly in H50 and H75 (Fig. 3.5, around x=-5 to x=-2 and y=0 in each panel). Specifically, RFD precipitation rates are typically ~30-60 mm hr^{-1} in M25, 15-30 mm hr^{-1} in H50, and 15-45 mm hr^{-1} in H75 compared to 60-75 mm hr^{-1} in CTL. The RFD also covers a smaller area. It is separated from the region of FFD precipitation by lighter precipitation rates in comparison to CTL, where the FFD and RFD precipitation are more continuously connected.

The spatial distribution of the FFD precipitation is notably different in the dry layer supercells compared to CTL. H50 and H75 have an elongated region of light precipitation extending downwind (with respect to the upper-level winds) of the heaviest FFD precipitation,

and the north-south extent of this precipitation is reduced, particularly in H75, when compared to CTL. The FFD precipitation in M25 is not as elongated as in H50 and H75; rather, the M25 supercell looks more like a spatially smaller and less intense version of CTL with a less-well-defined RFD.

To summarize, when elevated or weak dry layers are present in the moisture profile (M25, H50, and H75), strong RM storms form that have characteristics of LP supercells. These features include narrower updrafts, reduced surface precipitation rates, and a different RFD and FFD precipitation spatial pattern than in a CL supercell. In the next section, storm structure and dynamic characteristics of the CTL, M25, H50, and H75 supercells are compared and related to the differences noted in the precipitation features. The rest of the analysis will focus on the last 20 simulation minutes when the updraft strengths are similar amongst the four supercells (Fig. 3.4b).

b. Storm structure and dynamical features

The broad dynamical structure of the CTL, M25, H50, and H75 RM supercells is demonstrated in Fig. 3.6. Since the imposed environmental wind profile is strongly veering, each RM supercell ingests streamwise vorticity into its updraft due to its deviant rightward motion off the hodograph. The resultant mesocyclone structure is fairly similar amongst the supercells. A deep column of rotation exists within each updraft, and vertical relative vorticity exceeding 0.01 s^{-1} extends from at least 3 km up through 10 km, meeting the commonly accepted definition of a supercell storm (e.g. Doswell and Burgess 1993).

At the time shown in Fig. 3.6 (180 min), moderate updraft speeds (10 and 25 m s^{-1} contours) extend higher into the storm in the CTL and H75 supercells than in the other two.

However, the updraft heights vary considerably with time for each storm due to fluctuations in updraft strength resulting from low-level convergence and hydrometeor loading. The updraft is narrower in the dry layer supercells, as first shown in Fig. 3.4c, which is a consistent feature throughout the analysis time.

The broad updraft region is circular in the CTL supercell (Fig. 3.7), while updraft speeds greater than 25 m s^{-1} take on a typical horseshoe shape (e.g. Lemon and Doswell 1979; Byko et al. 2009). The dry layer supercell updraft shapes look similar to CTL, but they are more elongated along the northwest-southeast direction. In CTL, a region of updraft speeds between 10 and 25 m s^{-1} exists in the west-northwest portion of the updraft. Enclosed in this region is a spatially small and strong positive and negative couplet of vorticity, with the negative vorticity located ~3 km to the east of point A in Fig. 3.7 and the positive vorticity usually to its north. The negative vorticity is the stronger and more persistent of the couplet pair (e.g. H50 and H75 in Fig. 3.7). Similar midlevel vorticity couplets have been reported in previous observational (e.g. Bluestein and Gaddy 2001; Markowski 2008) and modeling (Byko et al. 2009) studies. These couplets also exist in the dry layer supercells, although they are spatially smaller. Additionally, in the dry layer supercells, the regions of weaker (10-25 m s^{-1}) updraft speeds are only contained within a narrow strip following the horseshoe shape and do not fully encompass the positive and negative vorticity couplets. These midlevel vorticity features will be discussed in relation to the microphysical processes in section 3.3d.

Cross sections of relative humidity, total condensate mixing ratio, and storm-relative winds shown in Figs. 3.8 and 3.9 demonstrate the direct impact of the imposed dry layer on the simulated supercells. Firstly, the dry layer impinges on the updraft between 2 and 5 km from the west (Fig. 3.8). The lower relative humidities in the elevated dry layer will evaporate any

existing cloud droplets on the western flank of the main updraft in the LP-like supercells, eroding the cloud edge until the flow reaches the edge of the main updraft and is diverted around it. Secondly, evaporation is enhanced within the forward flank regions to the east and north of the main updrafts as precipitating hydrometeors fall through the dry layer. Consequently, precipitation rates are less in the FFD of the LPs (Fig. 3.5). Thirdly, the dry layer altitude sits within the deep layer southerly inflow feeding each supercell (Fig. 3.9). The drier air ingested into the updraft reduces the amount of vapor available for hydrometeor growth. Vapor microphysical budget terms indicate that vapor deposition is reduced in M25 and H50 relative to CTL (not shown), at times up to ~25% at 3 and 4 km. This impacts the mass of condensate within the lower levels of the updraft.

Finally, because the updrafts are narrower in the three dry layer supercells than in CTL, they are tilted more to the east (Fig. 3.8) in agreement with theory (Davies-Jones 2002). The tilt orientation favors hydrometeor lofting into the downshear portion of the anvil over the upshear portion. As evident in both Figs. 3.8 and 3.9, the upshear anvil is very thin or almost entirely absent in each LP supercell, and hydrometeor mixing ratios do not extend beyond the western edge of the updraft between ~4 and 10 km in M25, H50, and H75. Implications of these changes in the upshear anvil and western cloud edge for the hailstone embryo region in the classic Browning and Foote (1976) hailstone growth model, and the resulting impacts on LP supercell hail and precipitation production efficiency, are discussed in the next two sections.

c. Microphysical fields and budgets

This section discusses microphysical characteristics and budgets in the CTL, M25, and H50 simulations. The M25 and H50 LPs were chosen for the following analysis because of their

similarity in total precipitation rate, updraft strength, and updraft area (Fig. 3.4). The magnitude of the change in PW is also most similar for these two cases. H75 is excluded because its precipitation distribution is similar to H50 (Fig. 3.5). All figures within this section are presented as composites over simulation minutes 160-180 relative to the midlevel updraft center. RAMS model output for these three simulations was produced every minute for this time period; thus 21 times are used for each composite. The following analysis focuses on microphysical trends within two regions of the supercell updrafts: (1) the horseshoe portion, to the west-northwest of the highest updraft speeds (simply referred to as the horseshoe from here on); and (2) the northeast edge of the updraft. These two regions are labeled "A" and "B", respectively, in Figs. 3.7 and 3.10-3.12.

The highest midlevel rain mixing ratios occur within the horseshoe (east of point A) for each of the three supercells (Fig. 3.10a-c). Rain mixing ratios frequently exceed 10 g kg^{-1} in the horseshoe, although the composite magnitude for CTL (Fig. 3.10a) is lower than this because the horseshoe of the updraft is more variable in shape for CTL than for the LPs. The largest mean rain diameters exceed 1 mm on average and are also located in the horseshoe for each supercell (Fig. 3.10d-f). The region of largest raindrops extends farther north of the updraft in M25 and H50 than in CTL.

In CTL, rain mixing ratios are negligible to the south, east, and northeast of the strongest updraft core. Conversely, the northeast edge of the updraft near point B is characterized by a secondary strip of local maxima in rain mixing ratios and mean raindrop diameters in M25 and H50 (Fig. 3.10b,c,e,f). Rain mixing ratios reach 4 g kg^{-1} at times near point B for the LPs, and raindrops have diameters around 0.4-0.6 mm on average. Note also that rain number

concentrations are higher there than in CTL. The differences in the rain fields near point B between CTL and the LPs are persistent in time and occur through a depth of several km.

Two local maxima in hail mixing ratios are present in CTL: one in the horseshoe within the 10-25 m s^{-1} updraft envelope (Fig. 3.11a east of point A), and another to the northwest outside of the main updraft (~x=-8, y=10). In the horseshoe, the composite hail mixing ratio exceeds 9 g kg^{-1} in CTL, but is only ~2 g kg^{-1} in H50 and is nearly negligible in M25 (Fig. 3.11b-c). It is not until 8-9 km that the hail mixing ratio within the western portion of the updraft is comparable between CTL and the dry layer cases (not shown). The local hail maximum that occurs to the northwest of the updraft in the CTL supercell is displaced farther east in M25 and H50. Additionally, immediately to the northeast of the updraft at point B, hail mixing ratios are up to a factor of 2 higher in the LPs compared to CTL.

Typically, the largest hail associated with CL supercells falls to the north of the updraft, whereas observations of LPs usually report hail falling from the downshear anvil, i.e. northeast of the updraft (e.g. Davies-Jones et al. 1976; BP83). As noted above, the hail mixing ratio maxima outside of the updraft occurs to the northwest in the CL and to the north in the LPs. If the simulations included stronger westerly shear aloft, as is typically observed in severe weather situations, these hail locations would shift from northwest to north of the updraft in CTL and from north to northeast for the LPs, in agreement with observations.

In the CTL supercell, the largest mean hail diameters are collocated with the highest hail mixing ratios and large raindrops within the horseshoe (Figs. 3.10a and 3.11a,d). In M25 and H50, hail diameters are significantly smaller than in CTL throughout the stronger portion of the updraft. These smaller hailstones are more easily lofted into the storm's anvil within the strongest updraft core and are subsequently transported further downwind of the updraft than in

CTL, thereby reducing their likelihood of reaching the surface as precipitation and decreasing the precipitation efficiency of the LPs relative to CL supercells. The hail diameter differences across the updraft are also consistent with those in van den Heever and Cotton (2004), where simulations using single-moment microphysics were performed and the mean hail diameter was systematically varied. Supercell precipitation characteristics were found to move from the HP end of the spectrum toward the CL supercell structure as the mean hail diameter was decreased (their Fig. 15).

It is perhaps counterintuitive that mean hail diameters are smaller across the updraft in these simulations because observations of LPs usually report large hailstones falling from the downshear anvil. However, this may be a subjective statement in that the adjective "large" is relative to the typically reported lack of rain occurring with these storms, as pointed out in Beatty et al. (2008). Additionally, observations of mean hail diameters within an LP and CL supercell occurring in a similar environment do not exist to the authors' knowledge, and a climatology of typical hail sizes associated with LPs and CLs is not available due to the relative scarcity of LP observations.

Differences in hail number concentration arise between the CTL and dry layer supercells near both points A and B (Fig. 3.11g-i). In CTL, a region of small hailstones with number concentrations between 500 and 1000 kg^{-1} occurs just east of point A outside the 10 m s^{-1} updraft contour for all the individual times within the analysis, although it only faintly appears in the composite because the CTL horseshoe shape changes in time as previously mentioned. The corresponding hail mixing ratios in this region are 2-3 g kg^{-1}. The location of this region corresponds to the location of the embryo curtain in the Browning and Foote (1976) model for hailstone growth – a source region for hailstone embryos on a supercell's right flank – and is

absent in M25 and H50 at this altitude (see also Figs. 3.8-3.9). There are also differences in hail number concentrations near point B; hail concentrations are enhanced in the dry layer supercells immediately outside of the updraft to the east-northeast.

Microphysical process budgets afford a closer look at the differences between the rain and hail fields in CTL, M25, and H50. Within the horseshoe, to the east of point A, riming rates are substantially larger in CTL than in the dry layer supercells, especially at 6 km (Fig. 3.12a-f). The riming rates with the horseshoe for CTL are larger in magnitude by several g kg^{-1} min^{-1} at individual times than is indicated in the composite. In the dry layer supercells, riming rates are enhanced at point B along the northeast side of the updraft relative to CTL, especially at 7 km (Fig. 3.12a-f). Collision and coalescence processes are also more efficient there (Fig. 3.12h,i), whereas cloud to rain conversion rates are negligible along the entire southern, eastern, and northeastern edges of the CTL supercell updraft (Fig. 3.12g). The more efficient rain production south of point B in M25 and H50 is collocated with the locally higher rain mixing ratios and larger raindrops. The implications of these different process rates for hail growth is discussed next.

d. Hail growth mechanisms

In this section, hailstone growth processes are discussed in relation to the aforementioned differences in the microphysical fields and budgets, first in the context of the Browning and Foote (1976) hailstone growth model. In this model, small frozen hydrometeors, or hailstone embryos, fall from the back-sheared anvil (referred to as the embryo curtain) and become re-ingested in the updraft, where they accrete liquid water during their final ascent through the

updraft. The largest hailstones grow in a favored region of moderate updraft strength, where the hailstone fall velocity approximately balances the updraft speed.

In the CTL classic-type supercell, high riming rates, high rain and hail mixing ratios, and large rain and hail diameters are all collocated within the horseshoe where updraft speeds are moderate (~10-25 m s^{-1}). Hailstone fall speeds in RAMS are given by the power law formula $v_t = 152.1 \cdot D^{0.497}$, where v_t is the terminal velocity in m s^{-1} and D is the mean hail diameter in m, following Mitchell (1996). The highest mean hail diameters contributing to the composite in Fig. 3.11 frequently exceed 9 mm, for which the corresponding hailstone fall speed is ~15 m s^{-1}. These fall speeds are relatively well balanced by the updraft, permitting longer hailstone residence times. Furthermore, these signals are collocated with the anticyclonic and cyclonic vorticity couplet (Fig. 3.7). Storm-relative wind speeds are weak, and the flow orientation associated with the vorticity couplet keeps growing hailstones from advecting horizontally around the mesocyclone, further extending hailstone residence times in this region. The superposition of high hydrometeor mixing ratios and the vorticity couplets resembles the mechanism for type I descending reflectivity core (DRC) formation within a “stagnation zone” (Rasmussen et al. 2006; Byko et al. 2009). All of these signals together indicate that in the CTL supercell, efficient large hailstone growth mechanisms are at work within the horseshoe. Hailstone embryos originate within the embryo curtain resulting from the backsheared anvil, as suggested in the Browning and Foote (1976) model. Hail that grows large enough in the horseshoe may begin falling relative to the updraft, advecting either cyclonically around the southwest side of the updraft and contributing to the RFD precipitation (e.g. Knight and Knupp 1986), or anticyclonically to the north side of the updraft, contributing to the precipitation within

the main hailstone fallout region in the CL supercell structure (Browning 1964; Lemon and Doswell 1979; Browning and Foote 1976).

Although the vorticity couplets and local rain mixing ratio maxima are also present in the horseshoe for M25 and H50, the relative lack of high hail mixing ratios and large hail diameters combined with the small backsheared anvil, absence of the right flank hailstone embryo region, and reduced area of moderate updraft speeds near the horseshoe indicate that the classic Browning and Foote (1976) hailstone growth model is much less efficient in LP supercells. As described in the previous section, the northeast side of the updraft in M25 and H50 contains higher rain and hail mixing ratios, larger raindrops, and enhanced riming relative to CTL. Interestingly, the enhanced riming in the LPs is collocated with a strip of negative relative vorticity (Fig. 3.7, point B). Storm-relative flow associated with this vorticity keeps hydrometeors, whether raindrops or hailstones, along the edge of the updraft as they are advected cyclonically around the eastern side of the mesocyclone. Therefore, it appears that another hail growth pathway exists along the northeastern edge of the updraft that is more efficient in LP supercells. This mechanism is hypothesized to work in the following way:

More and larger raindrops are available along the northeast side of the updraft in the LP supercells (Fig. 3.10b,c,e,f), due in part to (a) advection cyclonically around the mesocyclone from the horseshoe, given the lack of hail to collect rain by riming in this region (Fig. 3.11); and (b) enhanced collision and coalescence processes (Fig. 3.12h,i) due to the larger raindrops present and thus higher collection efficiencies. Greater hail mixing ratios and higher number concentrations of smaller hailstones are also located just outside of the northeast updraft edge (Fig. 3.11) due to the weaker storm-relative winds to the north and east of the main updraft at mid- and upper-levels (e.g. Figs. 3.8 and 3.9). Hail embryos that aren’t transported within the

strongest core of the updraft and out into the anvil region downwind, but instead fall out on the north and east periphery of the updraft at upper-levels, will fall closer to the midlevel updraft where they may be re-circulated into the updraft edge by the storm-relative flow. Note that the composite storm-relative wind vectors around point B, outside of the main updraft, have a northerly or easterly component in M25 and H50, whereas they do not in CTL (Figs. 3.10-3.12). The subsequent combination of larger raindrops and more numerous small hailstones enhances the riming process, thereby producing more efficient hailstone growth along the northeast updraft edge in the LPs before the hailstones fall out in the FFD region.

Previous studies of hail growth processes support the mechanisms in this proposed LP supercell hailstone growth model. Nelson (1983) indicates that hailstones can grow to sufficient size in a single traverse through the updraft, and that hail growth tends to occur at a nearly constant altitude. Temperatures within the updraft at ~6 and 7 km in M25 and H50, where the strongest riming signature is seen along the northeast updraft edge, fall within the -10 to -25 °C temperature zone that is efficient for hailstone growth (Foote 1984) (Fig. 3.13). Lastly, Rasmussen and Heymsfield (1987) describe a supercell case in which hailstone growth likely occurred across the updraft core or along the updraft edges; hailstone embryos were thought to originate from the updraft fringes.

In summary, due to the differences in the updraft tilt and shape and the dry layer impacts on the cloud edge, a spatial reorientation of the hydrometeors (Fig. 3.13) favors a different dominant midlevel hail growth mechanism in LPs compared to CL supercells. As evidenced in both the plan view and the cross section in Fig. 3.13, the most significant overlap regions between the hail and rain mixing ratios within the prime temperature growth zone shift from the western and southwestern side of the updraft in the CL supercell to the northeastern side in the

LP supercells. Therefore, as described above, hailstone growth is favored along the eastern and northeastern edge of the mesocyclone in the LPs. The heaviest precipitation is also favored to the north and east of the updraft within the FFD region, while the RFD precipitation rates are much lighter. The shift in hydrometeor mixing ratio distributions and relative importance of the different hailstone growth mechanisms within CL and LP supercells can therefore explain their variations in precipitation distributions (Fig. 3.5). The two hail growth mechanisms and their associated hailstone embryo source regions, areas of highest riming rates, and resulting surface precipitation distributions are summarized in the schematic presented in Fig. 3.14.

3.4 Results: Aerosols

This section presents the results of the aerosol sensitivity experiments that were performed for simulations CTL, M25, and H50. Aerosol concentrations were enhanced by a factor of 4 and 16 (Fig. 3.2) for these three moisture profiles based on the analysis of the microphysical fields and budgets described above. In order to separately analyze the RM and LM convection and their relative sensitivity to aerosols and midlevel dryness, the domain was subjectively divided such that the southern portion contained all of the accumulated precipitation exceeding 1 mm for the RM and the northern portion contained the rest. The results to be presented in this section are insensitive to 10 km shifts of this subjective division to the north and south, since the analysis focuses on the latter half of the simulation when the RM and LM cluster are widely separated (e.g. Fig. 3.3). Fig. 3.15 shows the response of the accumulated precipitation for the entire domain, the RM, and the LM cluster to changing aerosol concentrations for all three moisture profiles. It is clear that the presence of the dry layer has a much stronger influence on the accumulated precipitation than the aerosol concentrations. The

largest reduction in domain-accumulated precipitation relative to CTL is ~70% for M25, whereas the largest change due to aerosols occurs between H50 and H50-1600 and is only ~15%.

Separating the accumulated precipitation into the contributions from the right- and left-movers reveals additional interesting trends. The accumulated precipitation from the RM supercell is reduced for all three moisture profiles when aerosol concentrations are increased from the moderately polluted to the most polluted conditions. Previous studies of aerosol influences on supercells have also found decreasing trends in precipitation, although in a few instances the supercell precipitation increased for different environments (e.g. relative humidity) or microphysical schemes (Seifert and Beheng 2006; Khain and Lynn 2009; Storer et al. 2010; Morrison 2012). In the LP supercells, the RM precipitation is reduced by ~15-20% in the 1600 cases compared to the clean cases. However, a substantially different pattern emerges for the LM precipitation. While enhanced aerosol concentrations make very little difference in the LM precipitation for CTL, the precipitation decreases in H50 but increases in M25 by a factor of ~2 between the two extremes. This result demonstrates several important points: (1) the mechanism by which aerosols influence total precipitation is different for supercells and multicells; (2) the magnitude, and even the sign, of aerosol impacts on multicellular precipitation are sensitive to the vertical distribution of moisture. The sensitivities of the RM supercells to aerosols are discussed in the next section, and in the following section the processes responsible for the LM precipitation trends are investigated.

a. The right-mover

The same RM storm characteristics as those shown in Fig. 3.4 for the dry layer sensitivity tests are displayed in Figure 3.16 for the aerosol sensitivity tests, but expressed as a difference

from CTL. All nine supercells have strong updrafts, but the main distinguishing features of the LPs, including the reduced precipitation rates and narrower updrafts, are a result of the presence of midlevel dryness. Aerosols alone do not influence supercell morphology, since all the supercells with the CTL moisture profile have CL characteristics regardless of the aerosol concentration. Fig. 3.16 demonstrates that all the updrafts are invigorated by enhanced aerosols, especially in M25 where the updraft is up to 10 m s^{-1}stronger. Despite the stronger updrafts, the LPs produce less precipitation in the most polluted conditions because the anvils contain more ice content. Therefore, the supercells with the most LP-like characteristics occur in the simulations with both drier midlevels and enhanced aerosol concentrations, in keeping with the environments in which they form and the fact that they do not ingest air that has been moistened or cleansed of aerosol by previous convection.

To further demonstrate the relative influence of midlevel dryness and aerosols on the supercellular structure, composite cross sections of relative humidity and cloud, rain, and hail mixing ratios for the cleanest and most polluted simulation sets are shown in Fig. 3.17. It is obvious that the supercell storm structure is nearly identical between the clean and polluted cases for each different moisture profile. Aerosols do not influence the shift from the southwest in the CLs to the northeast in the LPs of both the hydrometeor mixing ratio distribution and the region of significant overlap between hail and liquid water within the prime temperature zone for hail growth. Therefore, the two hail growth mechanisms in CLs and LPs that were described in section 3.3 are not altered due to the presence of enhanced aerosol concentrations. Subsequently, the distribution of surface precipitation around the updraft is also not affected by aerosols (not shown).

Although the hail mixing ratio distribution within the supercell is nearly identical in the clean and polluted simulations, careful inspection of Fig. 3.17 reveals that the cloud water content increases while the rain water content decreases in the 1600 cases relative to the clean cases. In the most polluted aerosol scenarios tested here, the cloud droplets become small enough that the collision-coalescence efficiency is notably reduced, resulting in more cloud water and less rain water within the central and eastern portion of the main updraft. This in turn results in smaller hailstones throughout the updraft core, since the riming of cloud water is less efficient in comparison to riming of rain water (not shown). These smaller hailstones are more readily lofted into the anvil, accounting for the reduced surface precipitation and enhanced anvil mass. The efficiency of the LP hail growth mechanism along the northeast edge of the updraft (Fig. 3.14) is also reduced by the changes in the cloud and rain water partition. Therefore, the reduction in the RM precipitation in the most polluted LP supercells is a direct result of the smaller collection efficiencies associated with smaller cloud droplets.

b. The left-mover

As noted above, the trends in precipitation with changing aerosol concentrations for the multicellular convection resulting from the initial left mover have a complicated dependence on the vertical moisture distribution. For the moist profile (CTL), the LM precipitation is largely unaffected, whereas it is enhanced in M25 and suppressed in H50 (Fig. 3.15). The time series of LM total precipitation rate shown in Fig. 3.19 corroborates this result, although it can be seen that the LM precipitation rates for the aerosol tests in M25 and H50 do not begin to deviate significantly from the clean simulations until 120-150 min into the simulation.

The multicellular convection is largely driven by the low-level forcing induced by the cold pool, as demonstrated in Fig. 3.18. The dynamical lifting associated with the convergence at the cold pool's leading edge enhances convective development. Subsequent rainfall and evaporatively cooled downdrafts further enhance the cold pool strength and therefore the dynamical lift, demonstrating the potential for feedbacks to the cold pool strength and rainfall in these types of convective systems as has been indicated in recent studies (e.g. van den Heever and Cotton 2007; Lee et al. 2008, 2010; Storer et al. 2010; Lee 2011; Morrison 2012; Seigel et al. 2013). Thus it may be expected that the trends in the cold pool temperatures would match the trends in the rainfall, which is in fact evident in Fig. 3.18. For example, the cold pools associated with the LM in H50 and M25 are warmer than in CTL, since both H50 and M25 produce less precipitation, consistent with James and Markowski (2010). Moreover, the LM cold pools qualitatively appear colder for the M25 moisture profile and warmer for the H50 moisture profile as aerosol concentrations are increased. This is demonstrated quantitatively in the time series of the minimum density temperature perturbation (Fig. 3.19), which is directly related to buoyancy. With increasing aerosol concentrations, the cold pool buoyancy is more negative in M25 but less negative in H50, in agreement with the precipitation trends.

Note that the changes in cold pool buoyancy with increasing aerosols occur early at ~90 min. Significant changes in the LM precipitation rate do not occur until later, however. In particular, the LM precipitation rate becomes noticeably larger in M25-1600 compared to M25 at 120 min and substantially larger after 150 min. During this same time period, the M25-1600 cold pool buoyancy decreases even further relative to M25, and the area of strong midlevel updrafts also increases by at least a factor of 2 (Fig. 3.19). The time series for M25 therefore demonstrate how the initial changes in the cold pool buoyancy due to aerosols feeds back to the convection

and rainfall, which in turn further enhances the cold pool strength through evaporative cooling. This represents a positive feedback to the rainfall. The opposite effect occurs in H50; initially, aerosol impacts cause the cold pool buoyancy to weaken, which weakens the cold pool's dynamical forcing and reduces the amount of subsequent convection.

The final piece of the puzzle then is why enhanced aerosol concentrations initially increase the cold pool buoyancy when the dry layer is lower but decrease the buoyancy when the dry layer is higher, thus initiating the respective positive feedback loops. Throughout the time series, the area of midlevel convective updrafts is smaller in M25 than in H50 (Fig. 3.19). This demonstrates that entrainment is more detrimental to the developing convection when the dry layer is lower, as discussed by James and Markowski (2010). Additionally, dry layers have more potential to enhance evaporatively-driven downdrafts when they are lower in altitude (Gilmore and Wicker 1998). Furthermore, the smaller cloud droplets within the more polluted cases have more net surface area and therefore evaporate more quickly, which strengthens the downdrafts (e.g. Lee et al. 2008). Therefore, the initially colder cold pool in the more polluted M25 simulations can be attributed to enhanced evaporative cooling within the downdrafts. To verify this, downdrafts with magnitudes exceeding 1 m s^{-1} were averaged for the LM convection. The downdrafts between ~1-5 km were stronger by ~0.5 m s^{-1} in the more polluted M25 simulations compared to the clean cases (not shown). Note that the layer containing stronger downdrafts corresponds to the depth of the dry layer in this case (Table 3.2). This result agrees with the findings in Lee (2011) that enhanced evaporation within the downdrafts due to smaller cloud droplets can lead to increases in the precipitation by secondary convection under certain humidity conditions.

When the dry layer is higher, as in H50, entrainment is less detrimental to the convection, as evidenced by the larger updraft areas in comparison to M25 (Fig. 3.19), Moreover, the higher altitude of the dry layer is less influential in enhancing the downdrafts by evaporation. Consequently, the downdrafts are weaker in the more polluted simulations below ~3 km for the H50 moisture profile. In this case, the changes in the low-level raindrop characteristics become more important in determining the cold pool response to aerosol loading. The average in-cloud raindrop number concentrations are reduced and raindrops are larger in H50 as aerosol concentrations are increased (Fig. 3.20), in agreement with other recent studies (Storer et al. 2010; May et al. 2011; Storer and van den Heever 2013). The fewer, larger raindrops fall faster and have less net surface area, which reduces the latent cooling rate within the cold pool. The differences in the raindrop characteristics can therefore explain the initially less buoyant cold pool in the polluted H50 simulations.

3.5 Discussion

The results from the dry layer sensitivity experiments described in section 3.3 demonstrate that two hail growth mechanisms are evident in each supercell, although their relative importance varies substantially between storm types. While the classic Browning and Foote (1976) model is clearly evident in the CL supercell, a weak riming signal within the horseshoe is also present in the dry layer supercells at 6 km (Fig. 3.12). A hail overhang region also appears on the southwest side of the updraft in M25 and H50 within the prime temperature zone for hail growth, where it overlaps slightly with cloud and rain water (Fig. 3.13). However, the magnitude and vertical extent of this hail overhang is greatly reduced compared to CTL. Additionally, the riming signal on the northeast updraft edge is present in the CTL supercell, but

it is much weaker than in M25 and H50. Therefore, although substantial differences in their microphysical structures are evident, it does not appear that LP and CL supercells are distinct storm types from this point of view, especially given the similarities in their updraft and vorticity structures. In other words, supercell morphology is characterized by a continuous spectrum rather than discrete types (e.g. Doswell et al. 1990; RS98).

Some of the previously hypothesized storm morphology discrimination mechanisms can be addressed with the results from these simulations. Several hypotheses, including those of Brooks et al. (1994) and RS98, suggest that storm morphology depends on the environmental wind shear profile and resulting differences in storm-relative winds. It was shown that differences in storm relative winds are in fact central to the differences in hydrometeor distributions and hail growth mechanisms for CL and LP supercells. However, the changes in the storm-relative winds are not due to differences in the environmental wind profile, as this was kept identical in each simulation. Rather, the storm-relative wind differences are due purely to each storm's own motion and the storm-scale generated flow field. RS98 also speculated that supercell archetype may in fact depend on the storm motion itself.

BP83 hypothesized that storm morphology may depend on the initial bubble size due to differences in low-level moisture structure near the dryline. The results presented in this study suggest that the moisture content above the well-mixed boundary layer is more important for strong LP supercell formation than low-level moisture content and hence do not support this hypothesis, since neither the initial bubble size nor the vapor mixing ratio within the well-mixed layer were varied. Finally, the hypothesis that aerosol concentrations, through their impacts on drop size spectra, can influence supercell type (Weisman and Bluestein 1985; Bluestein and

Woodall 1990) is not supported, since aerosols had a negligible impact on the supercellular structure and surface precipitation distribution.

In these simulations, supercell updrafts were weaker and more unsteady when the dry layer depleted moisture from the well-mixed boundary layer (M and L simulations), consistent with the findings in BP83 and McCaul and Cohen (2002). However, it is not known how the results in this study translate to different CAPE and shear combinations. For instance, Gilmore and Wicker (1998) and McCaul and Cohen (2002) demonstrated supercell susceptibility to outflow dominance for different environmental controls including midlevel dryness, shear, and CAPE. Future research should therefore test the robustness of simulated supercell morphology sensitivity to the presence of dry layers under a suite of different CAPE and shear profiles. Moreover, James and Markowski (2010) showed that the impact of midlevel dryness on deep convection is sensitive to the microphysical scheme utilized. It would therefore also be interesting to investigate LP and CL supercell dynamical and microphysical structure using a triple-moment hail scheme, which would allow the hail size distribution width to vary in addition to mass and number concentration (Loftus 2012).

LP supercells are known for their difficulty to detect with radar (BD79). Given the differences in the hail mixing ratio distribution in the plan views of Fig. 3.13, it is clear that the classic hook echo shape often used to identify supercells would be much less distinct for LPs, especially if the storm is far enough away from the radar that the lowest elevation scan is sampling the midlevels of the storm, since most of the precipitation falls out ahead of the updraft. The slower and weaker motion off the right of the hodograph in these simulated LPs, which has also been noted in observations (BD79; BP83), may be a useful tool for forecasters to identify LP supercells that have ambiguous radar signals, particularly if model forecast soundings contain

elevated dry layers. It is noteworthy that the differences in storm motion are supported by the theory presented in Davies-Jones (2002). For curved hodographs, propagation off the hodograph decreases with decreasing updraft width. Since LPs have narrower updrafts, it may be expected that their deviant rightward storm motions are smaller. More observations are necessary, perhaps even stratified by hodograph curvature, to ascertain whether the trend in storm motion is robust.

The relative changes in PW in relation to storm morphology may also be of interest to forecasters (Table 3.3). In this study, environments in which PW was decreased by 19% or greater from CTL were not supportive of strong supercells (M50, M75, L50). The H25 RM supercell characteristics were between those of a CL and LP; the decrease in PW was only ~6% for this case. The strong LPs formed when PW was reduced by ~10-20% (M25, H50, and H75), although only if the dry layer was sufficiently elevated. BP83 and RS98 also found differences in PW for different supercell types. However, it should be emphasized that absolute PW magnitude should not be used to rank storm type because (1) as demonstrated here, supercell morphology is more sensitive to the vertical distribution of moisture; and (2) PW is sensitive to the low level moisture content, which was not varied in this study. Lastly, some observations have reported supercell morphology transition within the supercell life cycle (Bluestein and Woodall 1990). According to the findings presented here, supercells may evolve away from the LP end of the spectrum if they form along the dryline or high plains and propagate into environments with higher PW due to deeper mixed layers or higher midlevel moisture content. This may occur in the far-dryline environment as surface elevation decreases and the influence of the elevated mixed layer diminishes.

3.6 Summary

The goal of this study has been to investigate the sensitivity of simulated supercell morphology to the vertical distribution of moisture and to background aerosol concentrations. A suite of simulations was performed in which dry layers of varying magnitudes and altitudes were added to an environment characterized by deep moisture content. Aerosol concentrations were then enhanced for three of the moisture profiles in additional sensitivity tests. The moist profile produced a CL supercell in clean and polluted conditions. Though some of the dry layer scenarios were not supportive of sustained convection, strong and steady LP supercells formed when the imposed dry layer was elevated or weak (simulations H25-75 and M25), regardless of the background aerosol concentration.

The dry layers erode the cloud edge west of the updraft in the simulated LP supercells, which have narrower updrafts that are tilted more toward the east compared to the CL supercell. This combination favors a downshear distribution of hydrometeors and severely limits the upshear anvil extent and hail overhang in the LP storm types. Hail diameters are smaller throughout the updraft in the LPs, allowing them to be lofted more easily into the anvil. Additionally, the dry layers enhance evaporation of precipitation. As a result of these differences, lighter precipitation is found throughout most of the FFD region in the LPs. LP supercells therefore represent the lowest precipitation efficiency storm type within the supercell spectrum, as first suggested by BP83. Despite the large changes to the microphysical structure, the main dynamical features, including the strength and structure of the updraft and the vorticity, are similar between the LP and CL supercells.

It was demonstrated through the use of microphysical fields and process budgets that different hail growth mechanisms are important in LPs relative to CL supercells, as summarized

in Fig. 3.14. At midlevels, the primary hail growth region is located along the northeast edge of the updraft in LPs, whereas in CL supercells, efficient hail growth is preferred within the horseshoe of the updraft. The LP hail growth mechanism favors the FFD precipitation region and assists in explaining the resulting differences in surface precipitation distribution between CLs and LPs.

Finally, the relative sensitivity of supercell morphology and neighboring multicellular convection to dry layers and enhanced aerosol concentrations was investigated. Although the most LP-like supercell characteristics occurred in the simulations containing both midlevel dryness and enhanced aerosol concentrations, the supercellular structure and surface precipitation distribution was not significantly altered by the presence of increased aerosol concentrations. The multicellular convection was substantially more sensitive to aerosols than the supercells through feedbacks to the strength of the cold pool and subsequent dynamical forcing. However, for both the supercells and multicells, the changes in the precipitation with increasing midlevel dryness were much larger than the changes due to increasing aerosol concentrations.

The sensitivity of supercell morphology to the presence of elevated dry layers makes sense considering the environment in which LP supercells typically form, namely along the dryline and the high plains, and the fact that LP supercells are usually isolated or the furthest upwind in a line of storms. Supercells that form in these environments are more likely to draw in unmodified, drier, and more polluted low- to mid-level air that has not been pre-conditioned or processed by previous convection. Additionally, although not investigated in this study, LPs may also be the most upwind supercells due to possible “seeding” of downwind storms by anvil precipitation (RS98) into the right-flank embryo curtain.

High-resolution simulations of LPs and CLs occurring under similar environments with similar updraft strengths and using a sophisticated microphysical scheme have not been previously performed to the authors' knowledge. While new observations of LPs – such as those that can be obtained through the use of polarimetric radar – are needed to validate the findings here, the results of this study provide unique new insights into the dynamical and microphysical structure of LP supercells, which has not been possible with the limited observational data available to date.

3.7 Tables and Figures

Table 3.1. RAMS model configuration and options chosen for the supercell dry layer simulations described in the text.

Model Aspect	**Setting**
Grid	Arakawa C grid $\Delta x = \Delta y = 300$ m; 950 x 750 points Δz variable minimum $\Delta z = 25$ m, maximum $\Delta z = 300$ m vertical stretch ratio = 1.1 92 total vertical levels; 17 levels below 1 km AGL model top ~22 km
Time step	1 s
Simulation duration	3 hr
Initialization	Horizontally homogeneous thermodynamic and wind shear profile
Convective initialization	2 K thermal perturbation 10 km x 10 km bubble 3 km depth
Boundary conditions	Radiative lateral boundary (Klemp and Wilhelmson 1978) Rayleigh friction damping over top 6 vertical levels (~20-22 km AGL) No surface fluxes
Microphysics scheme	Two-moment bulk microphysics (Meyers et al. 1997) 8 hydrometeor classes (Saleeby and Cotton 2004)
Aerosol treatment	Two aerosol species: sulfates, dust (Saleeby and van den Heever 2013) Linearly decreasing sulfate and dust concentration profile from 100 cm^{-3} at the surface to 10 cm^{-3} at 4 km AGL; constant thereafter No aerosol sources or sinks DeMott et al. (2010) Ice Nucleation parameterization
Turbulence scheme	Smagorinsky (1963) deformation-K with stability modifications by Lilly (1962) and Hill (1974)
Radiation scheme	None
Coriolis	No

Table 3.2. Sensitivity experiment nomenclature and the imposed dry layer characteristics. Note that L75 was not performed and hence is not listed in the table.

	75% vapor mixing ratio reduction	**50% vapor mixing ratio reduction**	**25% vapor mixing ratio reduction**
Highest dry layer (center 3.5 km AGL)	H75	H50	H25
Middle dry layer (center 2.5 km AGL)	M75	M50	M25
Lowest dry layer (center 2.0 km AGL)	--	L50	L25

Table 3.3. Precipitable water (mm) for each simulation performed, and the percent change in precipitable water from CTL.

Simulation name	**Precipitable water (PW) (mm)**	**% change in PW from CTL**
CTL	44.05	--
L25	38.64	-12.3 %
L50	33.16	-24.7 %
M25	39.70	-9.9 %
M50	35.34	-19.8 %
M75	30.97	-29.7 %
H25	41.46	-5.9 %
H50	38.86	-11.8 %
H75	36.25	-17.7 %

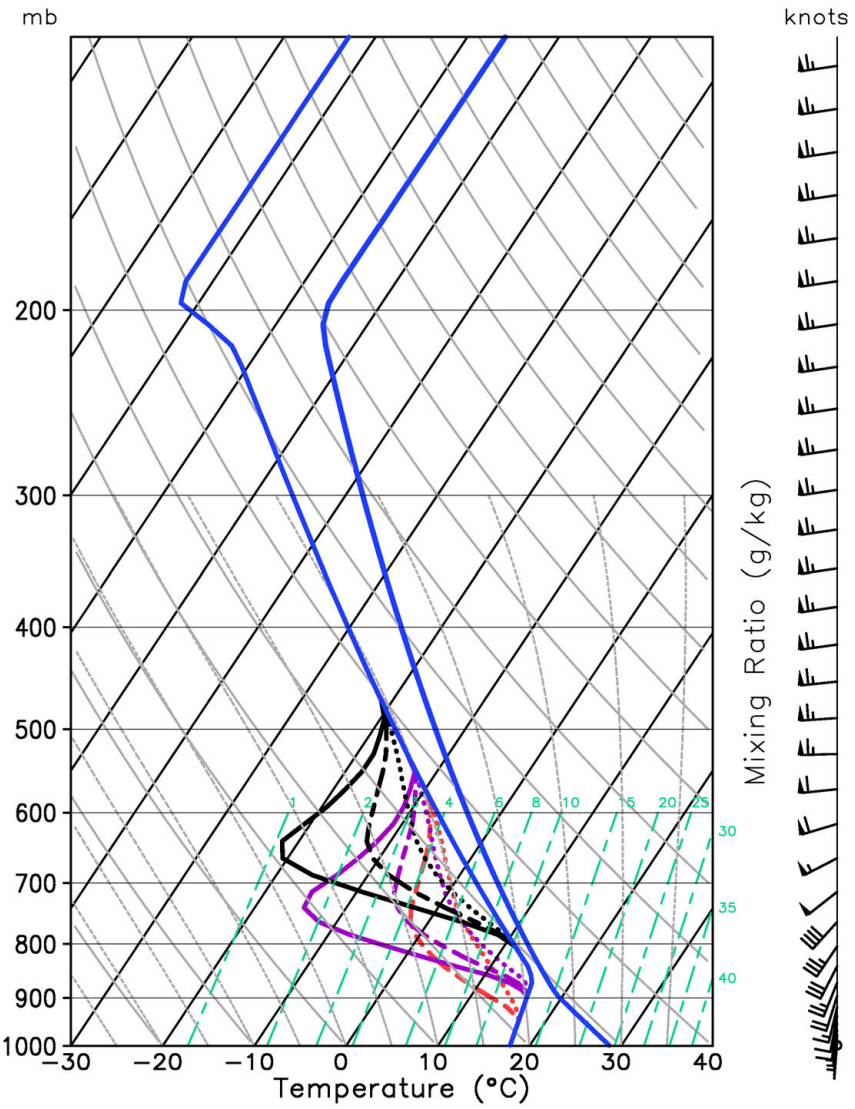

Fig. 3.1. Initial thermodynamic temperature and dewpoint profile used for the control (CTL) experiment (blue lines), following Weisman and Klemp (1982), and the wind profile used for all simulations (barbs, knots). Dewpoint profiles for the various dry layer sensitivity experiments as described in the text are also shown. Black: highest dry layer (H); purple: middle dry layer (M); red: lowest dry layer (L); dotted: 25% moisture reduction; long-short dashed: 50% moisture reduction; solid: 75% moisture reduction.

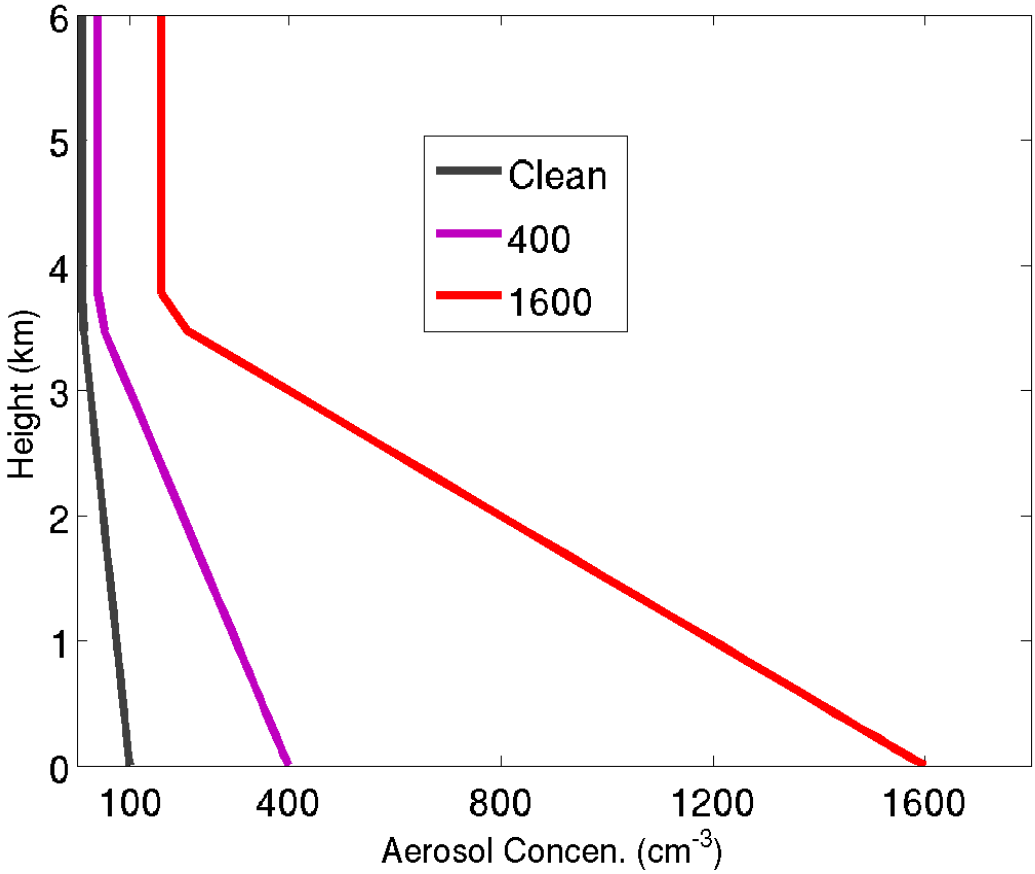

Fig. 3.2. Initial clean aerosol profile for both ammonium sulfate and dust modes that was utilized all nine initial dry layer sensitivity experiments, as well as the two sets of polluted aerosol profiles used for the aerosol sensitivity tests from simulations CTL, M25, and H50. The label in the legend refers to the aerosol number concentration at surface.

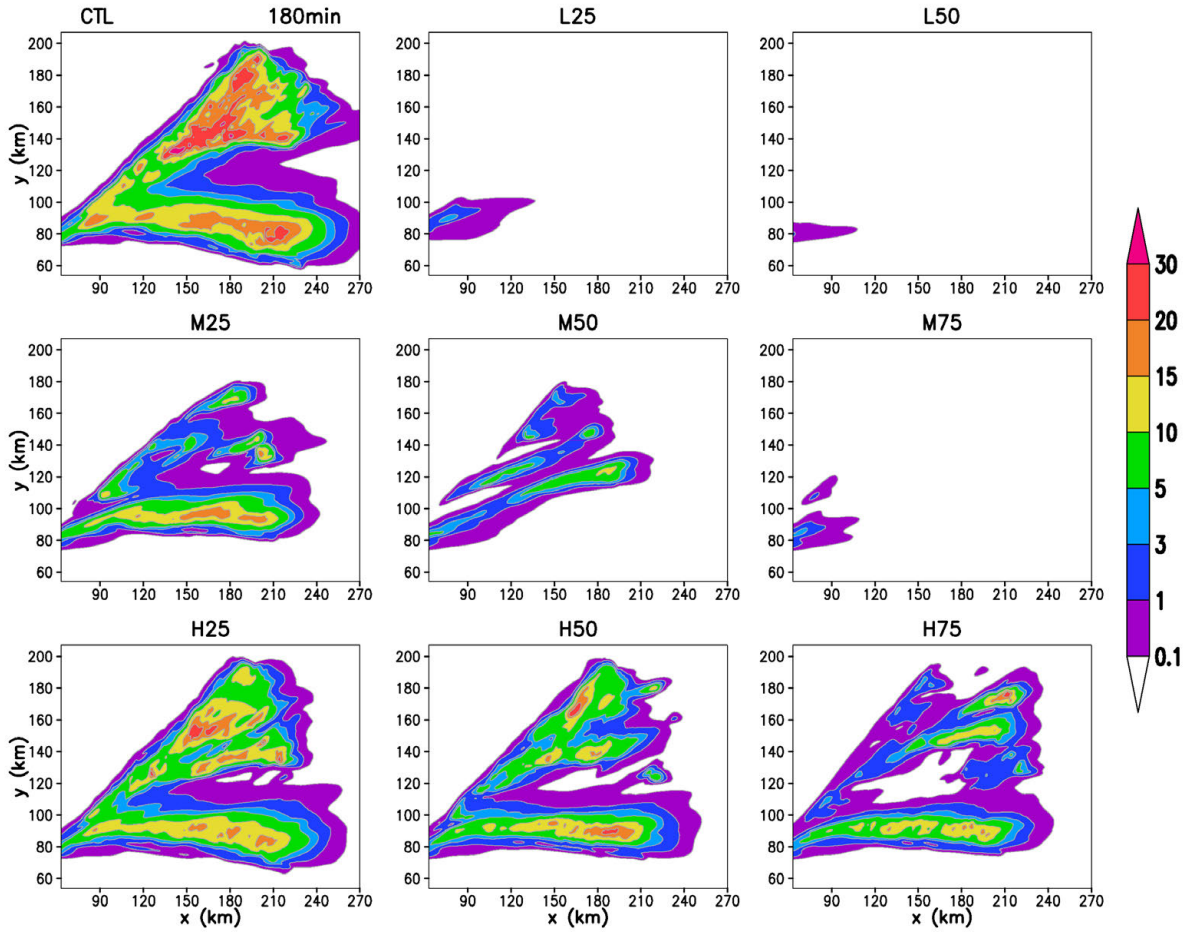

Fig. 3.3. Total accumulated surface precipitation (mm, shaded) after three simulation hours for CTL, L25 and L50, and all M and H sensitivity experiments.

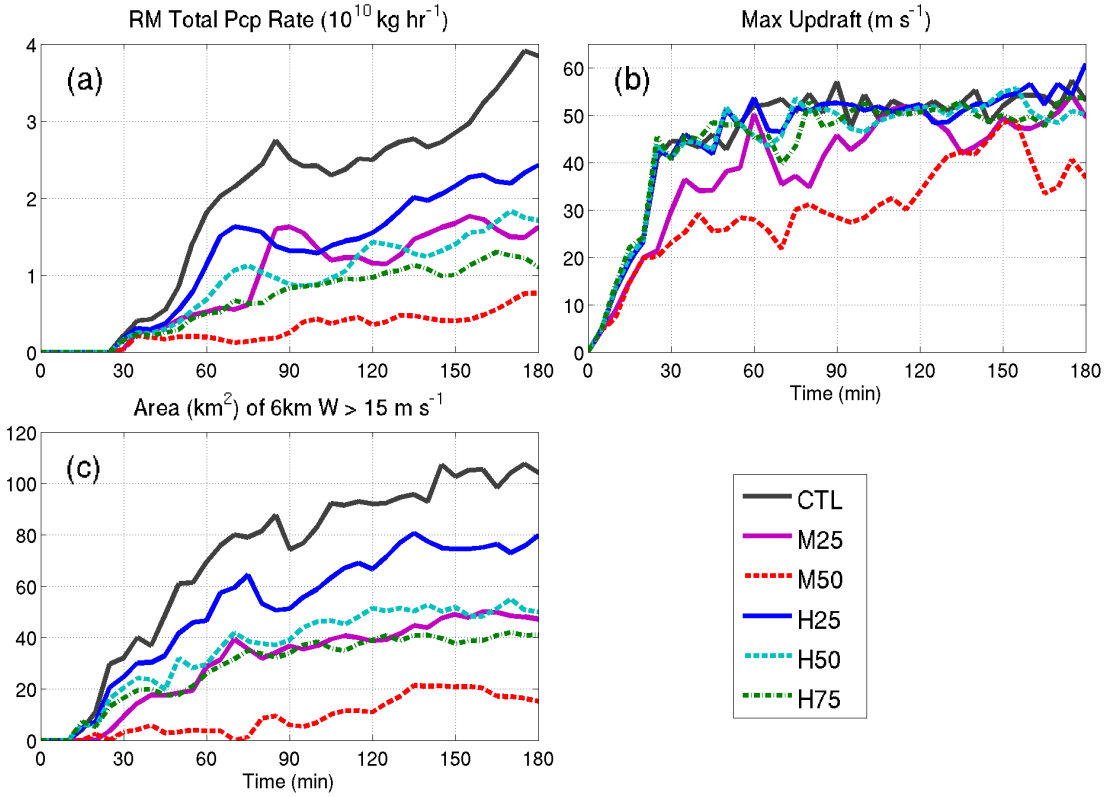

Fig. 3.4. (a) Time series of the total surface precipitation rate (10^{10} kg hr^{-1}) for the RM storm in simulations CTL, M25, M50, and all H sensitivity experiments. Total precipitation rate is calculated from the accumulated surface precipitation field using the formula discussed in the text. (b) Time series of the domain-maximum updraft speed (m s^{-1}) for each RM. (c) Time series of the area of the RM updraft (km^2) where vertical velocity exceeds 15 m s^{-1} at ~6 km AGL.

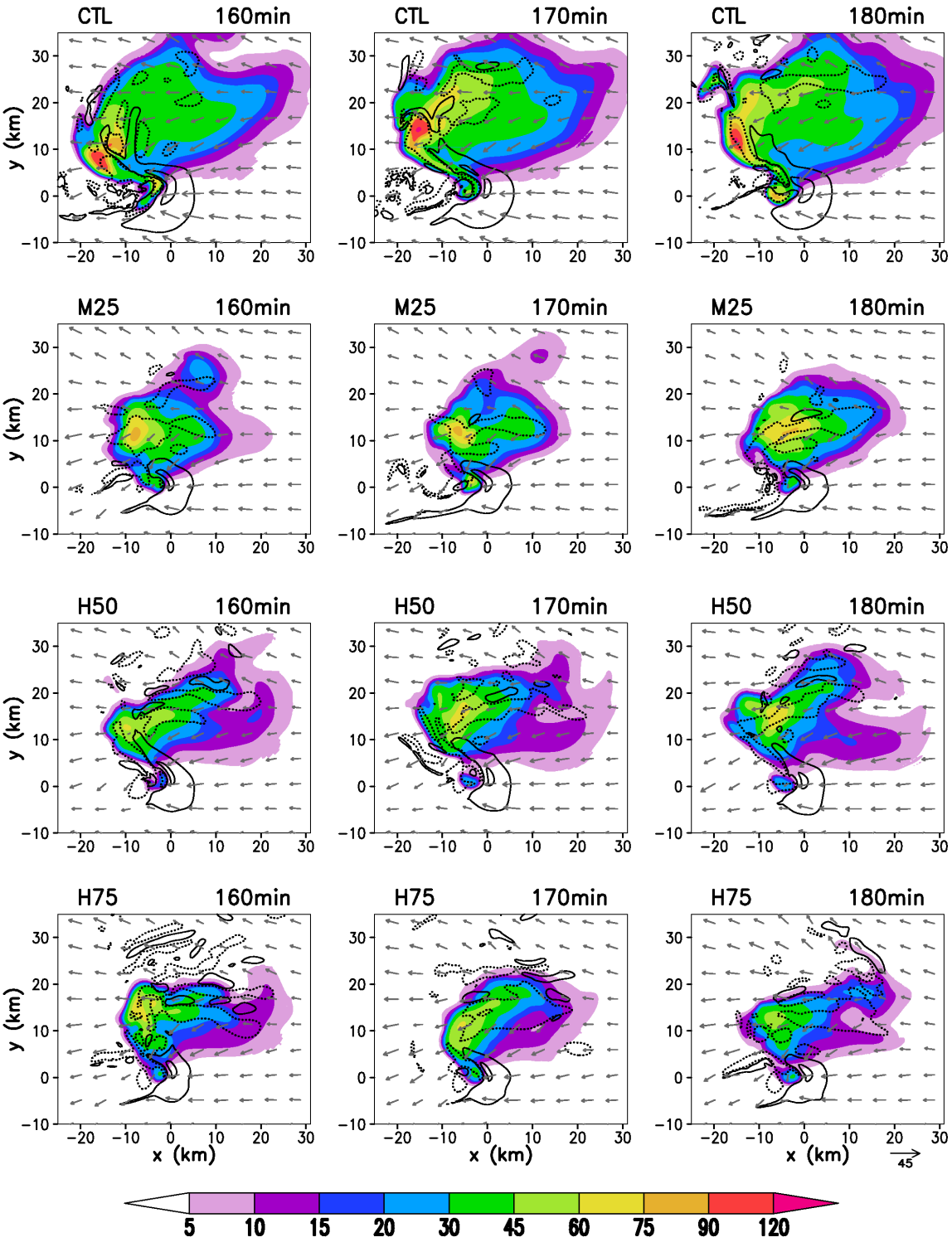

Fig. 3.5. Surface precipitation rate (mm hr^{-1}, shaded); maximum updrafts and downdrafts within the lowest 1 km (black contours; -2, 2, and 10 m s^{-1} contour levels shown, negative values dashed); and storm-relative horizontal winds (m s^{-1}, gray vectors shown every 18th grid point;

vector scale indicated in the bottom right corner) at the lowest model level (~12 m AGL) over the last 20 simulation minutes for simulations CTL (top row), M25 (2nd row), H50 (3rd row), and H75 (bottom row). The horizontal axes are centered on the location of the 6 km maximum updraft at the time indicated in each panel. The figure axes are determined in this manor for the rest of the figures in this chapter.

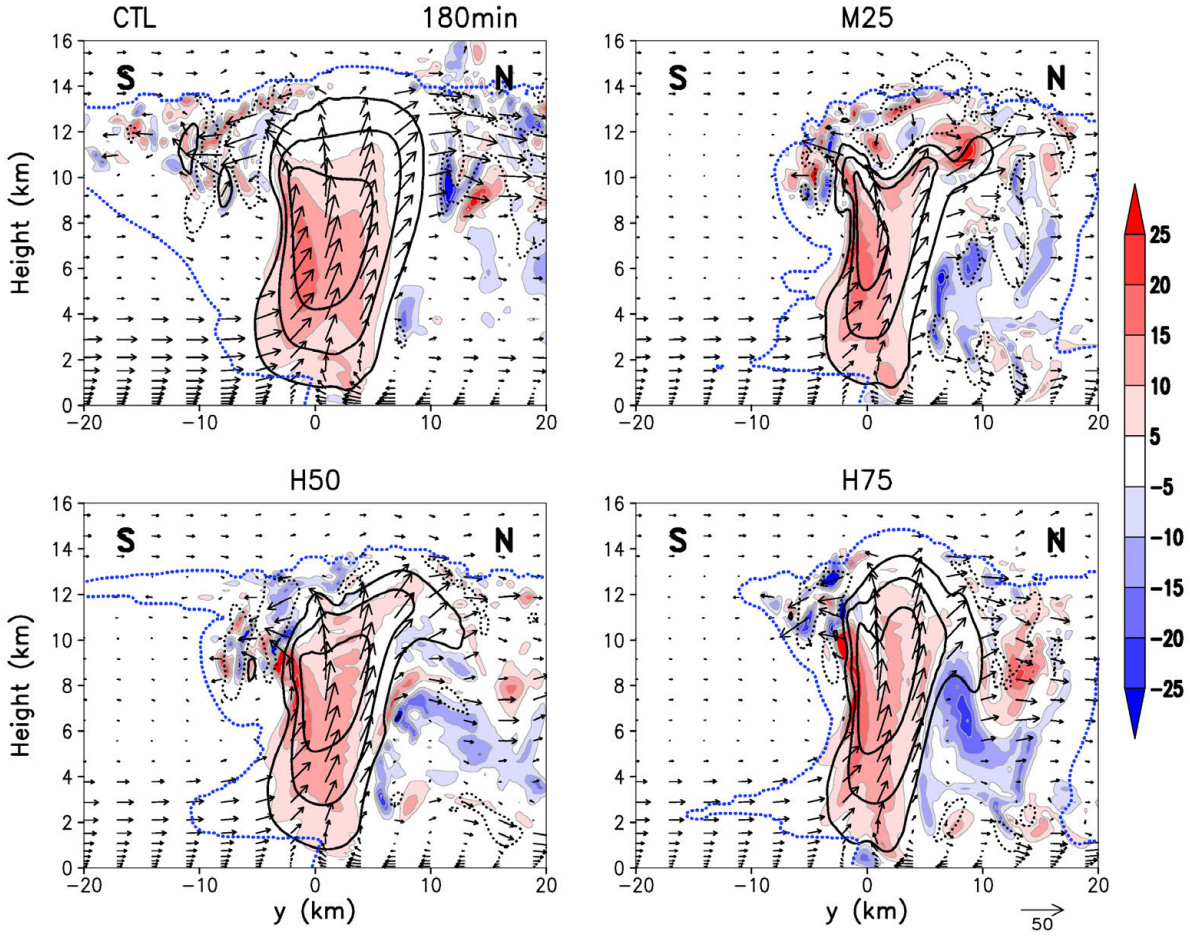

Fig. 3.6. South-north cross sections of vertical relative vorticity (10^{-3} s^{-1}, shaded); vertical velocity (black contours; -5, 10, 25, 40, and 55 m s^{-1} contour levels shown; negative values dashed); total condensate outline (0.01 g kg^{-1} dotted blue contour); and storm-relative v and w winds (m s^{-1}, black vectors shown every 10th grid point in the horizontal and every 3rd grid point in the vertical; vector scale indicated in the bottom right corner) through the maximum ~6 km updraft for simulations CTL, M25, H50, and H75 at 180 min.

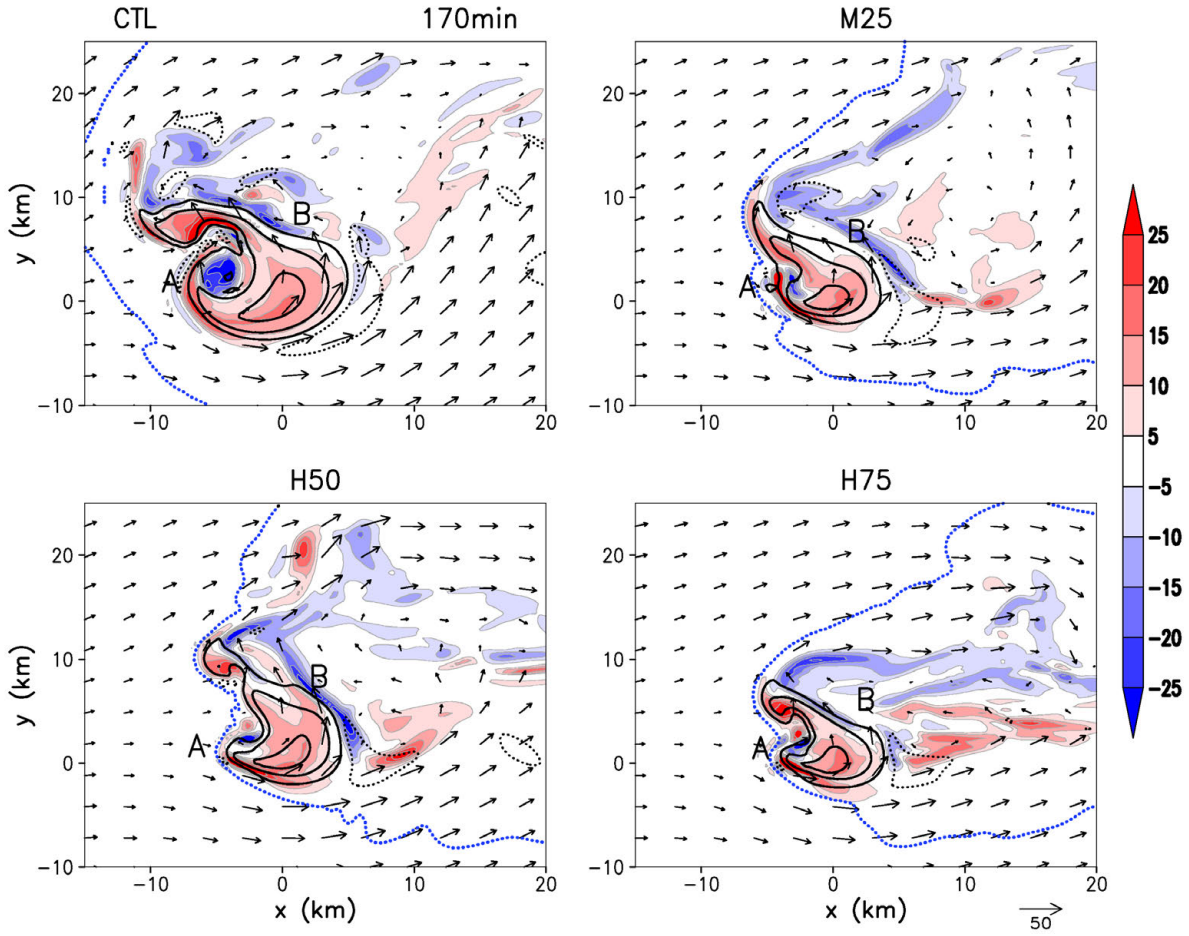

Fig. 3.7. Plan view at ~6 km AGL, with shading, contours, and vectors as in Fig. 3.6 but with horizontal storm relative wind vectors shown every 10th grid point, at 170 min. Annotated points "A" and "B" are discussed in the text.

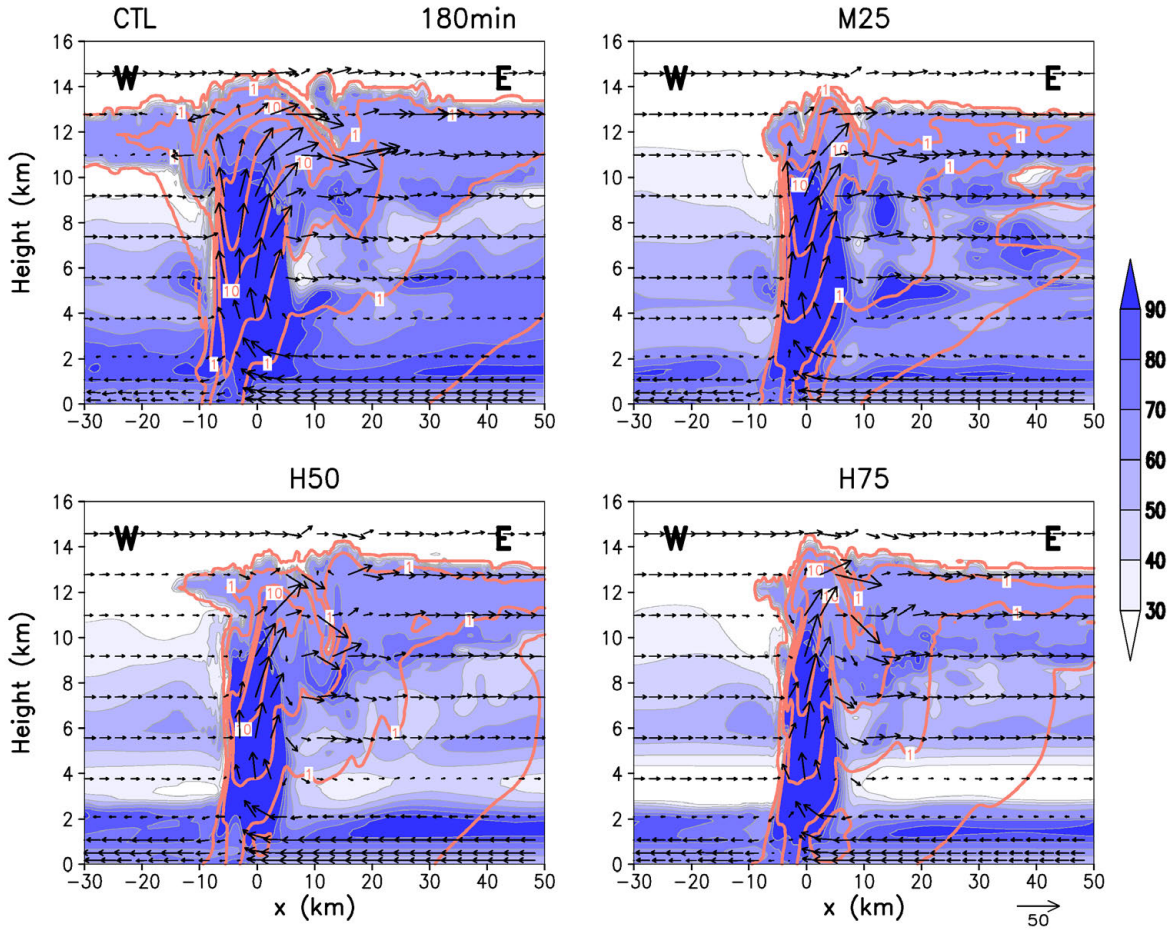

Fig. 3.8. West-east cross section through the location of the maximum ~6 km updraft of relative humidity (%, shaded); total condensate (orange solid contours; 5 g kg^{-1} contour interval with the 0.01 and 1 g kg^{-1} contours also shown); and storm-relative u and w winds (m s^{-1}, black vectors shown every 9th grid point in the horizontal and every 6th grid point in the vertical; vector scale indicated in the bottom right corner) for simulations CTL, M25, H50, and H75 at 180 min.

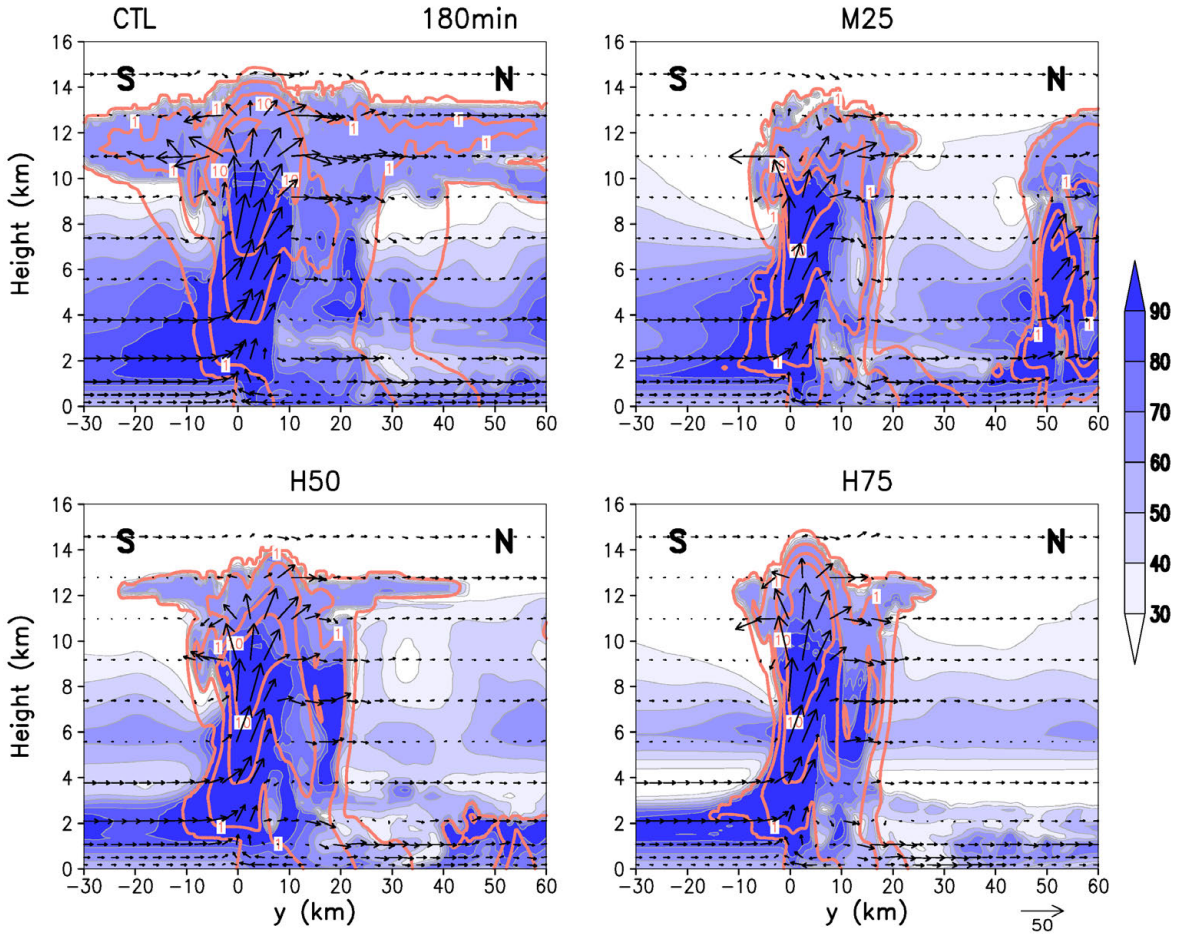

Fig. 3.9. As in Fig. 3.8, but a south-north cross section and with v and w storm-relative wind vectors.

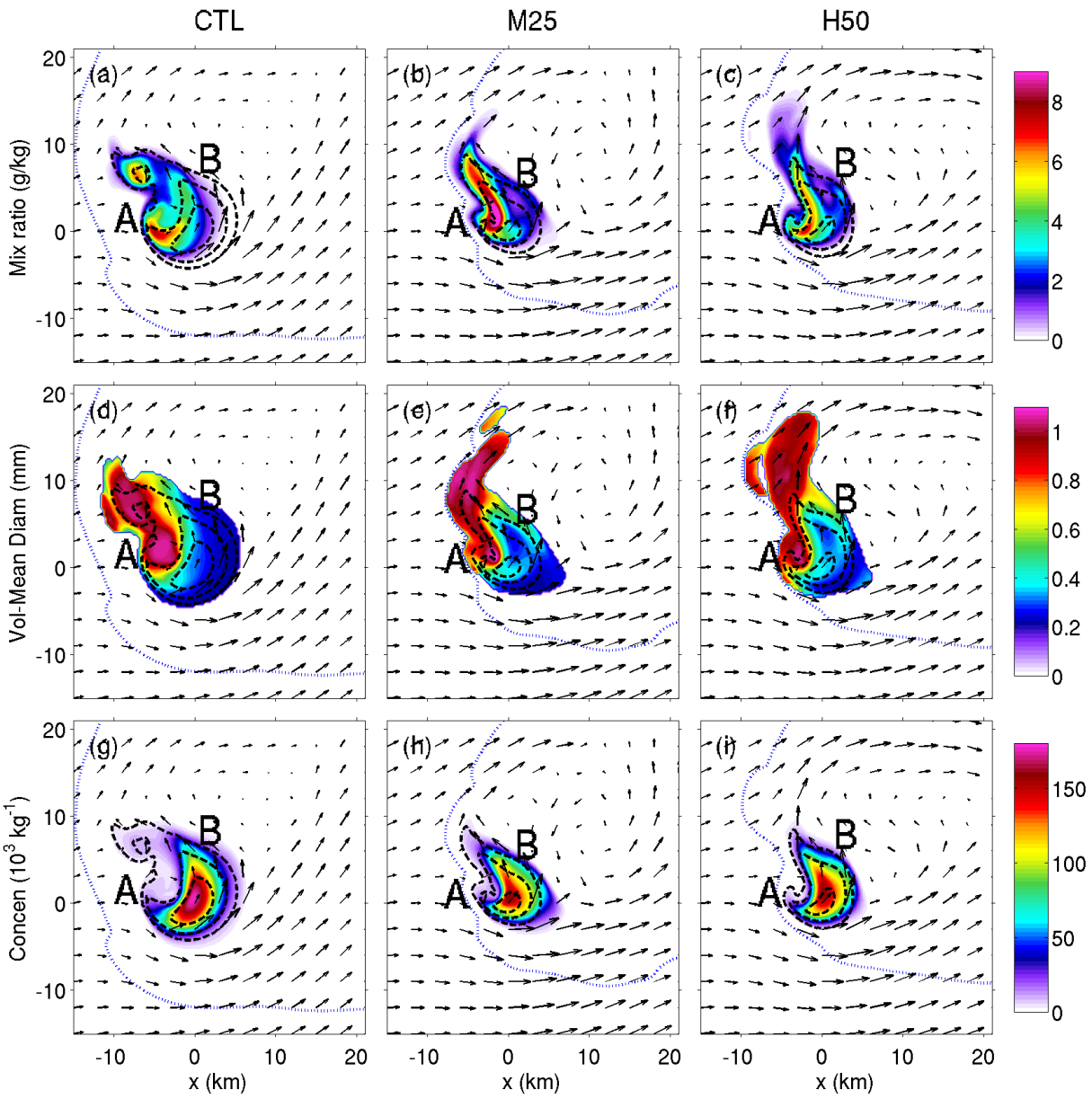

Fig. 3.10. Composite plan view at ~6 km AGL of (a)-(c) rain mixing ratio (g kg^{-1}), (d)-(f) volume-mean rain diameter (mm, only where mixing ratio exceeds 0.05 g kg^{-1}), and (g)-(i) rain number concentration (10^3 kg^{-3}); vertical velocity (10, 25, and 40 m s^{-1} black dashed contours); total condensate outline (0.01 g kg^{-1} blue dotted contour); and storm-relative horizontal winds (m s^{-1}, black vectors shown every 10th grid point) for simulations CTL (left column), M25 (middle column), and H50 (right column). All fields shown in Figs. 3.10-3.13 are composites taken from 160-180 min (21 times) relative to the intensity-weighted updraft center at 6 km AGL; axis numberings are distances (km) from the updraft center. Annotated points "A" and "B" are discussed in the text.

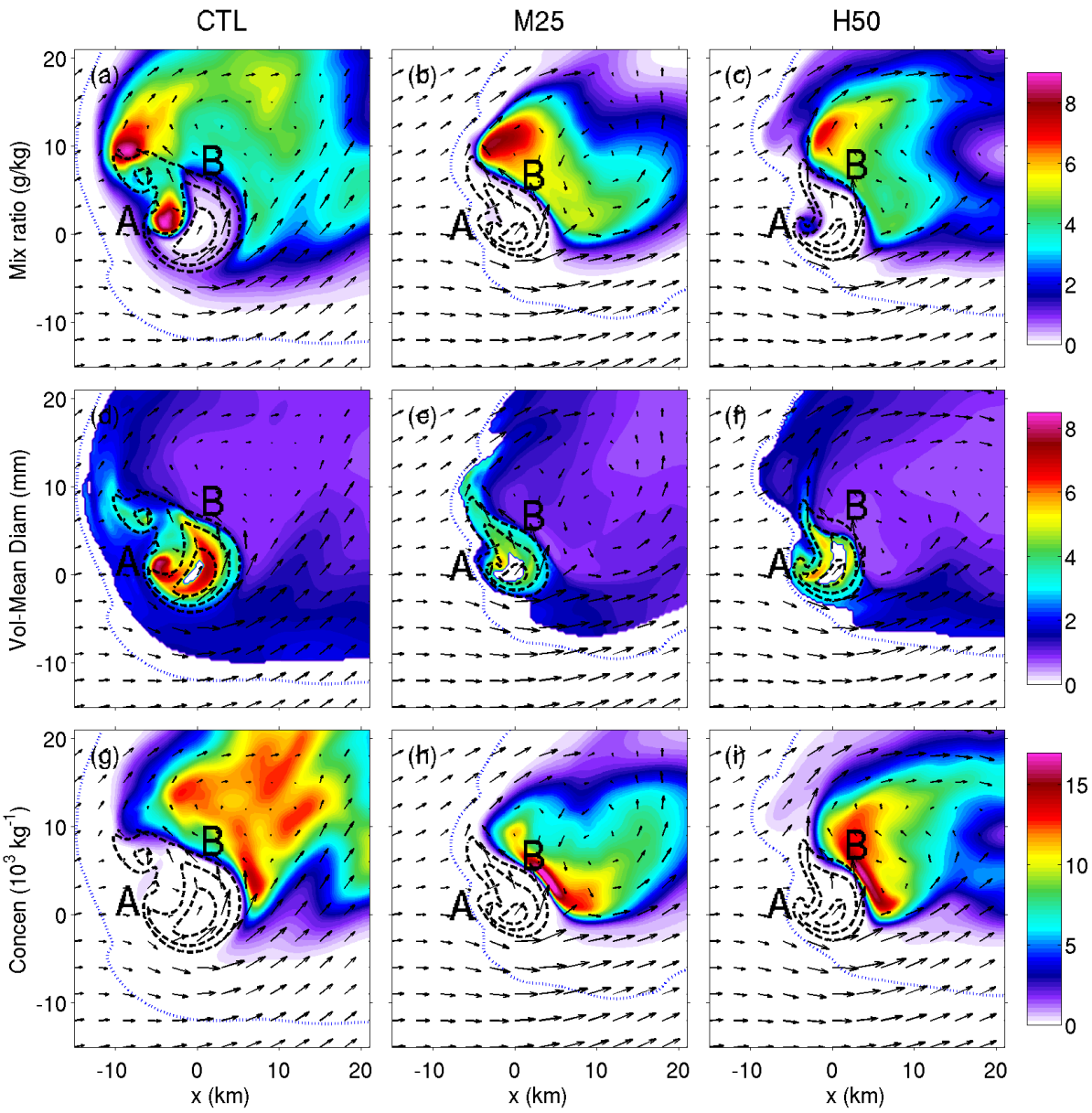

Fig. 3.11. As in Fig. 3.10, but for (a)-(c) hail mixing ratio (g kg^{-1}), (d)-(f) volume-mean hail diameter (mm), and (g)-(i) hail number concentration (10^3 kg^{-1}).

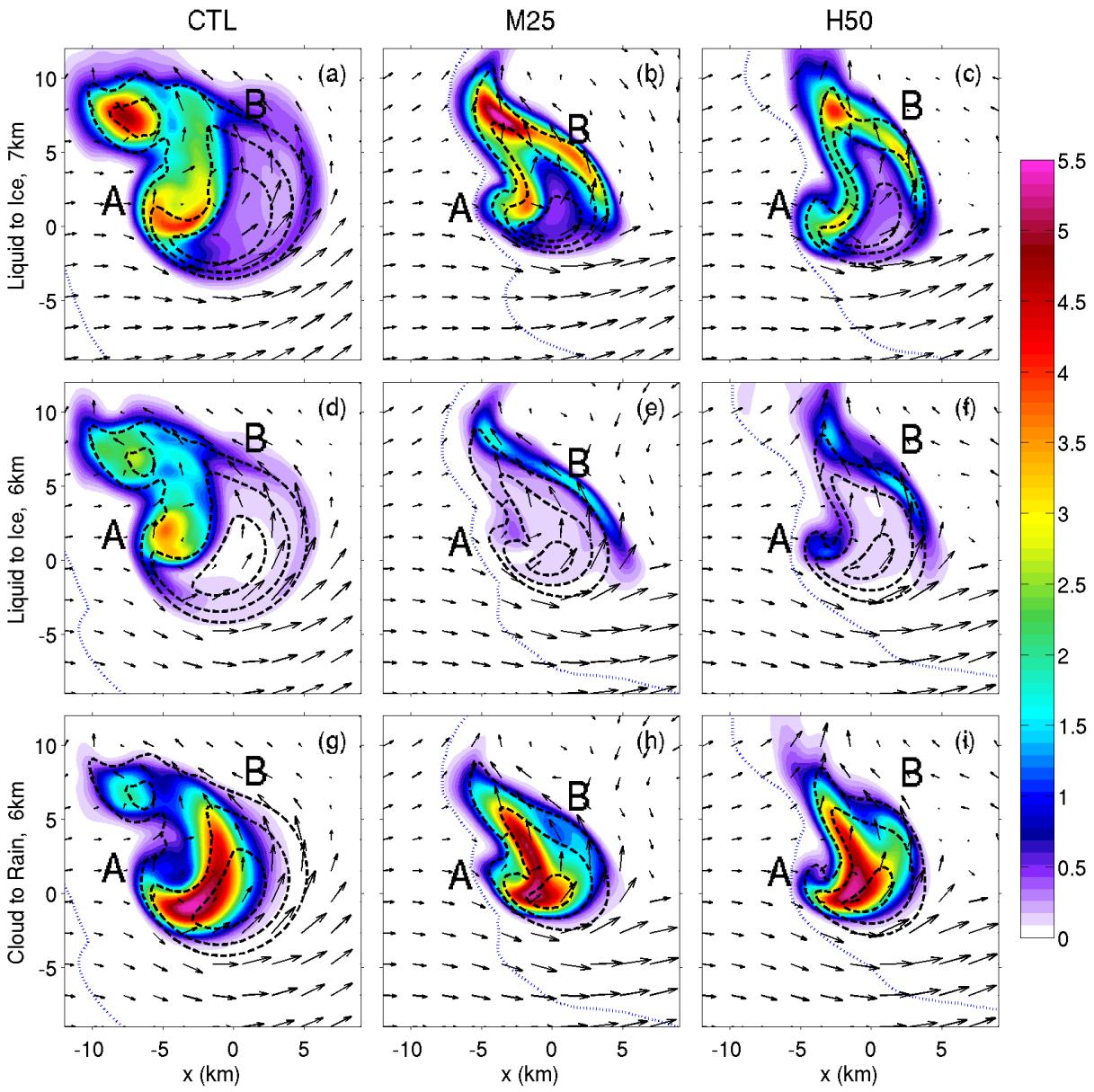

Fig. 3.12. Composite plan views of microphysical budget process rates (g kg^{-1} min^{-1}, shaded) for (a)-(c) cloud and rain water collected by all ice species at 7 km AGL and (d)-(f) at 6 km AGL, and (g)-(i) conversion of cloud to rain water by collection at 6 km AGL; updraft speed (10, 25, and 40 m s^{-1} dashed black contours); and total condensate outline (0.01 g kg^{-1} blue dotted contour) for simulations CTL (left column), M25 (middle column), and H50 (right column). Composite fields are calculated as in Fig. 3.10. Annotated points "A" and "B" are discussed in the text.

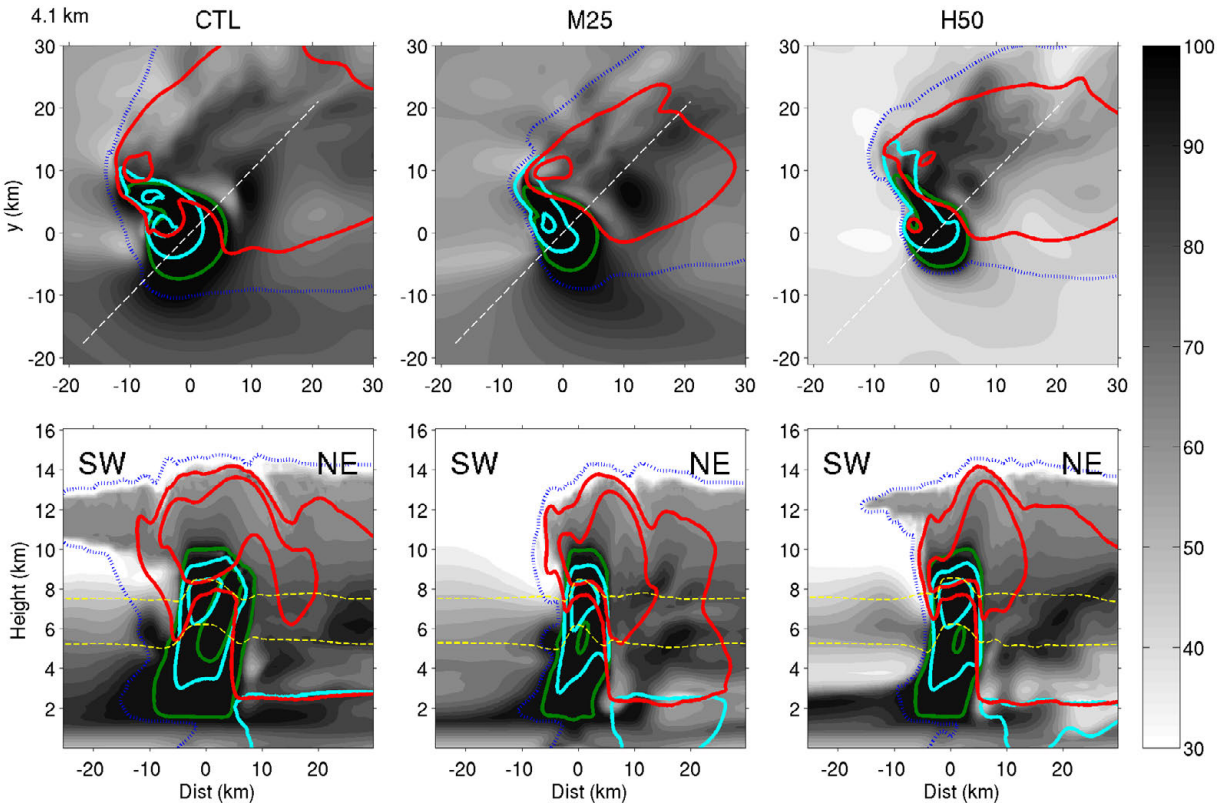

Fig. 3.13. Composite plan view at 4.1 km AGL (top row) and southwest-to-northeast cross sections (bottom row) of relative humidity (shaded); cloud mixing ratio (cyan solid contours); drizzle + rain mixing ratio (green solid contours); hail mixing ratio (red solid contours); temperature (-10 °C and -25 °C yellow dashed contours); and total condensate outline (0.01 g kg^{-1} blue dotted contour) for simulations CTL (left column), M25 (middle column), and H50 (right column). The 0.5 and 5 g kg^{-1} mixing ratio contours are shown. Composite fields are calculated as in Fig. 3.10. White dashed contours in the plan views indicate the location of the cross sections.

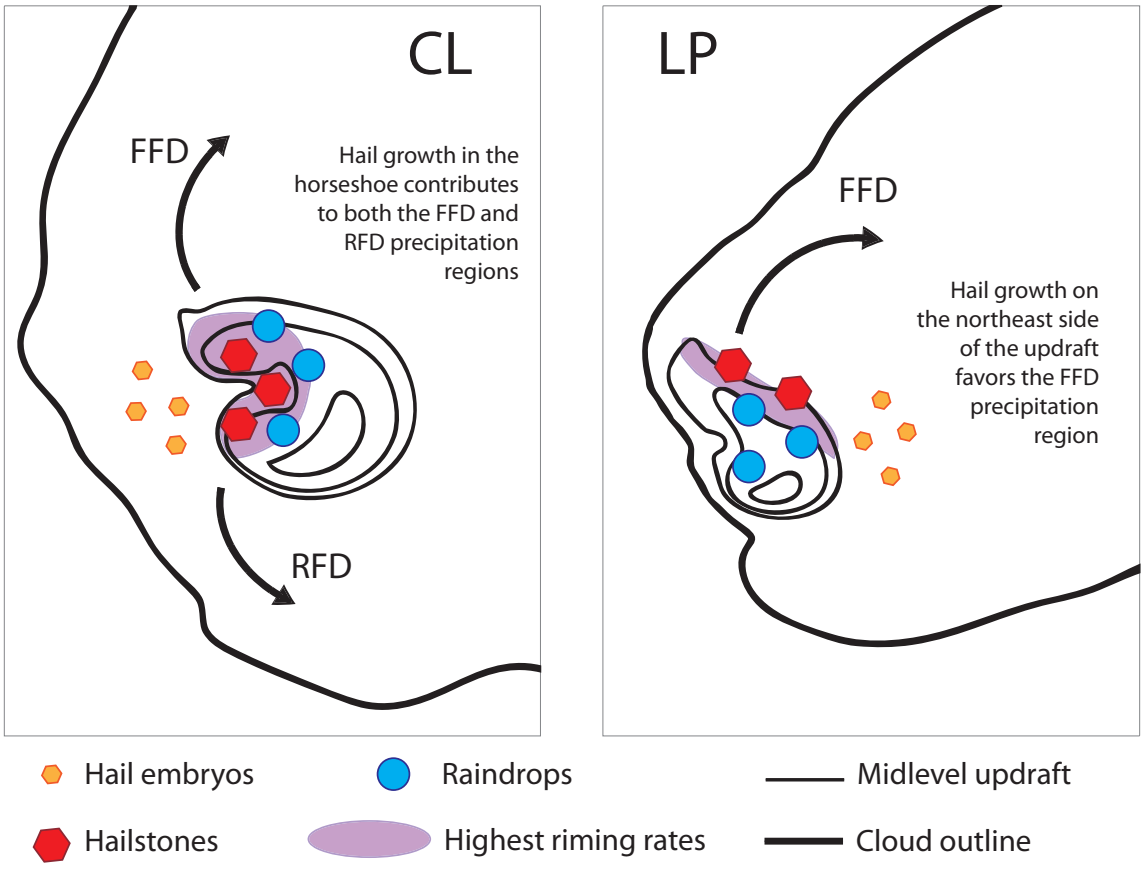

Fig. 3.14. Schematic diagram of the primary midlevel hail growth mechanisms in classic and low-precipitation supercells. The cloud outline (0.01 g kg^{-1} total condensate) and midlevel updraft speeds (10, 25, and 45 m s^{-1}) are taken from composite fields at 7 km for CTL and M25.

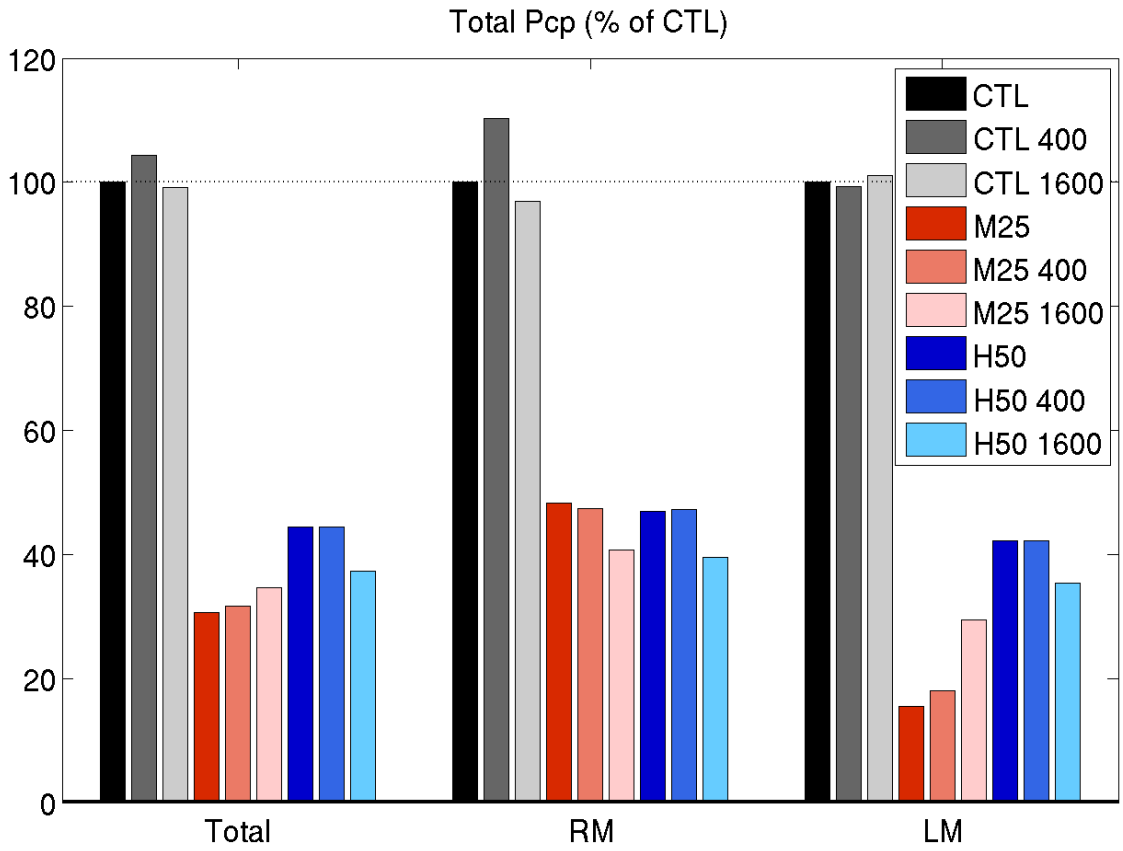

Fig. 3.15. Total accumulated precipitation over the entire domain (left), over just the southern portion encompassing the precipitation from the right-mover (RM) (middle), and over just the northern portion containing the precipitation resulting from the left-moving cluster (LM) (right) for the aerosol sensitivity tests, expressed as a percentage of the precipitation in CTL. The domain was divided into the RM and LM portion as described in the text.

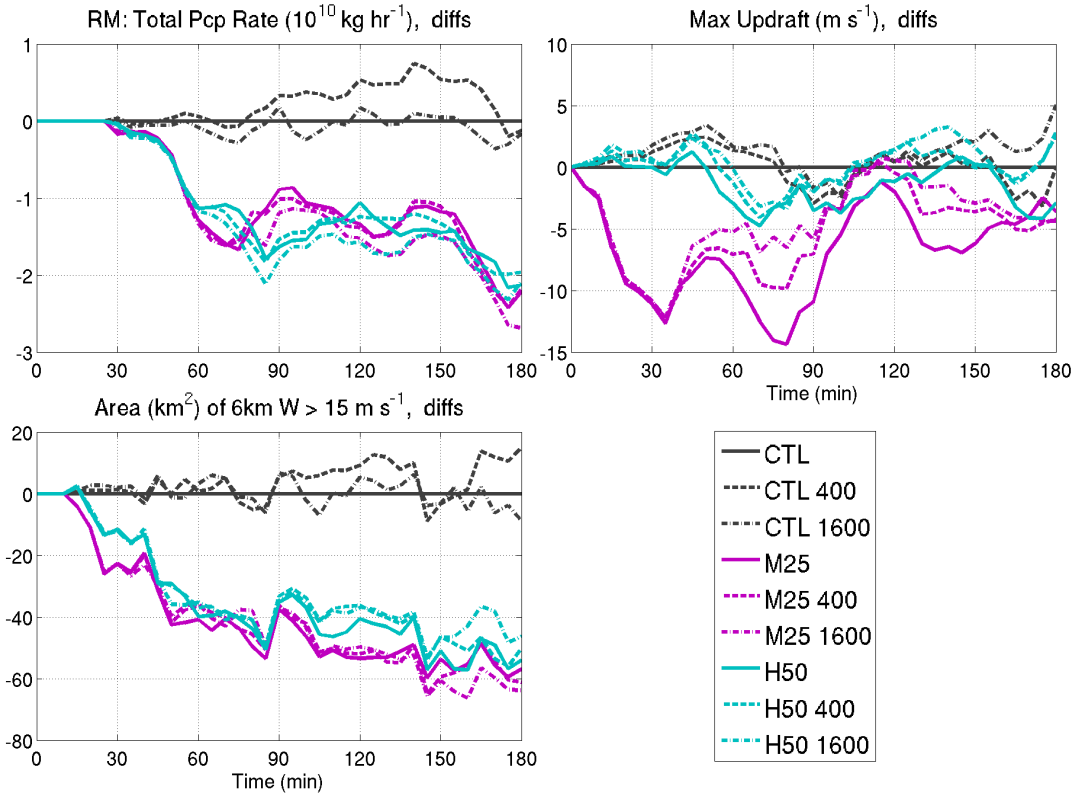

Fig. 3.16. Time series for the right-moving storm as in Fig. 3.4, but for the aerosol sensitivity tests, expressed as differences from simulation CTL. The maximum updraft line has been smoothed to show the trends more clearly.

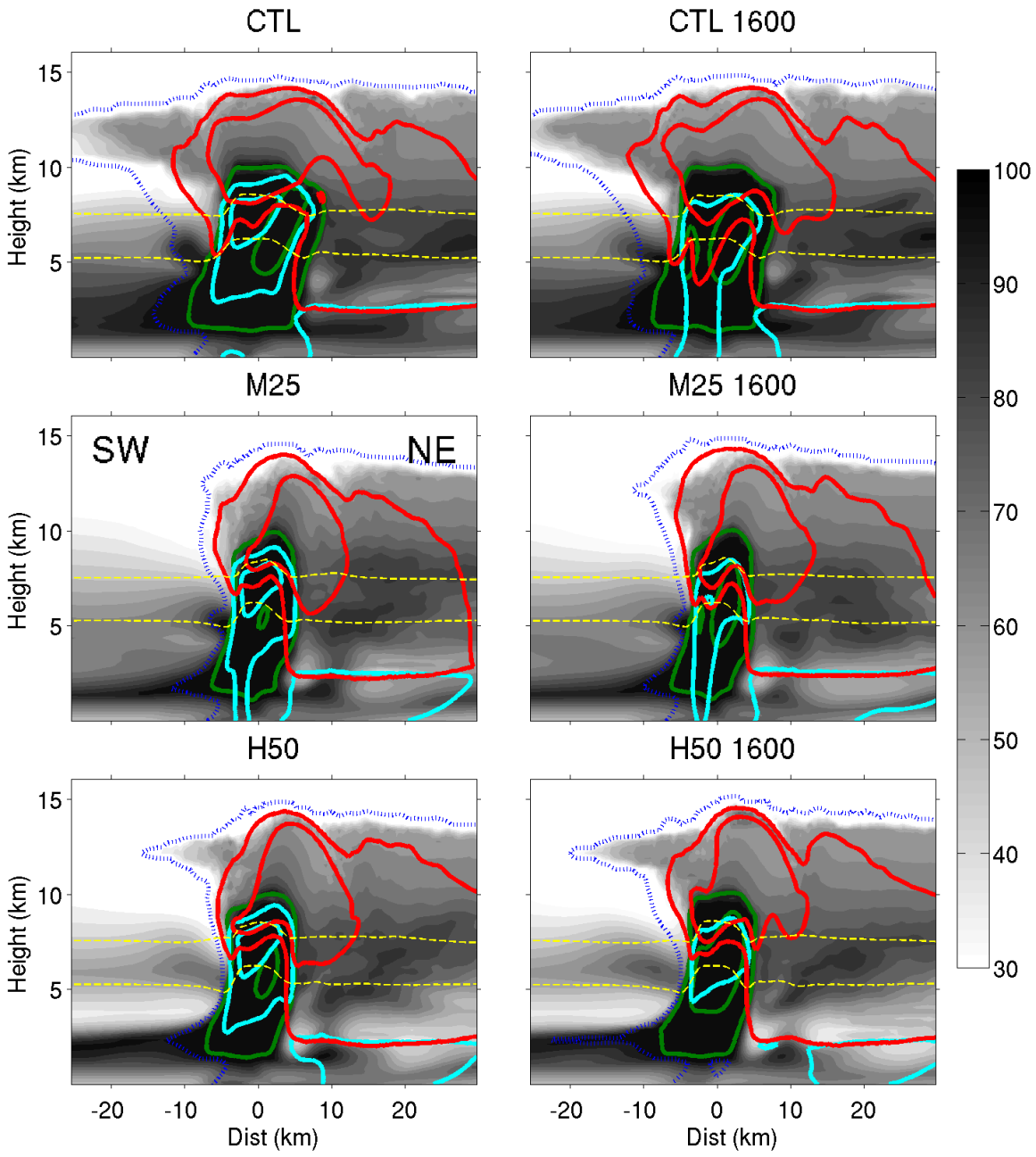

Fig. 3.17. Composite southwest-to-northeast cross sections for CTL (top row), M25 (middle row), and H50 (bottom row) moisture profiles for the cleanest (left column) and most polluted (right column) aerosol tests. Shading and contours are as in Fig. 3.13. Composite fields are calculated with 5-minute data from minutes 105 through 180 (16 times).

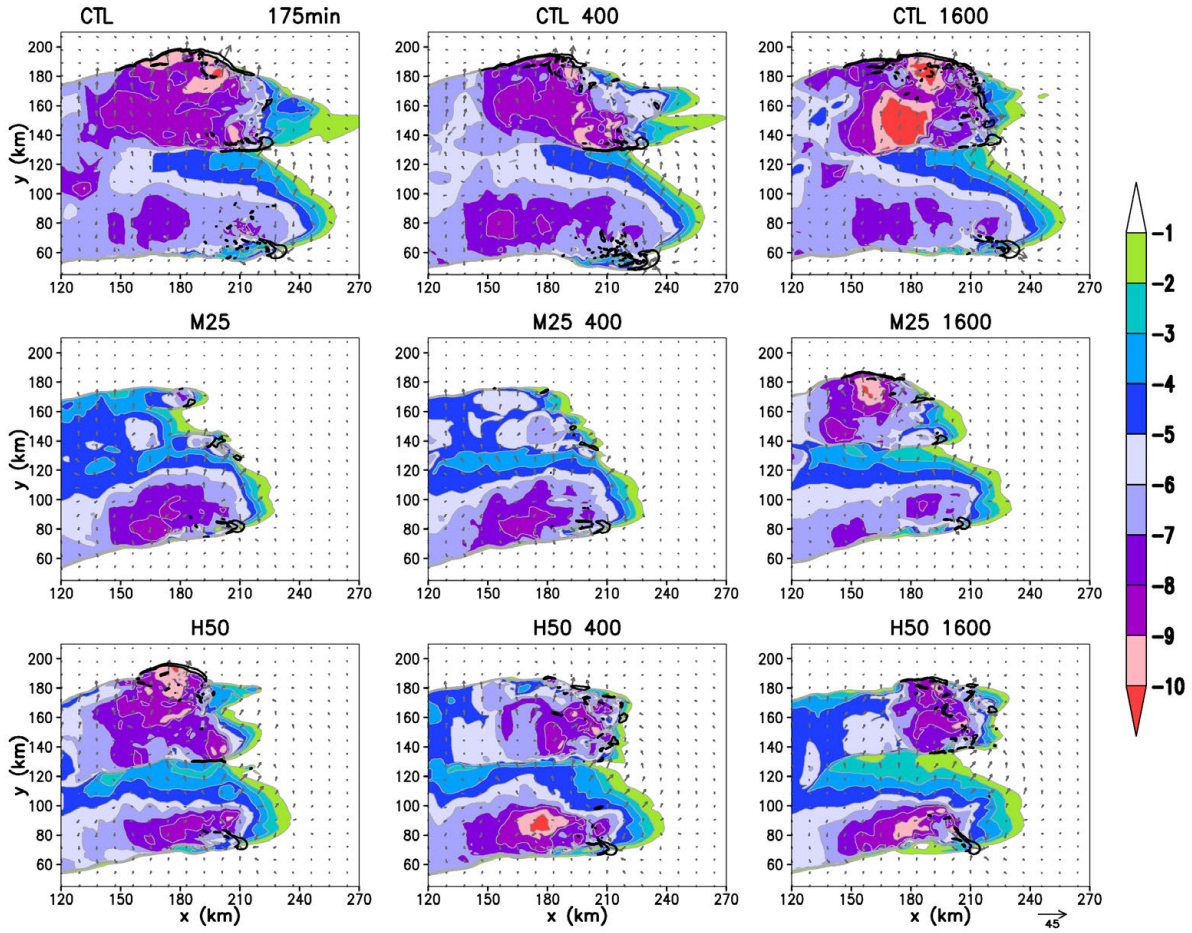

Fig. 3.18. Plan view of perturbation potential temperature at the lowest model level, 12 m AGL (K, shaded); convergence at 0.5 km (0.005 s^{-1} black contour); and 12 m horizontal wind (m s^{-1}, gray vectors shown every 30th grid point; vector scale indicated in the bottom right corner) for the simulations as described in Fig. 3.17 at 175 min.

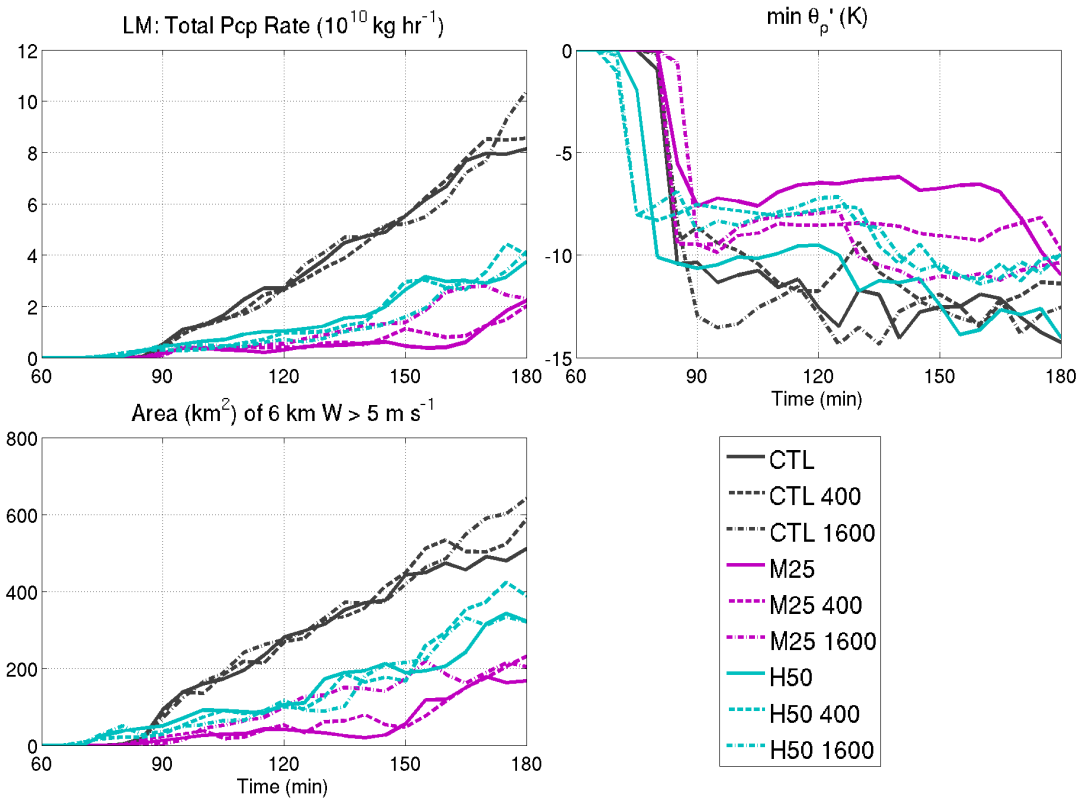

Fig. 3.19. Time series of characteristics for the northern portion of the domain that contains the precipitation resulting from the left-moving cluster. Top left: total precipitation rate, calculated in the same way as in Fig. 3.4; top right: minimum perturbation density temperature within the lowest 100 m, where density temperature is as defined in Tompkins (2001); bottom left: total area of updrafts exceeding 5 m s^{-1} at 6 km AGL.

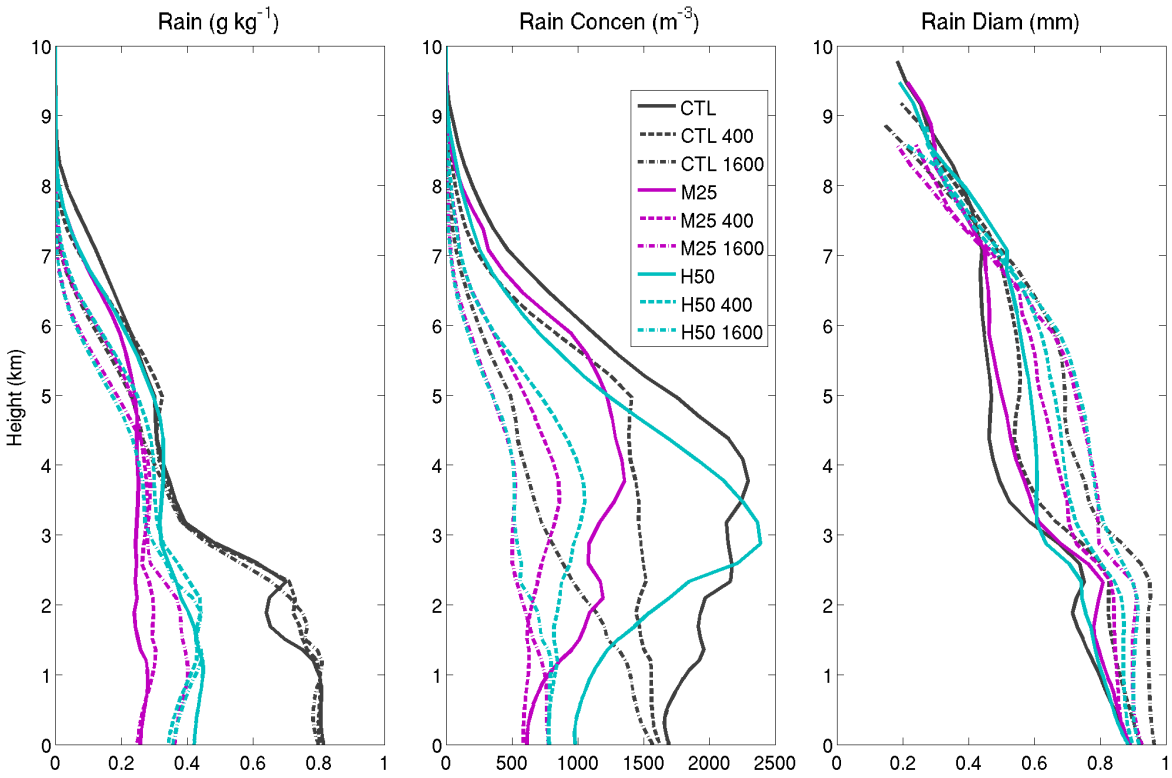

Fig. 3.20. Rain mixing ratio, number concentration, and mean diameter averaged spatially over the northern portion of the domain containing the left-mover precipitation and temporally from 90-180 min. The mixing ratio and number concentrations are averaged only over cloudy points (total condensate > 0.01 g kg^{-1}) and mean diameters are averaged only where rain mixing ratio > 0.01 g kg^{-1}.

CHAPTER 4: OVERALL SUMMARY AND DISCUSSION

As described in chapter 1 and summarized in a review by Tao et al. (2012), recent studies of aerosol-cloud interactions have revealed an increasingly complex picture from our initial understanding of aerosol impacts on shallow warm-phase clouds (Twomey 1977; Albrecht 1989; Ackerman et al. 2000) and convective invigoration within deep convection (Andreae et al. 2004). Additional complexities have been added piece by piece, including different precipitation responses to aerosols for different cloud types (e.g. Seifert and Beheng 2006; van den Heever et al. 2011), the modulating effects of environmental humidity (e.g. Khain et al. 2008), wind shear, (Fan et al. 2009), and convective instability (Storer et al. 2010), and consideration of feedbacks within a larger system context (e.g. Jiang and Feingold 2006; van den Heever et al. 2011). The overall goal of the research presented in this thesis has therefore been to enhance our understanding of aerosol impacts on various types of organized deep convection under the modulating influence of the environment, including land surface processes and midlevel moisture content. This goal has been achieved through the use of idealized cloud-resolving modeling simulations with RAMS. The main findings from these studies include the following:

- The strength of aerosol impacts on deep convection varies inversely with the level of convective organization.
- The environment, as well as system feedbacks, modulate aerosol influences on deep convective precipitation.

The first study investigated aerosol-cloud-land surface interactions within tropical sea breeze convection, which was the most weakly organized convection considered here. Idealized simulations were conducted in which feedbacks were allowed to occur between aerosols, clouds,

precipitation, radiation, and the land surface. Aerosol concentrations, the surface roughness length, and the soil moisture were systematically perturbed and the resulting changes to the sea breeze rainfall were analyzed. It was found that both aerosols and soil moisture decrease the rainfall produced by the sea breeze through changes in the surface latent and sensible heat fluxes. Though the individual influences of aerosols and soil moisture dominated the changes to the sea breeze convection when their perturbations were large, under more moderate perturbations, synergistic interactions between aerosols and the land surface parameters acted to enhance the sea breeze convection. The synergistic feedbacks occurred through their mutual influence on the low level convergence and gust front interaction with the sea breeze front. The possible feedbacks between aerosols, clouds, and the land surface have, to our knowledge, only been investigated in one other study of cumulus clouds over land (Jiang and Feingold 2006). That the aerosol-radiative interactions reduced the land surface fluxes, the strength of the convection, and the magnitude of aerosol indirect effects in both Jiang and Feingold (2006) and the present study is an important result, since the two types of convection in these studies have very different behaviors. This highlights the importance of including aerosol direct effects and feedbacks to the surface fluxes in studies of aerosol-cloud interactions for continental convection.

In the second study, the relative influence of midlevel moisture and aerosols on deep convective morphology, including supercells and multicells, was investigated. Midlevel dryness was systematically varied and aerosol concentrations enhanced for several of the moisture profiles within idealized simulations of a storm-splitting event in which the right-mover becomes a dominant supercell and the left-mover evolves into the multicellular cluster. The results indicated that supercell morphology was most sensitive to the midlevel moisture content. With increasing dryness aloft, the right-mover transitioned from a classic to a low-precipitation

supercell (Grant and van den Heever 2014), but the supercells showed very little sensitivity to aerosol concentrations. While the midlevel moisture content also dominated the precipitation changes in the multicellular convection, aerosols did impact the surface rainfall through feedbacks to the strength of the cold pool. It was found that both the sign and magnitude of the precipitation response to aerosols depends on the vertical distribution of moisture. These results demonstrate fundamental differences in the mechanisms by which aerosols can impact the precipitation in supercells and multicells, by virtue of the differences in the dynamics associated with these cloud types. Supercells are dynamically driven by strong vertical perturbation pressure gradients induced by the rotating mesocyclone, whereas multicells are driven by low-level cold pool forcing. Aerosols can influence supercellular precipitation through their impact on rain formation efficiency within the organized rotating mesocyclone, although the net effect is quite small. On the other hand, aerosols influence the multicellular precipitation mainly through changes in evaporatively-driven downdrafts and the microphysical characteristics of the raindrops.

The results from both of these studies demonstrate that, while classifying aerosol impacts on deep convection by environmental parameters (e.g. Khain 2009) is highly useful, such generalities are not necessarily applicable when considering the system response of precipitation to aerosols. For example, Khain et al. (2008) and Khain (2009) suggest that generally, aerosols increase the precipitation from mesoscale-organized deep convection in more humid (e.g. tropical) environments and decrease the precipitation in drier (e.g. continental) environments. However, the results in this study do not conform to this more generalized classification. The tropical sea breeze precipitation was reduced with increasing aerosol concentrations because of the inclusion of aerosol direct effects and their influence on the surface fluxes, even though the

environment was very moist and the vertical wind shear was weak. Conversely, when low-level moisture was reduced by decreasing soil moisture, synergistic feedbacks between aerosols and soil moisture enhanced the precipitation, which is again the opposite response to that predicted by the classification. Furthermore, for the midlatitude multicellular convection studied here, precipitation was found to either increase or decrease with midlevel dryness, depending on how the dryness was vertically distributed. These rainfall responses demonstrate a more complicated picture than suggested in Khain (2009).

Overall, the results in this study complement findings in previous studies such as Seifert and Behing (2006) and Storer et al. (2010) in that both the environment and the dynamics modulate the response of deep convection to aerosol forcing. In both sets of simulations presented herein, the moisture availability has a controlling influence on both the precipitation response and storm morphology, while the aerosol impacts are secondary. Furthermore, the magnitude by which aerosols can impact convective precipitation is regulated by the level of organization, both within specific types of deep convection (e.g. multicells or supercells) and within the broader spectrum of organized deep convection. The tropical sea breeze convection and resulting precipitation was found to be the most sensitive to aerosol concentrations in these studies, while the more organized multicellular convection was less sensitive and the highly organized supercell the least sensitive to aerosols. Within the different supercells simulated here, M25 was both the most sensitive to aerosols and also the least organized in terms of its updraft steadiness and strength. Similarly, the multicellular convection in M25, which was also the weakest of the multicellular convection, demonstrated the strongest response to aerosols.

Both of these studies have also highlighted the importance of taking into account the cold pool strength and resulting gust front convergence forcing for secondary convection when

considering aerosol impacts on deep convection, in agreement with other recent studies (e.g. Khain et al. 2005; van den Heever and Cotton 2007; Storer et al. 2010; Morrison 2012). More weakly dynamically forced convective regimes in which the cold pool and outflow strength play an integral role in the convective lifetime and total precipitation produced may therefore be some of the most susceptible deep convective cloud systems to aerosol perturbations. In order to better understand and characterize aerosol impacts on these types of cloud systems, extensive observations of cold pools are needed in order to verify model findings and to critically evaluate model microphysical schemes, which are known to have a major influence on simulated convective cold pools and outflow strength (e.g. van den Heever and Cotton 2004; Khain and Lynn 2009; James and Markowski 2010; Morrison 2012; Adams-Selin et al. 2013a, 2013b).

Given the importance of cold pool interactions and feedbacks in evaluating aerosol influences on deep convection, an important next step in this research is to evaluate the relative sensitivity of midlatitude multicellular convection to aerosols while allowing for other feedbacks within the system that can modify the cold pools, as was included in the tropical sea breeze study. In particular, aerosol direct effects and surface fluxes need to be included, which will impact the convective cold pool strength and cold pool recovery time. Finally, the vertical structure of the aerosol perturbation may have important impacts on the atmospheric stability profile (e.g. Yu et al. 2002; Feingold et al. 2005). The presence of stable layers within the environment impacts cold pool propagation and depth. Propagation is also sensitive to the altitude of the stable layers (e.g. Seigel and van den Heever 2012; Robinson et al. 2013). Variations in the vertical distribution of aerosols and resulting stability profile could also affect the sea breeze propagation and structure, as well as modulate the precipitation response. Although very little work has been done on the impact of variations in the vertical distribution of

aerosols on deep convection (e.g. Fridland et al. 2004), such work is a promising avenue for future research and is currently underway.

REFERENCES

Ackerman, A. S., 2000: Reduction of tropical cloudiness by soot. *Science*, **288**, 1042–1047.

Adams-Selin, R. D., S. C. van den Heever, and R. H. Johnson, 2013a: Sensitivity of Bow-Echo Simulation to Microphysical Parameterizations. *Wea. Forecasting*, **28**, 1188–1209.

Adams-Selin, R. D., S. C. van den Heever, and R. H. Johnson, 2013b: Impact of Graupel Parameterization Schemes on Idealized Bow Echo Simulations. *Mon. Wea. Rev.*, **141**, 1241–1262.

Albrecht, B. A., 1989: Aerosols, cloud microphysics, and fractional cloudiness. *Science*, **245**, 1227–1230.

Alpert, P., S. O. Krichak, T. N. Krishnamurti, U. Stein, and M. Tsidulko, 1996: The Relative Roles of Lateral Boundaries, Initial Conditions, and Topography in Mesoscale Simulations of Lee Cyclogenesis. *J. Appl. Meteor.*, **35**, 1091–1099.

Alpert, P., and T. Sholokhman, eds., 2011: *Factor Separation in the Atmosphere*. Cambridge University Press, 274 pp.

Altaratz, O., I. Koren, T. Reisin, a. Kostinski, G. Feingold, Z. Levin, and Y. Yin, 2008: Aerosols' influence on the interplay between condensation, evaporation and rain in warm cumulus cloud. *Atmos. Chem. Phys.*, **8**, 15–24.

Andreae, M. O., and D. Rosenfeld, 2008: Aerosol–cloud–precipitation interactions. Part 1. The nature and sources of cloud-active aerosols. *Earth Sci. Rev.*, **89**, 13–41.

Andreae, M. O., D. Rosenfeld, P. Artaxo, A. A. Costa, G. P. Frank, K. M. Longo, and M. A. F. Silva-Dias, 2004: Smoking rain clouds over the Amazon. *Science*, **303**, 1337–1342.

Atkins, N. T., R. M. Wakimoto, and T. M. Weckwerth, 1995: Observations of the Sea-Breeze Front during CaPE. Part II: Dual-Doppler and Aircraft Analysis. *Mon. Wea. Rev.*, **123**, 944–969.

Avissar, R., and D. Werth, 2005: Global Hydroclimatological Teleconnections Resulting from Tropical Deforestation. *J. Hydrometeor.*, **6**, 134–145.

Baker, R. D., B. H. Lynn, A. Boone, W.-K. Tao, and J. Simpson, 2001: The Influence of Soil Moisture, Coastline Curvature, and Land-Breeze Circulations on Sea-Breeze-Initiated Precipitation. *J. Hydrometeor.*, **2**, 193–211.

Balas, N., S. E. Nicholson, and D. Klotter, 2007: The relationship of rainfall variability in West Central Africa to sea-surface temperature fluctuations. *Int. J. Climatol.*, **27**, 1335–1349.

Beatty, K., E. N. Rasmussen, and J. M. Straka, 2008: The Supercell Spectrum. Part I: A Review of Research Related to Supercell Precipitation Morphology. *Electron. J. Severe Storms Meteor.*, **3**, 1–21.

Berg, W., T. L'Ecuyer, and S. van den Heever, 2008: Evidence for the impact of aerosols on the onset and microphysical properties of rainfall from a combination of satellite observations and cloud-resolving model simulations. *J. Geophys. Res.*, **113**, D14S23.

Betts, A. K., 2007: Coupling of water vapor convergence, clouds, precipitation, and land-surface processes. *J. Geophys. Res.*, **112**, D10108.

Betts, A. K., 2009: Land-surface-atmosphere coupling in observations and models. *J. Adv. Model. Earth Syst.*, **2**, 4.

Bluestein, H. B., 1984: Further Examples of Low-Precipitation Severe Thunderstorms. *Mon. Wea. Rev.*, **112**, 1885–1888.

Bluestein, H. B., and C. R. Parks, 1983: A Synoptic and Photographic Climatology of Low-Precipitation Severe Thunderstorms in the Southern Plains. *Mon. Wea. Rev.*, **111**, 2034–2046.

Bluestein, H. B., and G. R. Woodall, 1990: Doppler-Radar Analysis of a Low-Precipitation Severe Storm. *Mon. Wea. Rev.*, **118**, 1640–1665.

Bluestein, H. B., and S. G. Gaddy, 2001: Airborne Pseudo-Dual-Doppler Analysis of a Rear-Inflow Jet and Deep Convergence Zone within a Supercell. *Mon. Wea. Rev.*, **129**, 2270–2289.

Brooks, H. E., and R. B. Wilhelmson, 1992: Numerical simulation of a low-precipitation supercell thunderstorm. *Meteor. Atmos. Phys.*, **49**, 3–17.

Brooks, H. E., C. A. Doswell, and R. B. Wilhelmson, 1994: The Role of Midtropospheric Winds in the Evolution and Maintenance of Low-Level Mesocyclones. *Mon. Wea. Rev.*, **122**, 126–136.

Browning, K. A., 1964: Airflow and Precipitation Trajectories Within Severe Local Storms Which Travel to the Right of the Winds. *J. Atmos. Sci.*, **21**, 634–639.

Browning, K. A., 1977: The structure and mechanism of hailstorms. *Hail: A Review of Hail Science and Hail Suppression, Meteor. Monogr.*, No. 38, Amer. Meteor. Soc., 1–43.

Browning, K. A., and G. B. Foote, 1976: Airflow and hail growth in supercell storms and some implications for hail suppression. *Quart. J. Roy. Meteor. Soc.*, **102**, 499–533.

Burgess, D. W., and R. P. Davies-Jones, 1979: Unusual Tornadic Storms in Eastern Oklahoma on 5 December 1975. *Mon. Wea. Rev.*, **107**, 451–457.

Byko, Z., P. Markowski, Y. Richardson, J. Wurman, and E. Adlerman, 2009: Descending Reflectivity Cores in Supercell Thunderstorms Observed by Mobile Radars and in a High-Resolution Numerical Simulation. *Wea. Forecasting*, **24**, 155–186.

Cai, H., W.-C. Lee, T. M. Weckwerth, C. Flamant, and H. V. Murphey, 2006: Observations of the 11 June Dryline during IHOP_2002—A Null Case for Convection Initiation. *Mon. Wea. Rev.*, **134**, 336–354.

Carbone, R. E., J. W. Wilson, T. D. Keenan, and J. M. Hacker, 2000: Tropical Island Convection in the Absence of Significant Topography. Part I: Life Cycle of Diurnally Forced Convection. *Mon. Wea. Rev.*, **128**, 3459–3480.

Ciesielski, P. E. and Coauthors, 2014: Quality-controlled upper-air sounding dataset for DYNAMO/CINDY/AMIE: development and corrections. *J. Atmos. Oceanic Technol.*, in press.

Cotton, W. R. and Coauthors, 2003: RAMS 2001: Current status and future directions. *Meteor. Atmos. Phys.*, **82**, 5–29.

Cowie, S. M., P. Knippertz, and J. H. Marsham, 2013: Are vegetation-related roughness changes the cause of the recent decrease in dust emission from the Sahel? *Geophys. Res. Lett.*, **40**, 1868–1872.

Crosman, E. T., and J. D. Horel, 2010: Sea and Lake Breezes: A Review of Numerical Studies. *Boundary Layer Meteor.*, **137**, 1–29.

Darby, L. S., R. M. Banta, and R. A. Pielke, 2002: Comparisons between Mesoscale Model Terrain Sensitivity Studies and Doppler Lidar Measurements of the Sea Breeze at Monterey Bay. *Mon. Wea. Rev.*, **130**, 2813–2838.

Davies-Jones, R., 2002: Linear and Nonlinear Propagation of Supercell Storms. *J. Atmos. Sci.*, **59**, 3178–3205.

Davies-Jones, R. P., D. W. Burgess, and L. R. Lemon, 1976: An atypical tornado-producing cumulonimbus. *Weather*, **31**, 336–347.

DeMott, P. J. and Coauthors, 2010: Predicting global atmospheric ice nuclei distributions and their impacts on climate. *Proc. Natl. Acad. Sci.*, **107**, 11217–11222.

Doswell, C. A., 1987: The Distinction between Large-Scale and Mesoscale Contribution to Severe Convection: A Case Study Example. *Wea. Forecasting*, **2**, 3–16.

Doswell, C. A., and D. W. Burgess, 1993: Tornadoes and tornadic storms: A review of conceptual models. *The Tornado: Its Structure, Dynamics, Prediction, and Hazards, Geophys. Monogr.*, Amer. Geophys. Union, 161–172.

Doswell, C. A., A. R. Moller, and R. Przybylinski, 1990: A unified set of conceptual models for variations on the supercell theme. Preprints,*16th Conf. Severe Local Storms*, Kananaskis Park, AB, Canada, Amer. Meteor. Soc., 40–45.

Droegemeier, K. K., and R. B. Wilhelmson, 1985: Three-Dimensional Numerical Modeling of Convection Produced by Interacting Thunderstorm Outflows. Part I: Control Simulation and Low-Level Moisture Variations. *J. Atmos. Sci.*, **42**, 2381–2403.

Droegemeier, K. K., S. M. Lazarus, and R. Davies-Jones, 1993: The Influence of Helicity on Numerically Simulated Convective Storms. *Mon. Wea. Rev.*, **121**, 2005–2029.

Fan, J. and Coauthors, 2009: Dominant role by vertical wind shear in regulating aerosol effects on deep convective clouds. *J. Geophys. Res.*, **114**, D22206.

Fankhauser, J. C., N. A. Crook, J. Tuttle, L. J. Miller, and C. G. Wade, 1995: Initiation of Deep Convection along Boundary Layer Convergence Lines in a Semitropical Environment. *Mon. Wea. Rev.*, **123**, 291–314.

Feingold, G., H. Jiang, and J. Y. Harrington, 2005: On smoke suppression of clouds in Amazonia. *Geophys. Res. Lett.*, **32**, L02804.

Foote, G. B., 1984: A Study of Hail Growth Utilizing Observed Storm Conditions. *J. Climate Appl. Meteor.*, **23**, 84–101.

Fovell, R. G., 2005: Convective Initiation ahead of the Sea-Breeze Front. *Mon. Wea. Rev.*, **133**, 264–278.

Fovell, R. G., and P. S. Dailey, 2001: Numerical Simulation of the Interaction between the Sea-Breeze Front and Horizontal Convective Rolls. Part II: Alongshore Ambient Flow. *Mon. Wea. Rev.*, **129**, 2057–2072.

Fridlind, A. M. and Coauthors, 2004: Evidence for the predominance of mid-tropospheric aerosols as subtropical anvil cloud nuclei. *Science*, **304**, 718–722.

Garratt, J. R., 1993: Sensitivity of Climate Simulations to Land-Surface and Atmospheric Boundary-Layer Treatments-A Review. *J. Climate*, **6**, 419–448.

Gero, A F., and A J. Pitman, 2006: The Impact of Land Cover Change on a Simulated Storm Event in the Sydney Basin. *J. Appl. Meteor. Climatol.*, **45**, 283–300.

Gilmore, M. S., and L. J. Wicker, 1998: The Influence of Midtropospheric Dryness on Supercell Morphology and Evolution. *Mon. Wea. Rev.*, **126**, 943–958.

Grant, L. D., and S. C. van den Heever, 2014: Microphysical and dynamical characteristics of low-precipitation and classic supercells. *J. Atmos. Sci.* doi:10.1175/JAS-D-13-0261.1, in press.

Gu, L., D. D. Baldocchi, S. C. Wofsy, J. W. Munger, J. J. Michalsky, S. P. Urbanski, and T. A Boden, 2003: Response of a deciduous forest to the Mount Pinatubo eruption: enhanced photosynthesis. *Science*, **299**, 2035–2038.

Gunthe, S. S. and Coauthors, 2009: Cloud condensation nuclei in pristine tropical rainforest air of Amazonia: size-resolved measurements and modeling of atmospheric aerosol composition and CCN activity. *Atmos. Chem. Phys.*, **9**, 7551–7575.

Harrington, J. Y., 1997: The effects of radiative and microphysical processes on simulated warm and transition season Arctic stratus. Ph.D. Dissertation, Colorado State University, 289 pp.

Hill, G. E., 1974: Factors Controlling the Size and Spacing of Cumulus Clouds as Revealed by Numerical Experiments. *J. Atmos. Sci.*, **31**, 646–673.

Hinrichsen, D., 1999: *Coastal water of the world: trends, threats, and strategies*. Island Press, Washington, DC, 298 pp.

Jackson, B., S. E. Nicholson, and D. Klotter, 2009: Mesoscale Convective Systems over Western Equatorial Africa and Their Relationship to Large-Scale Circulation. *Mon. Wea. Rev.*, **137**, 1272–1294.

James, R. P., and P. M. Markowski, 2010: A Numerical Investigation of the Effects of Dry Air Aloft on Deep Convection. *Mon. Wea. Rev.*, **138**, 140–161.

Jiang, H., and G. Feingold, 2006: Effect of aerosol on warm convective clouds: Aerosol-cloud-surface flux feedbacks in a new coupled large eddy model. *J. Geophys. Res.*, **111**, D01202.

Johns, R. H., and C. A. Doswell, 1992: Severe Local Storms Forecasting. *Wea. Forecasting*, **7**, 588–612.

Kala, J., T. J. Lyons, D. J. Abbs, and U. S. Nair, 2010: Numerical Simulations of the Impacts of Land-Cover Change on a Southern Sea Breeze in South-West Western Australia. *Boundary Layer Meteor.*, **135**, 485–503.

Khain, A P., 2009: Notes on state-of-the-art investigations of aerosol effects on precipitation: a critical review. *Environ. Res. Lett.*, **4**, 015004.

Khain, A., D. Rosenfeld, and A. Pokrovsky, 2005: Aerosol impact on the dynamics and microphysics of deep convective clouds. *Quart. J. Roy. Meteor. Soc.*, **131**, 2639–2663.

Khain, A. P., N. BenMoshe, and a. Pokrovsky, 2008: Factors Determining the Impact of Aerosols on Surface Precipitation from Clouds: An Attempt at Classification. *J. Atmos. Sci.*, **65**, 1721–1748.

Khain, A., and B. Lynn, 2009: Simulation of a supercell storm in clean and dirty atmosphere using weather research and forecast model with spectral bin microphysics. *J. Geophys. Res.*, **114**, D19209.

Kikuchi, K., and B. Wang, 2008: Diurnal Precipitation Regimes in the Global Tropics*. *J. Climate*, **21**, 2680–2696.

Kingsmill, D. E., 1995: Convection Initiation Associated with a Sea-Breeze Front, a Gust Front, and Their Collision. *Mon. Wea. Rev.*, **123**, 2913–2933.

Klemp, J. B., and R. B. Wilhelmson, 1978: The Simulation of Three-Dimensional Convective Storm Dynamics. *J. Atmos. Sci.*, **35**, 1070–1096.

Knight, C. A., and K. R. Knupp, 1986: Precipitation Growth Trajectories in a CCOPE Storm. *J. Atmos. Sci.*, **43**, 1057–1073.

Koren, I., Y. J. Kaufman, L. A. Remer, and J. V Martins, 2004: Measurement of the effect of Amazon smoke on inhibition of cloud formation. *Science*, **303**, 1342–1345.

Koren, I., J. V. Martins, L. A. Remer, and H. Afargan, 2008: Smoke invigoration versus inhibition of clouds over the Amazon. *Science*, **321**, 946–949.

Kousky, V. E., 1980: Diurnal Rainfall Variation in Northeast Brazil. *Mon. Wea. Rev.*, **108**, 488–498.

Laing, A. G., R. Carbone, V. Levizzani, and J. Tuttle, 2008: The propagation and diurnal cycles of deep convection in northern tropical Africa. *Quart. J. Roy. Meteor. Soc.*, **134**, 93–109.

Laing, A. G., R. E. Carbone, and V. Levizzani, 2011: Cycles and Propagation of Deep Convection over Equatorial Africa. *Mon. Wea. Rev.*, **139**, 2832–2853.

Lee, S. S., 2011: Dependence of aerosol-precipitation interactions on humidity in a multiple-cloud system. *Atmos. Chem. Phys.*, **11**, 2179–2196.

Lee, S. S., L. J. Donner, V. T. J. Phillips, and Y. Ming, 2008: The dependence of aerosol effects on clouds and precipitation on cloud-system organization, shear and stability. *J. Geophys. Res.*, **113**, D16202.

Lee, S. S., L. J. Donner, and J. E. Penner, 2010: Thunderstorm and stratocumulus: how does their contrasting morphology affect their interactions with aerosols? *Atmos. Chem. Phys.*, **10**, 6819–6837.

Lemon, L. R., and C. A. Doswell, 1979: Severe Thunderstorm Evolution and Mesocyclone Structure as Related to Tornadogenesis. *Mon. Wea. Rev.*, **107**, 1184–1197.

Liebmann, B., I. Bladé, G. N. Kiladis, L. M. V. Carvalho, G. B. Senay, D. Allured, S. Leroux, and C. Funk, 2012: Seasonality of African Precipitation from 1996 to 2009. *J. Climate*, **25**, 4304–4322.

Lilly, D. K., 1962: On the numerical simulation of buoyant convection. *Tellus*, **14**, 148–172.

Lin, J. C., T. Matsui, R. a. Pielke, and C. Kummerow, 2006: Effects of biomass-burning-derived aerosols on precipitation and clouds in the Amazon Basin: a satellite-based empirical study. *J. Geophys. Res.*, **111**, D19204.

Loftus, A. M., 2012: A triple-moment bulk hail microphysics scheme to investigate the sensitivities of hail to aerosols. Ph.D. Dissertation, Colorado State University, 418 pp.

Lu, L., A. S. Denning, M. A. da Silva-Dias, P. da Silva-Dias, M. Longo, S. R. Freitas, and S. Saatchi, 2005: Mesoscale circulations and atmospheric CO 2 variations in the Tapajós Region, Pará, Brazil. *J. Geophys. Res.*, **110**, D21102.

MacGorman, D. R., and D. W. Burgess, 1994: Positive Cloud-to-Ground Lightning in Tornadic Storms and Hailstorms. *Mon. Wea. Rev.*, **122**, 1671–1697.

Mahmood, R. and Coauthors, 2014: Land cover changes and their biogeophysical effects on climate. *Int. J. Climatol.*, **34**, 929–953.

Markowski, P. M., 2008: A comparison of the midlevel kinematic characteristics of a pair of supercell thunderstorms observed by airborne Doppler radar. *Atmos. Res.*, **88**, 314–322.

Marshall, C. H., R. A Pielke, L. T. Steyaert, and D. A Willard, 2004: The Impact of Anthropogenic Land-Cover Change on the Florida Peninsula Sea Breezes and Warm Season Sensible Weather. *Mon. Wea. Rev.*, **132**, 28–52.

Martin, S. T. and Coauthors, 2010: Sources and properties of Amazonian aerosol particles. *Rev. of Geophys.*, **48**, RG2002.

Matsui, T., A. Beltrán-Przekurat, D. Niyogi, R. A. Pielke, and M. Coughenour, 2008: Aerosol light scattering effect on terrestrial plant productivity and energy fluxes over the eastern United States. *J. Geophys. Res.*, **113**, D14S14.

May, P. T., G. Allen, G. Vaughan, and P. Connolly, 2009: Aerosol and thermodynamic effects on tropical cloud systems during TWPICE and ACTIVE. *Atmos. Chem. Phys.*, **9**, 15–24.

May, P. T., V. N. Bringi, and M. Thurai, 2011: Do We Observe Aerosol Impacts on DSDs in Strongly Forced Tropical Thunderstorms? *J. Atmos. Sci.*, **68**, 1902–1910.

McCaul, E. W., and C. Cohen, 2002: The Impact on Simulated Storm Structure and Intensity of Variations in the Mixed Layer and Moist Layer Depths. *Mon. Wea. Rev.*, **130**, 1722–1748.

McCollum, J. R., A. Gruber, and M. B. Ba, 2000: Discrepancy between Gauges and Satellite Estimates of Rainfall in Equatorial Africa. *J. Appl. Meteor.*, **39**, 666–679.

Meyers, M. P., R. L. Walko, J. Y. Harrington, and W. R. Cotton, 1997: New RAMS cloud microphysics parameterization. Part II: The two-moment scheme. *Atmos. Res.*, **45**, 3–39.

Miao, J.-F., L. J. M. Kroon, J. Vila-Guerau de Arellano, and A. A. M. Holtslag, 2003: Impacts of topography and land degradation on the sea breeze over eastern Spain. *Meteor. Atmos. Phys.*, **84**, 157–170.

Mitchell, D. L., 1996: Use of Mass- and Area-Dimensional Power Laws for Determining Precipitation Particle Terminal Velocities. *J. Atmos. Sci.*, **53**, 1710–1723.

Mohr, K. I., and E. J. Zipser, 1996a: Defining Mesoscale Convective Systems by Their 85-GHz Ice-Scattering Signatures. *Bull. Amer. Meteor. Soc.*, **77**, 1179–1189.

Mohr, K. I., and E. J. Zipser, 1996b: Mesoscale Convective Systems Defined by Their 85-GHz Ice Scattering Signature: Size and Intensity Comparison over Tropical Oceans and Continents. *Mon. Wea. Rev.*, **124**, 2417–2437.

Mohr, K. I., J. S. Famiglietti, and E. J. Zipser, 1999: The Contribution to Tropical Rainfall with respect to Convective System Type, Size, and Intensity Estimated from the 85-GHz Ice-Scattering Signature. *J. Appl. Meteor.*, **38**, 596–606.

Moller, A. R., C. A. Doswell, M. P. Foster, and G. R. Woodall, 1994: The Operational Recognition of Supercell Thunderstorm Environments and Storm Structures. *Wea. Forecasting*, **9**, 327–347.

Morrison, H., 2012: On the robustness of aerosol effects on an idealized supercell storm simulated with a cloud system-resolving model. *Atmos. Chem. Phys.*, **12**, 7689–7705.

Nelson, S. P., 1983: The Influence of Storm Flow Structure on Hail Growth. *J. Atmos. Sci.*, **40**, 1965–1983.

Nesbitt, S., and E. Zipser, 2003: The Diurnal Cycle of Rainfall and Convective Intensity according to Three Years of TRMM Measurements. *J. Climate*, **16**, 1456–1475.

Nesbitt, S. W., R. Cifelli, and S. A. Rutledge, 2006: Storm Morphology and Rainfall Characteristics of TRMM Precipitation Features. *Mon. Wea. Rev.*, **134**, 2702–2721.

O'Brien, K. L., 2000: Upscaling tropical deforestation: implications for climate change. *Clim. Change*, **44**, 311–329.

Parker, M. D., 2012: Impacts of Lapse Rates on Low-Level Rotation in Idealized Storms. *J. Atmos. Sci.*, **69**, 538–559.

Petersen, W. A., and S. A. Rutledge, 1998: On the relationship between cloud-to-ground lightning and convective rainfall. *J. Geophys. Res.*, **103**, 14025.

Petersen, W. A., and S. A. Rutledge, 2001: Regional Variability in Tropical Convection: Observations from TRMM. *J. Climate*, **14**, 3566–3586.

Physick, W. L., 1980: Numerical experiments on the inland penetration of the sea breeze. *Quart. J. Roy. Meteor. Soc.*, **106**, 735–746.

Pielke, R. A., J. Adegoke, A. Beltrán-Przekurat, C. A. Hiemstra, J. Lin, U. S. Nair, D. Niyogi, And T. E. Nobis, 2007: An overview of regional land-use and land-cover impacts on rainfall. *Tellus B*, **59**, 587–601.

Prospero, J. M., 2002: Environmental characterization of global sources of atmospheric soil dust identified with the NIMBUS 7 Total Ozone Mapping Spectrometer (TOMS) absorbing aerosol product. *Rev. of Geophys.*, **40**, 1002.

Ramos da Silva, R., and R. Avissar, 2006: The Hydrometeorology of a Deforested Region of the Amazon Basin. *J. Hydrometeor.*, **7**, 1028–1042.

Rasmussen, E. N., and J. M. Straka, 1998: Variations in Supercell Morphology. Part I: Observations of the Role of Upper-Level Storm-Relative Flow. *Mon. Wea. Rev.*, **126**, 2406–2421.

Rasmussen, E. N., J. M. Straka, M. S. Gilmore, and R. Davies-Jones, 2006: A Preliminary Survey of Rear-Flank Descending Reflectivity Cores in Supercell Storms. *Wea. Forecasting*, **21**, 923–938.

Rasmussen, R. M., and A. J. Heymsfield, 1987: Melting and Shedding of Graupel and Hail. Part III: Investigation of the Role of Shed Drops as Hail Embryos in the 1 August CCOPE Severe Storm. *J. Atmos. Sci.*, **44**, 2783–2803.

Riehl, H., and J. S. Malkus, 1958: On the heat balance in the Equatorial trough zone. *Geophysica*, **6**, 503–538.

Roberts, G. C., M. O. Andreae, J. Zhou, and P. Artaxo, 2001: Cloud condensation nuclei in the Amazon Basin: "marine" conditions over a continent? *Geophys. Res. Lett.*, **28**, 2807–2810.

Robinson, F. J., M. D. Patterson, and S. C. Sherwood, 2013: A Numerical Modeling Study of the Propagation of Idealized Sea-Breeze Density Currents*. *J. Atmos. Sci.*, **70**, 653–668.

Rodell, M. and Coauthors, 2004: The Global Land Data Assimilation System. *Bull. Amer. Meteor. Soc.*, **85**, 381–394.

Rosenfeld, D., U. Lohmann, G. B. Raga, C. D. O'Dowd, M. Kulmala, S. Fuzzi, A. Reissell, and M. O. Andreae, 2008: Flood or drought: how do aerosols affect precipitation? *Science*, **321**, 1309–1313.

Saad, S. I., H. R. da Rocha, M. A. F. Silva Dias, and R. Rosolem, 2010: Can the Deforestation Breeze Change the Rainfall in Amazonia? A Case Study for the BR-163 Highway Region. *Earth Interact.*, **14**, 1–25.

Saleeby, S. M., and W. R. Cotton, 2004: A Large-Droplet Mode and Prognostic Number Concentration of Cloud Droplets in the Colorado State University Regional Atmospheric Modeling System (RAMS). Part I: Module Descriptions and Supercell Test Simulations. *J. Appl. Meteor.*, **43**, 182–195.

Saleeby, S. M., and W. R. Cotton, 2008: A Binned Approach to Cloud-Droplet Riming Implemented in a Bulk Microphysics Model. *J. Appl. Meteor. Climatol.*, **47**, 694–703.

Saleeby, S. M., and S. C. van den Heever, 2013: Developments in the CSU-RAMS Aerosol Model: Emissions, Nucleation, Regeneration, Deposition, and Radiation. *J. Appl. Meteor. Climatol.*, **52**, 2601–2622.

Saleeby, S. M., W. Berg, S. van den Heever, and T. L'Ecuyer, 2010: Impact of Cloud-Nucleating Aerosols in Cloud-Resolving Model Simulations of Warm-Rain Precipitation in the East China Sea. *J. Atmos. Sci.*, **67**, 3916–3930.

Seifert, A., and K. D. Beheng, 2006: A two-moment cloud microphysics parameterization for mixed-phase clouds. Part 2: Maritime vs. continental deep convective storms. *Meteor. Atmos. Phys.*, **92**, 67–82.

Seigel, R. B., S. C. van den Heever, and S. M. Saleeby, 2013: Mineral dust indirect effects and cloud radiative feedbacks of a simulated idealized nocturnal squall line. *Atmos. Chem. Phys.*, **13**, 4467–4485.

Smagorinsky, J., 1963: General Circulation Experiments with the Primitive Equations I. The Basic Experiment. *Mon. Wea. Rev.*, **91**, 99–164.

Stein, U., and P. Alpert, 1993: Factor Separation in Numerical Simulations. *J. Atmos. Sci.*, **50**, 2107–2115.

Storer, R. L., and S. C. van den Heever, 2013: Microphysical Processes Evident in Aerosol Forcing of Tropical Deep Convective Clouds. *J. Atmos. Sci.*, **70**, 430–446.

Storer, R. L., S. C. van den Heever, and G. L. Stephens, 2010: Modeling Aerosol Impacts on Convective Storms in Different Environments. *J. Atmos. Sci.*, **67**, 3904–3915.

Tao, W., J. Chen, Z. Li, C. Wang, and C. Zhang, 2012: Impact of aerosols on convective clouds and precipitation. *Rev. of Geophys.*, **50**, RG2001.

Tao, W.-K., X. Li, A. Khain, T. Matsui, S. Lang, and J. Simpson, 2007: Role of atmospheric aerosol concentration on deep convective precipitation: Cloud-resolving model simulations. *J. Geophys. Res.*, **112**, D24S18.

Taylor, C. M., R. A M. de Jeu, F. Guichard, P. P. Harris, and W. A Dorigo, 2012: Afternoon rain more likely over drier soils. *Nature*, **489**, 423–426.

Twomey, S., 1977: The Influence of Pollution on the Shortwave Albedo of Clouds. *J. Atmos. Sci.*, **34**, 1149–1152.

van den Heever, S. C., and W. R. Cotton, 2004: The Impact of Hail Size on Simulated Supercell Storms. *J. Atmos. Sci.*, **61**, 1596–1609.

van den Heever, S. C., and W. R. Cotton, 2007: Urban Aerosol Impacts on Downwind Convective Storms. *J. Appl. Meteor. Climatol.*, **46**, 828–850.

van den Heever, S. C., G. G. Carrió, W. R. Cotton, P. J. DeMott, and A. J. Prenni, 2006: Impacts of Nucleating Aerosol on Florida Storms. Part I: Mesoscale Simulations. *J. Atmos. Sci.*, **63**, 1752–1775.

van den Heever, S. C., G. L. Stephens, and N. B. Wood, 2011: Aerosol Indirect Effects on Tropical Convection Characteristics under Conditions of Radiative–Convective Equilibrium. *J. Atmos. Sci.*, **68**, 699–718.

Vondou, D. A., A. Nzeukou, and F. M. Kamga, 2010: Diurnal cycle of convective activity over the West of Central Africa based on Meteosat images. *Int. J. Appl. Earth Obs. Geoinf.*, **12**, S58–S62.

Wakimoto, R. M., and N. T. Atkins, 1994: Observations of the Sea-Breeze Front during CaPE. Part I: Single-Doppler, Satellite, and Cloud Photogrammetry Analysis. *Mon. Wea. Rev.*, **122**, 1092–1114.

Walko, R. L., W. R. Cotton, M. P. Meyers, and J. Y. Harrington, 1995: New RAMS cloud microphysics parameterization Part I: the single-moment scheme. *Atmos. Res.*, **38**, 29–62.

Walko, R. L. and Coauthors, 2000: Coupled Atmosphere–Biophysics–Hydrology Models for Environmental Modeling. *J. Appl. Meteor.*, **39**, 931–944.

Wall, C., E. Zipser, and C. Liu, 2014: An Investigation of the Aerosol Indirect Effect on Convective Intensity Using Satellite Observations. *J. Atmos. Sci.*, **71**, 430–447.

Weisman, M. L., and J. B. Klemp, 1982: The Dependence of Numerically Simulated Convective Storms on Vertical Wind Shear and Buoyancy. *Mon. Wea. Rev.*, **110**, 504–520.

Weisman, M. L., and J. B. Klemp, 1984: The Structure and Classification of Numerically Simulated Convective Storms in Directionally Varying Wind Shears. *Mon. Wea. Rev.*, **112**, 2479–2498.

Weisman, M. L., and H. B. Bluestein, 1985: Dynamics of numerically simulated LP storms. Preprints,*15th Conf. on Severe Local Storms*, Indianapolis, IN, Amer. Meteor. Soc., 167–171.

Wilson, J. W., and D. L. Megenhardt, 1997: Thunderstorm Initiation, Organization, and Lifetime Associated with Florida Boundary Layer Convergence Lines. *Mon. Wea. Rev.*, **125**, 1507–1525.

Xue, H., and G. Feingold, 2006: Large-Eddy Simulations of Trade Wind Cumuli: Investigation of Aerosol Indirect Effects. *J. Atmos. Sci.*, **63**, 1605–1622.

Yang, G.-Y., and J. Slingo, 2001: The Diurnal Cycle in the Tropics. *Mon. Wea. Rev.*, **129**, 784–801.

Yu, H., 2002: Radiative effects of aerosols on the evolution of the atmospheric boundary layer. *J. Geophys. Res.*, **107**, 4142.

Zhang, Y., R. Fu, H. Yu, R. E. Dickinson, R. N. Juarez, M. Chin, and H. Wang, 2008: A regional climate model study of how biomass burning aerosol impacts land-atmosphere interactions over the Amazon. *J. Geophys. Res.*, **113**, D14S15.

Ziegler, C. L., and E. N. Rasmussen, 1998: The Initiation of Moist Convection at the Dryline: Forecasting Issues from a Case Study Perspective. *Wea. Forecasting*, **13**, 1106–1131.

Zipser, E. J., C. Liu, D. J. Cecil, S. W. Nesbitt, and D. P. Yorty, 2006: Where are the most intense thunderstorms on earth? *Bull. Amer. Meteor. Soc.*, **87**, 1057–1071.